



**UNIVERSIDAD DE INVESTIGACIÓN DE
TECNOLOGÍA EXPERIMENTAL YACHAY**

Escuela de Ciencias Físicas y Nanotecnología

**TÍTULO: Theoretical Optical Absorption and Electron Energy
Loss Spectroscopy Using LCAO-TDDFT- k - ω of Chlorophyll and
Carbon Nanotubes**

Trabajo de integración curricular presentado como requisito para la
obtención del título de Física

Autora:

Preciado Rivas María Rosa

Tutor:

Ph. D. Mowbray Duncan John

Urcuquí, agosto 2019

Urcuquí, 28 de agosto de 2019

SECRETARÍA GENERAL
(Vicerrectorado Académico/Cancillería)
ESCUELA DE CIENCIAS FÍSICAS Y NANOTECNOLOGÍA
CARRERA DE FÍSICA
ACTA DE DEFENSA No. UITEY-PHY-2019-00021-AD

En la ciudad de San Miguel de Urcuquí, Provincia de Imbabura, a los 28 días del mes de agosto de 2019, a las 15:30 horas, en el Aula Sala Capitular de la Universidad de Investigación de Tecnología Experimental Yachay y ante el Tribunal Calificador, integrado por los docentes:

Presidente Tribunal de Defensa	Dr. PINTO ESPARZA, HENRY PAUL , Ph.D.
Miembro No Tutor	Dr. REINOSO CARLOS , Ph.D.
Tutor	Dr. MOWBRAY , DUNCAN JOHN , Ph.D.

Se presenta el(la) señor(ita) estudiante PRECIADO RIVAS, MARIA ROSA, con cédula de identidad No. 0706023892, de la ESCUELA DE CIENCIAS FÍSICAS Y NANOTECNOLOGÍA, de la Carrera de FÍSICA, aprobada por el Consejo de Educación Superior (CES), mediante Resolución RPC-SO-39-No.456-2014, con el objeto de rendir la sustentación de su trabajo de titulación denominado: Theoretical Optical Absorption and Electron Energy Loss Spectroscopy Using LCAO-TDDFT-k-? of Chlorophyll and Carbon Nanotubes., previa a la obtención del título de FÍSICO/A.

El citado trabajo de titulación, fue debidamente aprobado por el(los) docente(s):

Tutor	Dr. MOWBRAY , DUNCAN JOHN , Ph.D.
--------------	-----------------------------------

Y recibió las observaciones de los otros miembros del Tribunal Calificador, las mismas que han sido incorporadas por el(la) estudiante.

Previamente cumplidos los requisitos legales y reglamentarios, el trabajo de titulación fue sustentado por el(la) estudiante y examinado por los miembros del Tribunal Calificador. Escuchada la sustentación del trabajo de titulación, que integró la exposición de el(la) estudiante sobre el contenido de la misma y las preguntas formuladas por los miembros del Tribunal, se califica la sustentación del trabajo de titulación con las siguientes calificaciones:

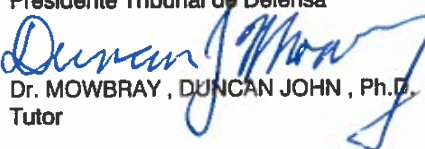
Tipo	Docente	Calificación
Presidente Tribunal De Defensa	Dr. PINTO ESPARZA, HENRY PAUL , Ph.D.	9,8
Tutor	Dr. MOWBRAY , DUNCAN JOHN , Ph.D.	10,0
Miembro Tribunal De Defensa	Dr. REINOSO CARLOS , Ph.D.	10,0

Lo que da un promedio de: 9.9 (Nueve punto Nueve), sobre 10 (diez), equivalente a: APROBADO

Para constancia de lo actuado, firman los miembros del Tribunal Calificador, el/la estudiante y el/la secretario ad-hoc.


PRECIADO RIVAS, MARIA ROSA
Estudiante


Dr. PINTO ESPARZA, HENRY PAUL , Ph.D.
Presidente Tribunal de Defensa


Dr. MOWBRAY , DUNCAN JOHN , Ph.D.
Tutor


Dr. REINOSO CARLOS, Ph.D.
Miembro No Tutor


CIFUENTES TAPUR, EVELYN CAROLINA
Secretario Ad-hoc

Autoría

Yo, **María Rosa Preciado Rivas**, con cédula de identidad 0706023892, declaro que las ideas, juicios, valoraciones, interpretaciones, consultas bibliográficas, definiciones y conceptualizaciones expuestas en el presente trabajo, así como los procedimientos y herramientas utilizadas en la investigación, son de absoluta responsabilidad de la autora del trabajo de integración curricular. Así mismo, me acojo a los reglamentos internos de la Universidad de Investigación de Tecnología Experimental Yachay.

Urcuquí, agosto 2019.

María Rosa Preciado Rivas

C. I. 0706023892

Autorización de publicación

Yo, **María Rosa Preciado Rivas**, con cédula de identidad 0706023892, cedo a la Universidad de Tecnología Experimental Yachay, los derechos de publicación de la presente obra, sin que deba haber un reconocimiento económico por este concepto. Declaro además que el texto del presente trabajo de titulación no podrá ser cedido a ninguna empresa editorial para su publicación u otros fines, sin contar previamente con la autorización escrita de la Universidad.

Asimismo, autorizo a la Universidad para que realice la digitalización y publicación de este trabajo de integración curricular en el repositorio virtual, de conformidad a lo dispuesto en el Art. 144 de la Ley Orgánica de Educación Superior.

Urcuquí, agosto 2019.

María Rosa Preciado Rivas

C. I. 0706023892

Acknowledgements

I acknowledge my advisor Duncan J. Mowbray for his guidance, support and help with this thesis and other scientific articles. I thank him for letting me be part of his research group and always being willing to answer any questions about my work either in his office or in “Árbol de la Vida”.

I thank my classmates Alexander Torres, Emilia Calderón and Sebastián Cortez who performed some of the calculations presented in this thesis. I also thank Keenan Lyon and Vito Despoja for their contribution to the LCAO-TDDFT- k - ω code.

Agradezco a mis padres, Toti y Winston, por todo el apoyo que me han dado desde siempre, por confiar en mí y nunca dejar que me rindiera. Todo su esfuerzo y trabajo están reflejados en mis logros académicos, incluida esta tesis. También agradezco a mis hermanos, Teo y Winston, por estar constantemente ayudando a mis papás. Así mismo agradezco a toda mi familia por su cariño y estar pendiente de mí.

A very special gratitude goes to my roommates and university friends for their moral and emotional support.

I am also grateful to all the professors, dean, and staff of the School of Physical Sciences and Nanotechnology for their support and assistance.

Finally, this work employed the Imbabura cluster of Yachay Tech University, which was purchased under contract No. 2017-024 (SIE-UI TEY-007-2017).

Resumen

El desarrollo de sistemas fotovoltaicos orgánicos (OPVs) más eficientes, ecológicos y económicos es un desafío fundamental de la nanotecnología. Una forma prometedora de abordar este problema es el diseño computacional de OPVs de última generación. Entender los procesos de excitación llevados a cabo en las grandes moléculas de tales sistemas requiere del desarrollo de nuevos métodos computacionales, precisos y altamente eficientes, para describir sus espectros de absorción óptica. En este trabajo, usamos una representación eficiente de las funciones de onda de Kohn-Sham (KS) por medio de una combinación lineal de orbitales atómicos (LCAO), para realizar cálculos de la teoría del funcional de la densidad tiempo-dependiente (TDDFT) en el dominio de la frecuencia usando el código LCAO-TDDFT- $k-\omega$. Al aplicar la corrección de la discontinuidad de la derivada del funcional de Gritsenko-Leeuwen-Lenthe-Baerends para sólidos y correlación (GLLB-SC) a las energías propias de KS, obtenemos una descripción semicuantitativa de la estructura electrónica. De esta manera, podemos confiar en estos métodos para obtener una descripción precisa de los espectros de absorción óptica con una reducción significativa del esfuerzo computacional. Aplicamos este método para calcular los espectros de absorción óptica de moléculas tales como monómeros y dímeros de clorofila, nanotubos de carbono de pared simple y combinaciones de los mismos que son potenciales OPVs.

Palabras clave: Teoría del funcional de la densidad, LCAO-TDDFT- $k-\omega$ code, espectros de absorción óptica, clorofila, nanotubos de carbono de pared simple, sistemas fotovoltaicos orgánicos

Abstract

The development of more efficient, environmentally friendly, and inexpensive organic photovoltaics (OPVs) is a fundamental challenge in nanotechnology. One promising way to address this problem is the computational design of next generation OPVs. Understanding the excitation processes undergone by the large molecules in such systems requires the development of novel accurate and highly efficient computational methods for describing their optical absorption spectra. In this work, we use an efficient linear combination of atomic orbitals (LCAO) representation of the Kohn-Sham (KS) wavefunctions to perform time-dependent density functional theory (TDDFT) calculations in the frequency domain using the LCAO-TDDFT- k - ω code. By applying the derivative discontinuity correction of the Gritsenko-Leeuwen-Lenthe-Baerends solid and correlation (GLLB-SC) functional to the KS eigenenergies, we obtain a semi-quantitative description of the electronic structure. In this way we can rely on these methods to obtain an accurate description of the optical absorption spectra with a significant reduction in computational effort. We apply this method to calculate the optical absorption spectra of molecules such as chlorophyll monomers and dimers, single-walled carbon nanotubes and combinations thereof which are potential OPVs.

Keywords: Density functional theory, LCAO-TDDFT- k - ω code, optical absorption spectra, chlorophyll, single-walled carbon nanotubes, OPV

Contents

List of Figures	xvii
List of Tables	xx
List of Papers	xxi
1 Introduction	1
1.1 Problem Statement	5
1.2 General and Specific Objectives	6
1.3 Overview	6
2 Theoretical Background	9
2.1 Density Functional Theory	9
2.1.1 The Many Body Problem	9
2.1.2 Born-Oppenheimer Approximation	10
2.1.3 Periodic Systems	12
2.1.4 The Hohenberg-Kohn theorem	14
2.1.5 Kohn-Sham Self-consistent Field Procedure	16
2.1.6 Exchange and correlation Functionals	19
2.1.7 Derivative Discontinuity	21
2.1.8 Band Gap	23
2.1.9 GLLB-SC to Describe Band Gaps	24

2.2	Representations of the KS wavefunctions	25
2.2.1	Real space	25
2.2.2	Plane Waves	26
2.2.3	Linear Combination of Atomic Orbitals	26
2.2.4	Naming convention of LCAO basis sets	27
2.3	Projector Augmented Wave Method	27
2.4	Time-Dependent Density Functional Theory	29
2.4.1	Runge-Gross Theorem	30
2.4.2	Linear Density Response	31
2.4.3	Dielectric matrix using LDR-TDDFT-RPA	35
2.5	Chlorophyll	37
2.6	Single-Walled Carbon Nanotubes	39
3	Methodology	43
3.1	Chlorophyll Monomers Structures & Computational details	43
3.2	Single-Walled Carbon Nanotubes Structures & Computational Details	46
3.3	Combined System Structure & Computational Details	48
4	Results & Discussion	51
4.1	Chlorophyll <i>a</i> and <i>b</i> Monomers	51
4.1.1	Optical Absorption Spectra	51
4.1.2	Excitonic Density	57
4.2	Single-Walled Carbon Nanotubes	59
4.2.1	Optical Absorption Spectra	59
4.2.2	E_{11} and E_{22} Transitions	63
4.2.3	Electron Energy Loss Spectroscopy	64
4.2.4	Excitonic Density	68
4.3	Chl <i>a</i> /(6,4) SWNT	69
4.3.1	Optical Absorption	69
4.3.2	Excitonic Density	70

5	Conclusions & Outlook	73
A	Excitations of <i>full</i>-1⁺ and <i>cut</i>-1⁺ Structures	77
	Bibliography	79
	Abbreviations	93

List of Figures

2.1	Kohn-Sham self-consistent scheme	18
2.2	Derivative Discontinuity	22
2.3	Chlorophyll <i>a</i> and <i>b</i> Structures	38
2.4	Graphene sheet	40
2.5	DOS of Metallic and Semiconducting SWCNTs	41
3.1	Chlorophyll <i>a</i> and <i>b</i> Structures with Charged Tags	45
3.2	single-walled carbon nanotube (SWCNT) map	47
3.3	Schematics of the system chlorophyll (Chl) <i>a</i> /(6,4) CNT	49
4.1	Basis Set Dependence of the Optical Absorption Spectra for Chl <i>a</i>	52
4.2	LCAO and plane wave (PW) Optical Absorption Spectra for Chl <i>a</i> and <i>b</i>	54
4.3	Chlorophyll <i>a</i> and <i>b</i> Optical Absorbance Spectra	56
4.4	Excitations of cut- $\mathbf{1}^+$	58
4.5	SWCNT Optical Absorbance Spectra	62
4.6	Comparison of Theoretical and Experimental E_{11} Energies	63
4.7	Comparison of Theoretical and Experimental E_{22} Energies	65
4.8	SWNT Electron Energy Loss Spectra	67
4.9	Exciton density difference of the (6,4) SWCNT	68
4.10	Optical Absorption Spectra of the Chl <i>a</i> /(6,4) SWCNT	70
4.11	Exciton density difference of Chl <i>a</i> /(6,4) CNT	71
A.1	Excitations of full- $\mathbf{1}^+$	77

A.2 Excitations of cut 78

List of Tables

4.1	Relaxed single-walled carbon nanotube (SWCNT) diameters d in Å, unit cell lengths L in Å, numbers of atoms N_{at} per unit cell, and derivative discontinuity corrections Δ_x and electronic band gaps E_{gap} in eV.	60
-----	--	----

List of Papers

- [1] Preciado-Rivas, M. R.; Mowbray, D. J.; Larsen, A. H.; Lyon, K.; Milne, B. F. “Optical Excitations of Chlorophyll *a* and Chlorophyll *b* Monomers and Dimers”, *Submitted to Journal of Chemical Physics* (2019), arXiv:1907.09430.

- [2] Preciado-Rivas, M. R.; Torres-Sanchez, V. A.; Mowbray, D. J. “Optical Absorption and Energy Loss Spectroscopy of Single-Walled Carbon Nanotubes”, *Submitted to Physical Review B* (2019), arXiv:1907.08036.

Chapter 1

Introduction

In Ecuador, 35% of electrical power comes from non-renewable sources such as fossil fuels which are used in internal combustion engines. While the remaining 65% is obtained from renewable sources, only 0.32% is generated by photovoltaics¹. In other words, solar energy is being harnessed very poorly in a country where each day has a constant of 12 hours of sunlight throughout the year due to its geographic location on or near the equator. One major obstacle for using photovoltaics to obtain clean energy is the high production cost of common silicon-based cells. This is because of the expensive vacuum and high temperature processes involved in their production²⁻⁴. Although the efficiencies of their inorganic counterparts are currently higher⁵, novel organic photovoltaic (OPV) cells are still of interest since their production costs are lower⁶. More importantly, silicon-based cells have a maximum efficiency of 33.7% according to the Shockley–Queisser limit^{7,8}, which does not apply to OPVs. This opens the possibility, at least theoretically, of producing OPVs with significantly higher efficiencies than silicon-based cells. Such cells could contain materials from dyes⁹ and polymers¹⁰ to carbon-only structures such as graphene^{11,12}, fullerenes¹³, and carbon nanotubes^{14,15}.

A solar photovoltaic cell is a device that harnesses the energy of electromagnetic radiation from the sun and ultimately converts it into electrical energy. Typically, photons or quanta of light are absorbed by a semiconducting material in the solar cell. If the energy of a photon is equal to or higher than the energy band gap, the photon can be absorbed in an interband process where an

electron is excited from the valence band to the conduction band of the semiconductor. Before it returns to its previous state by dissipating energy, via a small bias, the electron can be conducted to an electrode within the solar cell. In this way an electric current can be produced^{16,17}. Within this scheme, common solar cells use the p-n junctions of doped silicon¹⁸, cadmium telluride¹⁹, copper indium gallium selenide²⁰, gallium arsenide²¹ and others as the semiconducting material that absorbs light, whereas organic solar cells use polymers^{10,13} and other organic molecules⁹ as their light-absorbing semiconducting material.

The organic materials used in OPVs have the common characteristic of being large π -conjugated systems. In such systems, carbon atoms are connected by alternating single and double bonds where a delocalized bonding π orbital and an antibonding π^* orbital are formed. This configuration in general decreases the overall energy and stabilizes the molecule or ion. The delocalized π orbital becomes the highest occupied molecular orbital (HOMO) and takes the role of the valence band; whereas the π^* orbital becomes the lowest unoccupied molecular orbital (LUMO) and replaces the conduction band. The energy separation between these two states is considered the energy band gap of the organic material^{22,23}. This is why materials such as graphene, graphite, carbon nanotubes and polymers are the largest conjugated systems suitable for photovoltaic applications.

In particular, single-walled carbon nanotubes (SWCNTs) have drawn attention in the field of organic electronics due to their unique physical properties²⁴. These quasi-one-dimensional structures come in various chiralities, which depend on the way they are rolled up, changing their energy band gaps and yielding different absorption and/or conductive properties²⁵. A variety of different semiconducting SWCNTs can be used to widen the range of light wavelengths that can be potentially exploited in photovoltaic applications^{26,27}. They exhibit intense absorption peaks with band gaps around 1 to 1.3 eV and have high thermal stability^{28,29}. In the case of metallic nanotubes, electronic transport occurs ballistically, meaning they can carry high currents without heating^{30,31}. Furthermore, a clear advantage is the recently developed methods for separating SWCNTs based on their chirality³². This provides a straightforward method for tailoring the band gap of the semiconducting layer in a solar cell.

For these reasons, SWCNTs have been widely used as additives in OPVs to improve their effi-

ciency by increasing the charge carrier mobility of conventional polymers^{33,34} and dye-sensitized solar cells. In donor-acceptor hybrid cells, SWCNTs have been used to either covalently³⁵ or non-covalently³⁶ graft chromophore molecules, increasing the incident photon-to-current efficiency (IPCE) or external quantum efficiency of the solar cell by about 17%. SWCNTs can interact with polymers via π - π stacking, porphyrins electrostatically³⁷ to achieve an IPCE of 8.4%, lipid nanodiscs, and human deoxyribonucleic acid (DNA)³⁸. Moreover, in many other photovoltaic devices, metallic carbon nanotubes are used as electrodes because of their ballistic conducting properties.

Other organic molecules used for light absorption include well known pigments such as chlorophyll (Chl) *a* and *b*, carotenoids, and phycoerythrin. These molecules are involved in the photosynthesis processes which take place in large light-harvesting complexes (LHCs) of green plants and algae, where the production of carbohydrates from CO₂ and water is driven by light absorption. Moreover, the *in vivo* absorption spectra of these photosynthetic pigments have their maximum at the maximum of the solar spectrum photon flux density at the Earth's surface³⁹, which corresponds to the visible region. In 1993, derivatives of chlorophyll were used to photosensitize colloidal TiO₂ electrodes in solar cells that achieved light harvesting and charge separation comparable to those in natural photosynthesis, that is, artificial photosynthesis⁴⁰. More recently, further experimental work has been done in order to improve the performance of these types of dye-sensitized solar cells, achieving a solar energy-to-electricity conversion efficiency of ~1.3%^{41,42}. Specifically, chlorophyll is a magnesium-containing chlorin, that is, a partially hydrogenated version of a porphyrin⁴³. Also, functionalized SWCNTs interacting electrostatically with porphyrin molecules have been used to increase the IPCE of donor acceptor solar cells³⁷.

The recombination of an electron from the conduction band with a hole from the valence band is an unwanted process in a solar cell. For this reason, efforts must be made to minimize electron-hole recombination, or germination. A feature that must be taken into account when designing OPVs is the degree of the charge separation, which can involve different and/or separate molecules or materials. For example, a hole can be created in a dye or polymer while the electron is transferred to a conductive layer, such as a SWCNT. Once this step is accomplished, the hole

on the dye or polymer should be filled again to repeat the cycle. This final necessary process can be undertaken by ions in a solution, such as iodine ions for example.

Spectroscopy techniques are often used to characterize carbon nanotubes and molecules such as chlorophyll. The advantages of optical absorption, a specific type of spectroscopy, rely on the fact that it is nondestructive, noninvasive as well as simple to perform at room temperature and under ambient pressure. For instance, photoluminescence, absorption, and resonance Raman spectroscopy are widely employed in bulk SWCNT samples in both research^{44,45} and industrial laboratories⁴⁶. This makes spectroscopy techniques important for the development of OPVs, since these methods provide insight into the properties of the materials, whether they are suitable for photovoltaic devices, and how they can be improved. Also, it can be said that information about the exciton generation process is gathered by spectroscopic techniques to make further improvements in the design of OPVs. This is because, in the case of optical absorption, light is most often absorbed when in resonance with the band gap of the material so that the observation of absorption peaks are related to electronic transitions.

On the one hand, pump-probe spectroscopy has been used to study the excited state dynamics of the first optical transition, E_{11} , in SWCNTs⁴⁷. And electron energy loss spectroscopy (EELS) has been used to experimentally study how optical properties and electronic transport are correlated with structure in carbon nanotubes⁴⁸. On the other hand, experimental studies have given insight into the absorption spectrum and properties of both Chl monomers and dimers with and without the proteins that contain them in biological structures⁴⁹⁻⁵¹. Moreover, experimental onset energies and absorption spectra of Chl *a* and *b* have been reported to be blue-shifted by 30 to 70 nm compared to that of chlorophyll-containing proteins⁵².

Theoretical calculations of the photoabsorption processes provide insight into not only how excitons are generated, but also other properties, such as the charge distribution, which can help to explain what is observed in experimental data. Some of the most commonly used methods are those based on density functional theory (DFT)⁵³. DFT, based on the hypothesis that the electron density distribution completely characterizes the ground state of many electron systems, uses functionals of the spatially dependent electron density to model the ground state electronic structure and properties at the quantum mechanical level. DFT has made important contributions

before in designing materials using theory and computation to replace traditional, and often time consuming and expensive, experiments^{54,55}. For instance, DFT calculations have been done to unravel the characteristics of spectroscopy for both SWCNTs and chlorophyll: linear response time-dependent density functional theory (TDDFT) was used to complement the experimental work made in Ref. 47; additionally, estimates of the internal quantum efficiency of organic photovoltaic devices containing polymers, fullerene C₆₀ and SWCNTs have been obtained using DFT⁵⁶. Also, first-principles calculations using real-space TDDFT were performed in Ref. 57 for the LHC of chlorophyll.

1.1 Problem Statement

There is not an unique way to perform theoretical calculations on molecular systems and obtain an accurate description of their properties observed. Therefore, the problem, that is meant to be tackled in this thesis, is the lack of a defined efficient yet accurate method to do theoretical spectroscopy calculations on big organic molecules and carbon-based nanostructures, in order to study their excitation processes. We believe that is important to solve this problem, not just to reproduce what is observed on the available experimental data, but to also predict the properties of these kind of materials and, to some extent, evaluate their suitability as components of OPVs.

This was our motivation to perform TDDFT calculations using linear combinations of atomic orbitals (LCAOs) to represent the Kohn-Sham (KS) wavefunctions in order to obtain the optical absorption and electron energy loss spectra as well as the excitonic density distribution of chlorophyll and SWCNTs and to apply the derivative discontinuity correction of the Gritsenko-Leeuwen-Lenthe-Baerends solid and correlation (GLLB-SC) functional. We implemented this by using `gpaW`⁵⁸, a Python code based on the projector-augmented wave (PAW) method and the atomic simulation environment (ASE)⁵⁹, and the LCAO-TDDFT- k - ω code⁴⁷.

1.2 General and Specific Objectives

The general goal of this thesis is to contribute to the design of next generation OPVs because it has been estimated that OPVs could have a higher efficiencies than their inorganic counterparts. However, only a 10% efficiency has been obtained so far experimentally. Our aim is to contribute by studying the properties that can be obtained by performing theoretical spectroscopy calculations in both SWCNTs and chlorophyll, and to provide, to some extent, tools for the computational screening of materials for OPVs. Somewhat surprisingly, such methods are still an open problem in computational physics, as there is currently a lack of both accurate and efficient methods for performing such calculations.

1.3 Overview

This thesis has five chapters and an appendix. The first chapter corresponds to this Introduction where we have introduced OPVs, why we want to study the optical absorption properties of chlorophyll, single-walled carbon nanotubes and combined systems containing both, and how this still is an open problem.

In the second chapter, Theoretical Background, the concepts behind density functional theory, Kohn-Sham wavefunctions, exchange and correlation functionals and their approximations are reviewed. We also described the GLLB-SC derivative discontinuity correction, the projector augmented wave method and the linear combination of atomic orbital basis set, in order to understand the theory used in `gpaw` and the `LCAO-TDDFT-k- ω` code. Also, we include a description of the chlorophyll monomers and SWCNTs.

In the third chapter, Methodology, we introduce the actual structures of the molecules used in the calculations and the computational details so the results can be replicated.

The fourth chapter, Results & Discussion, is separated into three well-defined sections. The first one covers the optical absorption spectra and its dependance on the basis set for Chl *a* and Chl *b* monomers as well as the excitonic density of the first four transitions. The second section is dedicated to optical absorption and electron energy loss spectroscopy of SWCNTs, their E_{11}

and E_{22} transitions' energies and the excitonic density of the (6,4) SWCNT. In the last section we show the optical absorbance for a combined system, Chl *a*/(6,4) SWCNT. and its excitonic density.

Finally in the fifth chapter, Conclusions, we summarize the principal results and provide an outlook for future research.

Chapter 2

Theoretical Background

2.1 Density Functional Theory

2.1.1 The Many Body Problem

The wavefunction Ψ of a quantum system's state is described by Schrödinger's equation. In the case of a well defined set of atoms, e.g., a molecule or crystal, the wavefunction will be defined by the positions and spins of its nuclei and electrons as

$$\Psi(\mathbf{r}_1, s_1, \dots, \mathbf{r}_N, s_N; \mathbf{R}_1, S_1, \dots, \mathbf{R}_M, S_M), \quad (2.1)$$

where \mathbf{r}_i and s_i are the coordinates and spins for the N electrons; and \mathbf{R}_I and S_I are the coordinates and spins for the M nuclei.

The many-body Hamiltonian \hat{H} is the operator corresponding to the sum of the kinetic energies and the interactions

$$\hat{H} = -\frac{1}{2} \sum_i \nabla_{\mathbf{r}_i}^2 - \sum_i \sum_I \frac{Z_I}{|\mathbf{r}_i - \mathbf{R}_I|} + \frac{1}{2} \sum_{i \neq j} \frac{1}{|\mathbf{r}_i - \mathbf{r}_j|} - \frac{1}{2} \sum_I \frac{1}{M_I} \nabla_{\mathbf{R}_I}^2 + \frac{1}{2} \sum_{I \neq J} \frac{1}{|\mathbf{R}_I - \mathbf{R}_J|}, \quad (2.2)$$

where $\nabla_{\mathbf{r}_i}^2$ and $\nabla_{\mathbf{R}_I}^2$ are the Laplacians with respect to the electronic and nuclear coordinates; and Z_I and M_I are the atomic number and mass of the I th nucleus, respectively, in atomic units ($m_e = a_0 = \hbar = e = 1$). In Eq. 2.2 the first term is the kinetic energy operator for electrons, \hat{T}_e , the

second term describes the attractive Coulomb interaction potential between positively charged nuclei and negatively charged electrons, V_{e-n} , the third term is the repulsive interaction potential between electrons, V_{e-e} , the fourth term is the kinetic energy operator for nuclei, \hat{T}_n , and the last term is the repulsive interaction potential between nuclei, V_{n-n} . So the many-body Hamiltonian can be written as

$$\hat{H} = \hat{T}_e - V_{e-n} + V_{e-e} + \hat{T}_n + V_{n-n}. \quad (2.3)$$

The linear transformation of the wavefunction Ψ given by the Hamiltonian \hat{H} is related to the evolution of Ψ over time t . Such a relation is

$$i \frac{\partial}{\partial t} \Psi(\mathbf{x}, t) = \hat{H} \Psi(\mathbf{x}, t), \quad (2.4)$$

where $\mathbf{x} \equiv \{\mathbf{r}_1, s_1, \dots, \mathbf{r}_N, s_N; \mathbf{R}_1, S_1, \dots, \mathbf{R}_M, S_M\}$ represents all the position coordinates and spins of all nuclei and electrons. This is the time-dependent Schrödinger equation, which is a linear partial differential equation that describes the wavefunction of the many-body system, in the position basis⁶⁰. All the physical observables of the system can be deduced from the eigenfunctions and eigenvalues that solve this equation.

Because the potential only depends on the position but not on time, the wavefunction is separable into a time-dependent and a time-independent part with separation constant E . The time-independent Schrödinger equation for the many-problem is then

$$\hat{H}\psi(\mathbf{x}) = E\psi(\mathbf{x}). \quad (2.5)$$

Eq. 2.5 has an infinite collection of solutions ψ_i with eigenvalue E_i . Then the general solution is a linear combination of the separable solutions:

$$\Psi(\mathbf{x}, t) = \sum_{i=0}^{\infty} c_i \psi_i(\mathbf{x}) e^{-iE_i t/\hbar} \quad (2.6)$$

2.1.2 Born-Oppenheimer Approximation

The proton-to-electron mass ratio, independent of the system of units, is $m_p/m_e \approx 1836.15267389$, so that a proton is three orders of magnitude heavier than an electron. This means nuclei, which

are composed of tens of protons and neutrons, will have much slower velocities than electrons at the same temperature. In other words, on the time-scale of the nuclear motion, the electrons will very rapidly relax to the instantaneous ground-state configuration⁶¹. Thus it is safe to assume that the nuclei are stationary while the electrons relax. Consequently, the many-body wavefunction can be separated into a nuclear and an electronic part. Such separability is known as the Born-Oppenheimer approximation⁶².

$$\psi(\mathbf{x}) = \psi_e(\mathbf{r}_1, s_1, \dots, \mathbf{r}_N, s_N) \otimes \psi_n(\mathbf{R}_1, S_1, \dots, \mathbf{R}_M, S_M), \quad (2.7)$$

where ψ_e is the electronic wavefunction and ψ_n is the nuclear wavefunction. We can then solve for the electronic part first, calculate the energy of the system in that configuration, and then solve for the nuclear motion. The many-body Hamiltonian problem can thus be simplified to a problem in terms of the electronic Hamiltonian \hat{H}_e :

$$\hat{H}_e = -\frac{1}{2} \sum_{i=1} \nabla_{\mathbf{r}_i}^2 + \frac{1}{2} \sum_{i \neq j} \frac{1}{|\mathbf{r}_i - \mathbf{r}_j|} + V_{ext}^{\mathbf{R}_1, \dots, \mathbf{R}_M}(\mathbf{r}_1, \dots, \mathbf{r}_N), \quad (2.8)$$

where the external potential V_{ext} includes electronic interactions with any external fields. The nuclei still interact electromagnetically with the electrons and this interaction is included in the external potential V_{ext} . Thus it is said that the electronic wavefunction depends only parametrically on the nuclear position coordinates $\mathbf{R}_1, \dots, \mathbf{R}_M$. We thus obtain the “frozen-nuclei” Schrödinger equation

$$\hat{H}_e \psi_e(\mathbf{r}_1, s_1, \dots, \mathbf{r}_N, s_N) = \varepsilon(\mathbf{R}_1, S_1, \dots, \mathbf{R}_M, S_M) \psi_e(\mathbf{r}_1, s_1, \dots, \mathbf{r}_N, s_N). \quad (2.9)$$

Eq. 2.9 has also a collection of solutions ψ_{e_i} with eigenvalues ε_i . These are the potential energy surfaces which are representations of the electronic energy of the system. Neglecting the kinetic energy of the nuclei, we find that:

$$\begin{aligned} \hat{H} \psi(\mathbf{x}) &= \hat{H}_e \psi_n(\mathbf{R}_1, S_1, \dots, \mathbf{R}_M, S_M) \psi_e(\mathbf{r}_1, s_1, \dots, \mathbf{r}_N, s_N) \\ &= \psi_n(\mathbf{R}_1, S_1, \dots, \mathbf{R}_M, S_M) \hat{H}_e \psi_e(\mathbf{r}_1, s_1, \dots, \mathbf{r}_N, s_N) \\ &= \varepsilon(\mathbf{R}_1, S_1, \dots, \mathbf{R}_M, S_M) \psi(\mathbf{x}). \end{aligned} \quad (2.10)$$

From hereon we will consider \hat{H} to be \hat{H}_e , ψ_e to be ψ , and ε to be E . Computing ψ can provide much more information than what is actually needed. Even when reducing the problem to only the relaxation of the electrons, such a calculation can be made in practice only for few electron systems.

2.1.3 Periodic Systems

The correlated nature of electrons within a solid or a molecule can be an obstacle to solving the Schrödinger equation. Bloch's theorem, developed by Felix Bloch, can help us to address this problem because, instead of requiring us to consider an infinite or very large number of electrons, it is only necessary to consider the number of electrons within a periodic unit cell of our system. If the unit cell is repeated until we resemble our original system, then the system is periodic and there exists a corresponding periodic external potential as well. This potential is the same for all translations \mathbf{R}_n ,

$$v_{ext}(\mathbf{r} + \mathbf{R}_n) = v_{ext}(\mathbf{r}), \quad (2.11)$$

where the vector \mathbf{R}_n is a linear combination of the three primitive vectors of the unit cell. In this way

$$\mathbf{R}_n = n_1 \mathbf{a}_1 + n_2 \mathbf{a}_2 + n_3 \mathbf{a}_3, \quad (2.12)$$

where n_i are integers and the periodicity of a lattice is observed with respect to the vectors \mathbf{a}_i . The unit cell therefore is the parallelepiped formed from the primitive vectors and the unit cell volume is then

$$\Omega = |\mathbf{a}_1 \cdot (\mathbf{a}_2 \times \mathbf{a}_3)|. \quad (2.13)$$

The kinetic operator and the Coulomb interactions of the Hamiltonian remain unaffected under the translations \mathbf{R}_n and therefore the Hamiltonian of a periodic system commutes with the translations, meaning that they have the same eigenstates. Moreover, this results in eigenstates that can be labeled according to the translational symmetry. For example, in the specific case of noninteracting electrons in the external potential caused by nuclei as in Eq. 2.11, the wavefunctions

will be given by

$$\left[-\frac{1}{2}\nabla^2 + v_{ext}(\mathbf{r}) \right] \psi_{n,\mathbf{k}}(\mathbf{r}) = \varepsilon_{n,\mathbf{k}} \psi_{n,\mathbf{k}}(\mathbf{r}), \quad (2.14)$$

where such wavefunctions satisfy Bloch's theorem.

Theorem 1 (Bloch's Theorem). For particles in an periodic external potential, there is a basis of wavefunctions which are Bloch's waves that are eigenstates of Schrödinger's equation. Bloch's waves are the product of a plane wave $e^{i\mathbf{k}\cdot\mathbf{r}}$ and a function $u_{n,\mathbf{k}}(\mathbf{r})$ with the same periodicity as the external potential,

$$\psi_{n,\mathbf{k}}(\mathbf{r}) = e^{i\mathbf{k}\cdot\mathbf{r}} u_{n,\mathbf{k}}(\mathbf{r}), \quad (2.15)$$

where the quantum numbers \mathbf{k} and n are the wave vector and the band index, respectively.

The vector \mathbf{k} reflects the periodicity of the system and n corresponds to independent eigenstates of different energies. Furthermore, for any vector \mathbf{k} , there is a complete set of bands n . For instance, the band structure for a solid is equivalent to the eigenvalues $\varepsilon_{n,\mathbf{k}}$ plotted along a specific path in \mathbf{k} -space.

A direct consequence of Bloch's theorem is that all observables of the systems can be Fourier expanded in terms of the reciprocal lattice vectors \mathbf{G}_m ,

$$\mathbf{G}_m = m_1 \mathbf{b}_1 + m_2 \mathbf{b}_2 + m_3 \mathbf{b}_3, \quad (2.16)$$

where m_i are integers and \mathbf{b}_i are the primitive vectors of the reciprocal lattice. These are given by

$$\mathbf{b}_i = 2\pi \frac{\mathbf{a}_j \times \mathbf{a}_k}{\Omega}. \quad (2.17)$$

The relation between the vectors of the unit and the reciprocal lattice cell is then

$$\mathbf{a}_i \cdot \mathbf{b}_j = 2\pi \delta_{ij}, \quad (2.18)$$

so that

$$\exp [i\mathbf{G}_m \cdot (\mathbf{r} + \mathbf{R}_n)] = \exp [i\mathbf{G}_m \cdot \mathbf{r}]. \quad (2.19)$$

The Fourier expansions of v_{ext} and other periodic functions, for example for $u_{n,\mathbf{k}}(\mathbf{r})$, are then

$$u_{n,\mathbf{k}}(\mathbf{r}) = \sum_{\mathbf{m}} e^{i\mathbf{G}_m \cdot \mathbf{r}} u_{n,\mathbf{k}}(\mathbf{G}_m). \quad (2.20)$$

In order to ensure the normalization of Bloch waves in Eq. 2.15, we must restrict the values of \mathbf{k} and the number of particles. To do this, boundary conditions must be set by

$$\psi_{n,\mathbf{k}}(\mathbf{r} + N_i \mathbf{a}_i) = \psi_{n,\mathbf{k}}(\mathbf{r}), \quad (2.21)$$

and we get a restriction for \mathbf{k}_1

$$\mathbf{k}_1 = \frac{l_1}{N_1} \mathbf{b}_1 + \frac{l_2}{N_2} \mathbf{b}_2 + \frac{l_3}{N_3} \mathbf{b}_3 \quad \text{and} \quad -\frac{N_i}{2} \leq l_i < \frac{N_i}{2}, \quad (2.22)$$

where l_i are positive integers. These constrained values of \mathbf{k} correspond to the first Brillouin zone. Furthermore, any value of \mathbf{k} outside this zone can be reduced to the first Brillouin zone.

To perform the calculations using Bloch waves to represent the Kohn-Sham (KS) wavefunctions, a finite number of sampling points in the first Brillouin zone is required. The orbitals vary very smoothly with respect to k and calculations are converged with respect to each one of these sampling points. A Monkhorst-Pack sampling⁶³ of special⁶⁴ k -points is performed as it is an unbiased method to select these points in a equally spaced mesh

$$\mathbf{k}(n_1, n_2, n_3) = \sum_{i=1}^3 \frac{2n_i - N_i - 1}{2N_i} \mathbf{b}_i, \quad (2.23)$$

where $n_i = 1, \dots, N_i$, N_i determines the number of points in the \mathbf{b}_i direction.

The calculation of many properties requires the evaluation of integrals over the Brillouin zone in reciprocal space. This discrete set of \mathbf{k} -points allows us to make an accurate approximation of these integrals⁶⁵. To illustrate, the integral of a function $F(\mathbf{k})$

$$\frac{1}{\Omega_{\text{BZ}}} \int_{\text{BZ}} F(\mathbf{k}) d\mathbf{k} \approx \sum_{\mathbf{k}} w_{\mathbf{k}} F(\mathbf{k}), \quad (2.24)$$

where Ω_{BZ} is the volume of the Brillouin zone, is approximately equal to the weighted sum over the \mathbf{k} -points of the first Brillouin zone.

2.1.4 The Hohenberg-Kohn theorem

One alternative way to reduce the computational effort of considering the positions of all electrons would be to use only the electronic density to calculate the properties we want. The Hohenberg-Kohn theorem tells us why such a different approach can be used. The Hamiltonian in Eq. 2.9

is completely determined by the N electrons and the external potential v_{ext} , and so is the ground state electronic wavefunction ψ_0 .

$$n_0(\mathbf{r}) = \langle \psi_0 | \hat{n} | \psi_0 \rangle = \int |\psi_0(\mathbf{r}, \mathbf{r}_2, \dots, \mathbf{r}_N)|^2 d\mathbf{r}_2 \dots d\mathbf{r}_N. \quad (2.25)$$

The ground state density $n_0(\mathbf{r})$ is a functional of the number of electrons N and the external potential v_{ext} . In the very foundations of density functional theory is the Hohenberg-Kohn theorem⁶⁶.

Theorem 2 (Hohenberg-Kohn). The ground state electronic density $n_0(\mathbf{r})$ is uniquely determined by the corresponding external potential $v_{ext}(\mathbf{r})$, to within an additive constant.

The proof to this theorem is very simple and can be found in Ref. 61. Moreover, the ground state is a unique functional of the ground state density

$$|\psi_0\rangle = |\psi[n_0]\rangle. \quad (2.26)$$

Such a functional dependence can be extremely complicated. The existence of this functional means any ground state observable is also a density functional,

$$O[n] \equiv \langle \psi[n] | \hat{O} | \psi[n] \rangle. \quad (2.27)$$

In particular, this holds for the ground state energy, which will be the most important density functional,

$$\begin{aligned} E[n] &\equiv \langle \psi[n] | \hat{H} | \psi[n] \rangle = F[n] + \int d^3\mathbf{r} v_{ext}(\mathbf{r}) n(\mathbf{r}), \\ F[n] &\equiv \langle \psi[n] | (\hat{T}_e + V_{e-e}) | \psi[n] \rangle. \end{aligned} \quad (2.28)$$

In Eq. 2.28 $F[n]$ corresponds to a universal part and v_{ext} enters into $E[n]$ at only one point.

Another fundamental part of density functional theory (DFT) is the minimum principle for the ground state energy functional $E[n]$. For all densities $n'_0(\mathbf{r}) \neq n_0(\mathbf{r})$, such that n_0 is the ground state density corresponding to v_{ext} ,

$$E[n_0] < E[n'_0] \iff E_0 = \min_{n \in \mathcal{N}} E[n], \quad (2.29)$$

where \mathcal{N} is the set of all ground state densities corresponding to different v_{ext} . The latter principle is a direct consequence of the Ritz variational principle, that is, the ground state $|\psi'_0\rangle$ corresponding to n'_0 is not the same as $|\psi_0\rangle$. The functional $E[n]$ has its domain restricted to only densities in \mathcal{N} , as obtained by solving Eq. 2.9⁶⁷. The energy functional can be rewritten as

$$E[n] = T[n] + E_H[n] + E_{ext}[n] + E_{xc}[n], \quad (2.30)$$

that is, as the sum of the kinetic energy functional $T[n]$, the Hartree interaction energy functional $E_H[n]$, the external potential energy functional $E_{ext}[n]$ and the exchange and correlation (xc) energy functional $E_{xc}[n]$. The xc functional accounts for the complicated effects of the interactions not present in T , E_H , or E_{ext} .

2.1.5 Kohn-Sham Self-consistent Field Procedure

The basic idea behind DFT is to introduce an exact mapping of the interacting many-body problem onto a suitable non-interacting system, the Kohn-Sham (KS) system⁶⁸. This fictitious system of non-interacting electrons should have a ground state density that is the same as the density of the fully interacting system. Through the KS self-consistent field procedure, the ground state density $n_0(\mathbf{r})$, energy E_0 , and forces \mathbf{F}_I between the electrons can be found. The KS scheme has five steps:

1. An initial guess n_0 for the trial density $\tilde{n}(\mathbf{r})$ is made.
2. The effective potential

$$v_{eff}[\tilde{n}](\mathbf{r}) = v_{ext}(\mathbf{r}) + \int \frac{\tilde{n}(\mathbf{r}')}{|\mathbf{r} - \mathbf{r}'|} d^3\mathbf{r}' + v_{xc}[\tilde{n}](\mathbf{r}), \quad (2.31)$$

is calculated, where $v_{ext}(\mathbf{r})$ is the external potential due to the nuclei, the second term corresponds to the Hartree potential from the other electrons, and the third term v_{xc} is the exchange and correlation (xc) potential. The Hartree⁶⁹ potential's source is the average density of the electrons, and the exchange and correlation term includes corrections to the kinetic energies and electron-electron interactions. v_{xc} is the difference between Hamiltonians that describe the interacting electrons and the KS system.

3. The single-electron Schrödinger equation is solved to obtain the KS wavefunctions φ_i . The effective potential is a functional of the trial density:

$$\left(-\frac{1}{2}\nabla^2 + v_{\text{eff}}[\tilde{n}](\mathbf{r}) - \epsilon_i\right)\varphi_i(\mathbf{r}) = 0. \quad (2.32)$$

4. A new trial density $\tilde{n}'(\mathbf{r})$ is calculated with the KS wavefunctions from the last step. To obtain the density only the $N/2$ lowest eigenfunctions φ_i are summed, where we have assumed the system is spin-paired

$$\tilde{n}'(\mathbf{r}) = 2 \sum_{i=1}^{N/2} |\varphi_i|^2. \quad (2.33)$$

5. Steps (2), (3), and (4) are repeated until the density is converged, that is, the trial density $\tilde{n}'(\mathbf{r})$ is approximately equal to $\tilde{n}(\mathbf{r})$, the previous density from Eq. 2.33, within a defined accuracy. When this is achieved, we have a “final” density $n(\mathbf{r})$ with the corresponding eigenenergies ϵ_i . The cycle is also shown schematically in Fig. 2.1.

The KS wavefunctions φ_i result in the density of our system and $\epsilon_{N/2}$, the eigenvalue corresponding to the highest occupied molecular orbital (HOMO), is the ionization energy. The ground state energy E_0 can be calculated from the outputs of the KS scheme using

$$E_0 = \sum_{i=1}^{N/2} \epsilon_i + E_{xc}[n] - \int v_{\text{ext}}(\mathbf{r})n(\mathbf{r})d^3\mathbf{r} + \frac{1}{2} \iint \frac{n(\mathbf{r})n(\mathbf{r}')}{|\mathbf{r} - \mathbf{r}'|} d^3\mathbf{r}d^3\mathbf{r}'. \quad (2.34)$$

It is important to mention that, so far, the exchange and correlation potential v_{xc} only has an exact expression for systems with few atoms. This means that, in the case of a many-body problem, the exchange and correlation potential functional must be approximated.

Finally, in order to find the relaxed structure of certain system it is necessary to minimize the forces of its atoms, the force acting on an atom at \mathbf{R}_I is $\mathbf{F}_I = -\nabla_I E[n]^{67}$, which, by the Hellman-Feynman theorem⁷¹, can be also calculated as $\mathbf{F}_I = -\langle \psi_0(\mathbf{R}) | \nabla_I H(\mathbf{R}) | \psi_0 \rangle$. That is, we can obtain the forces from the ground state wavefunctions which were already calculated for the energy. Let us recall that the total energy depends parametrically on the positions of the nuclei.

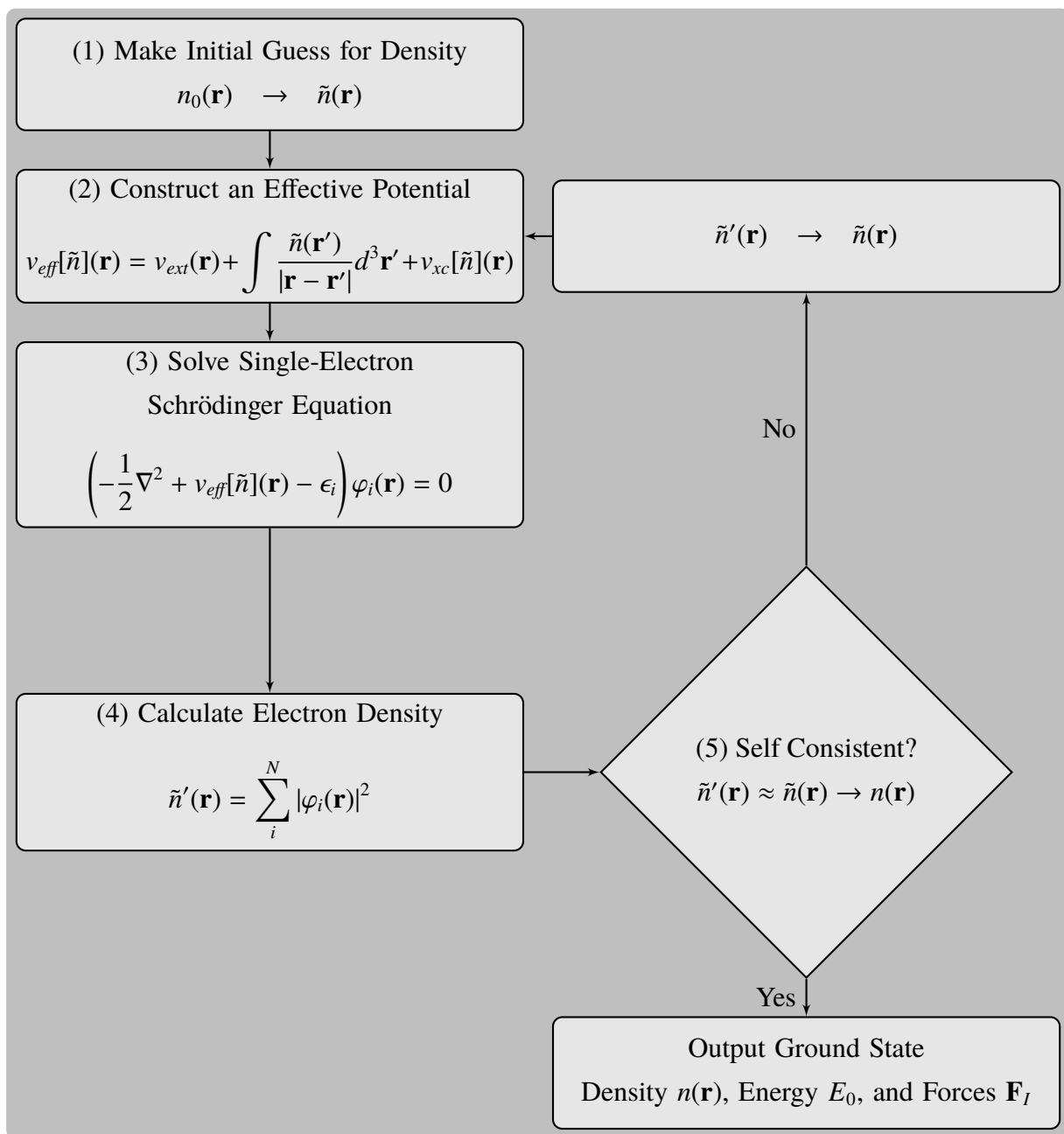


Figure 2.1: Kohn-Sham self-consistent scheme. Adapted from Ref. 70.

2.1.6 Exchange and correlation Functionals

Although it is a basic requirement for DFT to obtain the ground state energy, the exact form of the functional $E_{xc}[n]$ is unknown. Numerical approximations must therefore be made, e.g., using Monte Carlo simulations.

Local-density approximation

One of the first approaches to estimate the xc-energy functional was proposed by Perdew and Zunger⁷². They considered a local-density approximation (LDA) in which the xc-energy of the system in question, with density $n(\mathbf{r})$, is locally approximated by the xc-energy of a homogeneous (or uniform) electron gas (HEG), with density $n(\mathbf{r}) = n_0$. The HEG is a system of interacting electrons that do not experience a spatially varying external potential. The LDA xc-energy density is then

$$E_{xc}^{\text{LDA}}[n] = \int \epsilon_{xc}^{\text{HEG}}(n_0 = n(\mathbf{r})) d^3 \mathbf{r}. \quad (2.35)$$

As discussed in Ref. 67, the LDA is often used in the KS scheme because the corresponding xc-potential is simply a function of the local density,

$$v_{xc}^{\text{LDA}}(\mathbf{r}) = \frac{\delta E_{xc}^{\text{LDA}}[n]}{\delta n(\mathbf{r})}. \quad (2.36)$$

Physically, the v_{xc}^{LDA} has an extremely short range because it only depends on the local density. The LDA ignores corrections to the xc-energy due to inhomogeneities, but it is successful despite this severe approximation. It has been used in DFT for decades producing an overwhelming number of results throughout the literature. This is because LDA respects the sum rule that one electron is excluded from the immediate vicinity of a given electron. Also, although LDA generally underestimates the exchange energy and overestimates the correlation energy, these errors tend to cancel each other. A known disadvantage of the LDA is its the over binding of molecules⁷³.

Generalized gradient approximation

In order to take into account non-homogeneities in the electron density, a semi-local approximation that depends on the gradient of the density is often used. This generalized gradient approximation (GGA) is based on how the density changes away from the coordinate. The GGA exchange functional generally takes the form⁷⁴

$$E_x^{\text{GGA}}[n] = \int \epsilon_x^{\text{HEG}}(n_0 = n(\mathbf{r})) F_x[s(\mathbf{r})] d^3\mathbf{r}, \quad (2.37)$$

where $n(\mathbf{r})$ is the electronic density, ϵ_x^{HEG} is the exchange energy density of a HEG ($\sim n^{4/3}$), F_x is an enhancement factor, and s is the dimensionless density gradient

$$s = \frac{|\nabla n|}{2k_F n}, \quad (2.38)$$

with $k_F = (3\pi^2 n)^{1/3}$. Eq. 2.37 is spin-unpolarized but a spin-polarized version may also be deduced⁷⁴. The enhancement for any GGA that recovers the HEG limit is

$$F_x[s] = 1 + \mu s^2 + \dots \quad (s \rightarrow 0) \quad (2.39)$$

Similarly, the gradient expansion for the correlation functional that recovers the HEG limit is

$$E_c^{\text{GGA}}[n] = \int n(\mathbf{r}) \left\{ \epsilon_c^{\text{HEG}}[n(\mathbf{r})] + \frac{\pi k_F}{2} \beta s^2[n(\mathbf{r})] + \dots \right\} d^3\mathbf{r}, \quad (2.40)$$

where ϵ_c^{HEG} is the correlation energy of the HEG and β is a coefficient. GGA functionals used to be parametrized by fitting experimental data and were therefore restricted to certain systems. However, parameter-free functionals can be used in a wide range of systems. One example of these is the functional developed by Perdew, Burke, and Ernzerhof (PBE)⁷⁴.

PBE GGA

The parameters used in the PBE functional are rather fundamental constants and are defined as

$$\mu = 0.21951 \text{ and } \beta = 0.0066725. \quad (2.41)$$

The PBE functional was used in this thesis and it includes the linear response of the uniform gas, correct behavior under uniform scaling, and a smoother potential. The physical ideas of PBE and the consequences for practical calculations are found in Refs. 75 and 76.

PBEsol GGA

The PBEsol functional is a revised PBE GGA that improves equilibrium properties of densely-packed solids and their surfaces⁷⁷. For this functional, the same form as PBE is used but the parameters are set to

$$\mu = \mu_{GE} = 0.1235 \text{ and } \beta = 0.046, \quad (2.42)$$

where μ_{GE} is used to obtain an accurate gradient expansion for slowly varying electrons. PBEsol reduces the dependence on error cancellation by providing a more accurate accurate description for both exchange and correlation energies of surfaces. The performance of PBEsol for solids is assessed in Ref. 77.

2.1.7 Derivative Discontinuity

Energy functionals are defined only for an integer number of electrons, N . In Ref. 67, the energy functional for fractional particle numbers is derived as the statistical superposition of the lowest energies of the two states $|\psi_N\rangle$ and $|\psi_{N+1}\rangle$,

$$E_f[n] \equiv F_f + \int d^3\mathbf{r} v_{ext}(\mathbf{r})n(\mathbf{r}) \quad (2.43)$$

$$F_f[n] \equiv \min_{\psi_N, \psi_{N+1}} \left\{ (1 - \eta) \langle \psi_N | (\hat{T}_e + V_{e-e}) | \psi_N \rangle + \eta \langle \psi_{N+1} | (\hat{T}_e + V_{e-e}) | \psi_{N+1} \rangle \right\}, \quad (2.44)$$

where $0 < \eta < 1$, and the search of the minimum is restricted by the density

$$n(\mathbf{r}) = (1 - \eta) \langle \psi_N | \hat{n}(\mathbf{r}) | \psi_N \rangle + \eta \langle \psi_{N+1} | \hat{n}(\mathbf{r}) | \psi_{N+1} \rangle. \quad (2.45)$$

For fractional particle numbers, the variational equation that determines the ground state density is well-defined because $F_f[n]$ exists for any density that integrates up to $N + \eta$,

$$\frac{\delta E_f[n]}{\delta n(\mathbf{r})} = \mu_L, \quad (2.46)$$

where μ_L is the Levy-Lieb functional. This functional is identical to the chemical potential for integer particle number

$$\mu(N) = \frac{\partial E}{\partial N}(N), \quad (2.47)$$

where the total energy $E(N + \eta)$ corresponds to the minimum of the energy functional of a fractional particle number,

$$E(N + \eta) = \min_n E_f[n]. \quad (2.48)$$

The minimum in Eq. 2.48 is obtained when n is a superposition of the ground state densities of the N -particle system n_N and of the $(N + 1)$ -particle system n_{N+1} ,

$$n(\mathbf{r}) = (1 - \eta)n_N(\mathbf{r}) + \eta n_{N+1}(\mathbf{r}). \quad (2.49)$$

The total energy of a system with $N + \eta$ particles is also the superposition of the total energy of a system of N particles and a system of $N + 1$ particles resulting in,

$$E(N + \eta) = (1 - \eta)E(N) + \eta E(N + 1). \quad (2.50)$$

It can be seen in Fig. 2.2 that the total energy for a fractional number of particles is a linear function between two integer particle numbers.

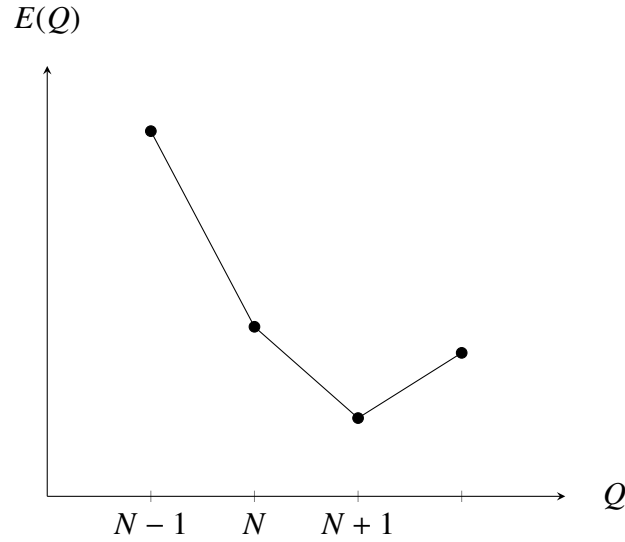


Figure 2.2: Total energy $E(Q)$ in as a function of the fractional particle number Q .

The chemical potential is the slope of the piecewise linear curve $E(Q)$. For this reason, the ionization potential (IP) and the electron affinity (EA) are given simply by

$$\mu(N - \eta) = E^N - E^{N-1} = -\text{IP} \quad (2.51)$$

$$\mu(N + \eta) = E^{N+1} - E^N = -\text{EA}. \quad (2.52)$$

As a consequence of the form of the total energy, the chemical potential $\mu(N)$, that is the derivative of the energy with respect to the number of particles, is discontinuous at all integer particle numbers. Recalling Eq. 2.46, the last statement implies that the functional derivative of the total energy functional $E_f[n]$ must also have discontinuities for integer particle numbers. These are called derivative discontinuities.

2.1.8 Band Gap

The fundamental band gap E_g is defined as the difference between two binding energies: one for the most weakly bound electron in the ground state of the semiconductor and the other for the most weakly bound electron in the ground state of the system by adding one electron. For an N -electron system, the fundamental band gap is

$$E_g = -\{[E_0^N - E_0^{N-1}] - [E_0^{N+1} - E_0^N]\}, \quad (2.53)$$

where the sign convention guarantees that the band gap energy is positive. This corresponds to the difference in energy between the $(N + 1)$ th electron belonging to the conduction band minimum (CBM) and the N th electron in the valence band maximum (VBM). For a KS system, the ionization energies are the same as the orbital energies, that is, $E_0^N - E_0^{N-1} = \varepsilon_N$ and the band gap for the non-interacting system is

$$\Delta_{KS} = \varepsilon_{N+1} - \varepsilon_N. \quad (2.54)$$

By using Eqs. 2.51 and 2.52 the fundamental band gap can be rewritten as

$$E_g = \text{IP} - \text{EA} = \lim_{\eta \rightarrow 0^+} \{\mu(N + \eta) - \mu(N - \eta)\}. \quad (2.55)$$

By using the variational equation, Eq. 2.46, this expression becomes

$$E_g = \lim_{\eta \rightarrow 0^+} \left\{ \left. \frac{\delta E[n]}{\delta n(\mathbf{r})} \right|_{N+\eta} - \left. \frac{\delta E[n]}{\delta n(\mathbf{r})} \right|_{N-\eta} \right\}, \quad (2.56)$$

and may be evaluated at the ground state density of the $N + \eta$ particles. Decomposing the energy functional as in Eq. 2.30 and as E_{ext} and E_H have a continuous dependence on the particle number, the band gap becomes

$$\begin{aligned} E_g &= \lim_{\eta \rightarrow 0^+} \left\{ \left[\left. \frac{\delta T[n]}{\delta n(\mathbf{r})} \right|_{N+\eta} - \left. \frac{\delta T[n]}{\delta n(\mathbf{r})} \right|_{N-\eta} \right] + \left[\left. \frac{\delta E_{xc}[n]}{\delta n(\mathbf{r})} \right|_{N+\eta} - \left. \frac{\delta E_{xc}[n]}{\delta n(\mathbf{r})} \right|_{N-\eta} \right] \right\} \\ &= \Delta_{KS} + \Delta_{xc}, \end{aligned} \quad (2.57)$$

because T is the part of the KS system which has a derivative discontinuity. Finally, the band gap is the difference between the lowest unoccupied KS orbital and the highest occupied KS orbital, plus the contribution of the xc derivative discontinuity.

$$E_g = \varepsilon_{N+1} - \varepsilon_N + \Delta_{xc}. \quad (2.58)$$

2.1.9 GLLB-SC to Describe Band Gaps

The KS band gap differs from the experimental band gap by the derivative discontinuity Δ_{xc} , which can be of the same order of magnitude as the KS band gap, $\Delta_{KS} = \varepsilon_{N+1} - \varepsilon_N$. Δ_{xc} is always positive and Δ_{KS} is thus smaller than E_g . For this reason, comparison with experimental values should only be done when the derivative discontinuity is added to the KS band gap⁷⁸. The xc potential can be tuned to obtain a better agreement of Δ_{KS} with the experimental values, but this can lead to a potential that has unphysical features, resulting in a poor description of other properties that are not the band gap⁷⁹. In Ref. 80, they calculated the exchange part of the derivative discontinuity Δ_x from the KS equations by using a modified version of the Gritsenko, van Leeuwen, van Lenthe, and Baerends (GLLB) xc potential^{81,82}. This xc potential exhibits a step structure at the lowest unoccupied orbital when it starts to be occupied. A newer version of this potential is called GLLB-SC, for solid and correlation, and has been shown to yield a better

agreement with the experimental band gaps than LDA or GGA for solids⁸³. The expression for the derivative discontinuity for the GLLB-SC is

$$\Delta_x^{GLLB-SC} = \left\langle \varphi_{\text{CBM}} \left| \sum_{n=1}^{N/2} \frac{8\sqrt{2}}{3\pi^2} \left(\sqrt{\epsilon_{\text{CBM}} - \epsilon_n} - \sqrt{\epsilon_{\text{VBM}} - \epsilon_n} \right) \frac{|\varphi_n(\mathbf{r})|^2}{n(\mathbf{r})} \right| \varphi_{\text{CBM}} \right\rangle, \quad (2.59)$$

where φ_{CBM} and φ_n are the CBM and the n th KS wavefunctions, respectively, and ϵ_{CBM} , ϵ_{VBM} , and ϵ_n are the eigenenergies of the CBM, VBM, and the n th states, respectively. The potential varies abruptly when φ_{CBM} starts to be occupied by an infinitesimal amount η .

2.2 Representations of the KS wavefunctions

In DFT calculations, generally one of three types of representations of the KS wavefunctions are used: real space, plane waves (PWs), or linear combinations of atomic orbitals (LCAOs). In real space representations the wavefunctions are directly sampled at a finite number of grid points, whereas in PW or LCAO representations, the wavefunctions are expanded in either a plane wave or atomic orbital basis set, respectively.

A wavefunction is an element of a Hilbert space, that is, a vector space with an inner product. States are represented as elements of this vector space and therefore can be expressed as a linear combination of basis vectors. Moreover, any state ψ can be expressed as the linear combination of vectors of a complete basis set $\{\phi_\mu\}$

$$\psi_n = \sum_{\mu} c_{n,\mu} \phi_{\mu}. \quad (2.60)$$

In practice, a truncated basis set is used to expand the wavefunctions and find the solution to the KS equation in such a way that a finite matrix is employed to solve the eigenvalue problem. In this section, a very brief review of each one of the representations is done.

2.2.1 Real space

The values of wavefunctions, electron densities, and potentials on a discrete grid of finite points in real space can be used to represent them^{84–87}. Also, the kinetic operator of the Hamiltonian

contains the Laplacian operator which involves derivatives that can be approximated by finite difference (FD) techniques⁸⁸. The accuracy of this method can be systematically improved by increasing the number of grid points, i.e., decreasing the spacing of the grid. One of the advantages of this method is its flexibility when imposing boundary conditions: they can be either periodic, non-periodic, or a mixture of the two. Furthermore, real-space calculations can be parallelized on different processors by domain decomposition. The real space or FD representation of the KS wavefunctions cannot be easily scaled up to perform calculations that involve very large molecules with a great number of atoms.

2.2.2 Plane Waves

As we have seen in section 2.1.3, plane waves can constitute a complete basis set that spans the KS wavefunctions. For a given unit cell of volume Ω ,

$$u_n(\mathbf{r}) = \frac{1}{\sqrt{\Omega}} \sum_{\mathbf{G}} \tilde{u}_{n,\mathbf{G}} e^{i\mathbf{G}\cdot\mathbf{r}}. \quad (2.61)$$

In this way, the KS wavefunctions can be represented in terms of the coefficients $\tilde{u}_{n,\mathbf{G}}$, and the quality of this description is systematically improved by inclusion of more reciprocal lattice vectors, \mathbf{G} , in the sum of Eq. 2.61. However, a PW expansion of the KS wavefunctions cannot be domain decomposed, as is possible for real space calculations.

2.2.3 Linear Combination of Atomic Orbitals

Another basis set that can be used to represent the KS wavefunctions is a linear combination of atomic orbitals (LCAO). This approximation is widely used in *ab initio* calculations based on the idea that the molecular orbitals of a given system can be built from the orbitals of its constituent atoms⁸⁹. The representation of the KS wavefunctions as a linear combination of atom-centered functions has proven to be useful in large systems with many atoms per unit cell or with vacuum regions where plane waves become expensive to use⁹⁰. For instance, the GPAW code employs LCAOs as basis within the projector-augmented wave (PAW) method⁹¹.

An atomic orbital centered on atom a , $\phi_{nlm}^a(r, \theta, \varphi)$, is the product of a numerical radial function $\zeta_{nl}(r)$ and a spherical harmonic $Y_{lm}(\theta, \varphi)$,

$$\phi_{nlm}^a = \zeta_{nl}(r)Y_{lm}(\theta, \varphi), \quad (2.62)$$

where $\{r, \theta, \varphi\}$ are the spherical coordinates of the nucleus a where the wavefunctions are centered. So μ in Eq. 2.60 corresponds to n, l , and m , the three quantum numbers of a state. This basis set is obtained by solving the radial all-electron KS equations for isolated atoms^{92,93}. The detailed procedure to generate LCAO basis functions can be found in Ref. 94.

2.2.4 Naming convention of LCAO basis sets

LCAO basis sets are named following the number of basis functions used for each element^{91,95}. In this way, for the minimal or single- ζ (SZ) basis set, one radial function $\zeta_{nl}(r)$ for each occupied valence orbital, $|nl\rangle$ is used. Likewise, multiple- ζ sets are obtained by generating multiple functions by the split valence technique for each occupied valence orbital⁹⁶. For instance, the SZ basis set for a hydrogen atom has one s -type function and the DZ basis set for a carbon atom has two s -type functions and 2×2 p -type functions.

Multiple-Zeta orbitals improve the radial flexibility of the basis set and polarization functions that have higher angular momentum l improve the angular flexibility. A polarized basis set has a function with angular momentum $l + 1$ where l is the highest occupied valence orbital. For example, a DZP basis for oxygen has 8 functions from the DZ part and 5 functions from the polarized part which is a d -type orbital⁹⁵.

2.3 Projector Augmented Wave Method

In order to solve the KS equations using efficient numerical methods, some approximations are made. These are related to the different behavior of wavefunctions in different regions of real space, i.e., close to and away from the nucleus. These are the pseudopotential and all-electron methods.

The usage of a pseudopotential and pseudowavefunctions is an approximation based on the observation that core electrons, the ones closest to the atomic nucleus, are relatively unaffected by the chemical environment. This means that the binding energy of the core electrons in isolated atoms and in atoms that are brought together, like in molecules, is approximately the same. Also, the total binding energy depends mostly on the energy of valence electrons. Another motivation for treating core and valence electrons differently is that the strong nuclear Coulomb potential and the highly localized core electrons states are difficult to represent computationally⁹⁷.

All the atomic wavefunctions, either core or valence, should be mutually orthogonal because they are derived from the same atomic Hamiltonian. Because the core states are highly localized in the vicinity of the nucleus, the valence wavefunctions must oscillate very rapidly in this region in order to maintain their orthogonality. Keeping in mind that the kinetic energy is proportional to second spatial derivatives of the wavefunction and therefore to the magnitude of the curvature, these rapid oscillations of the valence wavefunctions result in a large kinetic energy of the valence electrons near the nucleus. This kinetic energy roughly cancels out the potential energy corresponding to the Coulomb potential and this is why valence electrons are less bound than core electrons. Because of this, it is convenient to replace the strong Coulomb potential and core electrons by a pseudopotential⁹⁸ that is smooth and reproduces the effect of the potential and core electrons on the valence electrons. The KS equations are then solved only for the valence electrons using pseudopotentials that are calculated and tabulated once for each element. Drawbacks of this approximation include that information of wavefunctions near the nucleus is lost and it is not a simple procedure to generate accurate pseudopotentials.

In the other approach or all-electron methods, the full information of the wavefunction is available. This is achieved by using the frozen core approximation in which the orbitals of the core electrons are fixed. These core orbitals are calculated and tabulated once. The frozen core approximation is also motivated by the fact that the core electrons are inert for most purposes. The Augmented-Plane-Wave (APW) is one of the all-electron methods in which the space is divided into two regions: one spherical region centered at each atom where the wavefunction is expanded into a local basis, and an interstitial region between the spheres where another basis set is used, e.g., plane waves. The two basis are connected at the boundaries of the two regions⁹⁹.

A more general approach is the Projector Augmented Wave method (PAW)¹⁰⁰ in which APW is a special case¹⁰¹, and the pseudopotential method is a well defined approximation¹⁰². This method is implemented using the GPAW⁵⁸ code in all the calculations presented in this thesis. The PAW method establishes a linear transformation $\hat{\mathcal{T}}$ that maps the physical valence wavefunctions ψ_n onto computationally convenient fictitious pseudowavefunctions $\tilde{\psi}_n$,

$$\psi_n = \hat{\mathcal{T}} \tilde{\psi}_n, \quad (2.63)$$

where n is a quantum state label, that is a band, spin, or k -vector index. The transformation operator is given by

$$\hat{\mathcal{T}} = 1 + \sum_a \sum_i (|\phi_i^a\rangle - |\tilde{\phi}_i^a\rangle) \langle \tilde{p}_i^a|, \quad (2.64)$$

where ϕ_i^a are the atom-centered partial waves used to expand the all-electron wavefunction within the atom-centered sphere or augmentation region, so that $|\psi_n\rangle = \sum_{ai} c_{ni}^a |\phi_i^a\rangle$, $\tilde{\phi}_i^a$ are the corresponding partial waves used to expand the pseudowavefunctions, and \tilde{p}_i^a are projector functions.

The pseudo partial waves coincide with the corresponding true partial wave outside the augmentation region and are smooth continuations inside the augmentation region. The projector function for each pseudo partial wave is localized within the augmentation region and fulfills the condition $\langle \tilde{p}_i^a | \tilde{\phi}_j^a \rangle = \delta_{ij}$ inside the sphere. In order to make the PAW method a practical scheme some approximations are needed. These include the frozen core approximation, where no projector functions are needed for the core states, and employing a finite number of partial waves and projectors.

2.4 Time-Dependent Density Functional Theory

Time-dependent density functional theory (TDDFT) gives access to excited states and to time-dependent processes, like transport phenomena and conduction in the quantum regime¹⁰³. In this section we are going to describe the basic ideas behind TDDFT, that is, the Runge-Gross theorem and linear response within TDDFT. Other aspects of this theory, such as the time-dependent

Kohn-Sham equations and the adiabatic local density approximation (ALDA), are addressed in previous works such as Refs. 67 and 104.

2.4.1 Runge-Gross Theorem

The Runge-Gross theorem is the analog of the Hohenberg-Kohn theorem for time dependent systems. It establishes a map from the time dependent many-particle state to the corresponding time dependent density. The evolution of the wavefunction is ruled by the time dependent Schrödinger equation

$$\hat{H}(t)\psi(t) = i\frac{\partial\psi(t)}{\partial t}, \quad (2.65)$$

with an initial state at time t_0

$$\psi(t_0) = \psi_0, \quad (2.66)$$

where the Hamiltonian is

$$\hat{H}(t) = \hat{T} + \hat{V}_{ext}(t) + \hat{W}. \quad (2.67)$$

For all systems of interest, \hat{W} is the particle-particle Coulomb interaction and $\hat{V}_{ext}(t)$ is the coupling between the particle density and a time-dependent potential $v_{ext}(\mathbf{r}, t)$,

$$\hat{V}_{ext}(t) = \sum_i^N v_{ext}(\mathbf{r}_i, t) = \int d^3\mathbf{r} v_{ext}(\mathbf{r}, t) \hat{n}(\mathbf{r}). \quad (2.68)$$

As the system evolves in time, its density also changes, as given by

$$n(\mathbf{r}, t) = N \int d^3\mathbf{r}_2 \dots \int d^3\mathbf{r}_N |\psi(\mathbf{r}, \mathbf{r}_2, \dots, \mathbf{r}_N, t)|^2, \quad (2.69)$$

and is normalized to yield the number of electrons, $\int d^3\mathbf{r} n(\mathbf{r}, t) = N$.

Theorem 3 (Runge-Gross). Two densities $n(\mathbf{r}, t)$ and $n'(\mathbf{r}, t)$ evolving from the same initial state ψ_0 under the influence of two potentials $v_{ext}(\mathbf{r}, t)$ and $v'_{ext}(\mathbf{r}, t)$, both Taylor expandable about t_0 , eventually differ if the potentials differ by more than a purely time-dependent function, that is, $v_{ext}(\mathbf{r}, t) - v'_{ext}(\mathbf{r}, t) \neq c(t)$ ¹⁰⁵.

Based on this theorem, there is an injective mapping between densities and potentials under these conditions. This means that the potential is a functional of the density. Having this relation, a fictitious system of noninteracting electrons that satisfies the time-dependent Kohn-Sham equations,

$$i\frac{\partial\varphi_n(\mathbf{r},t)}{\partial t} = \left[-\frac{\nabla^2}{2} + v_{\text{eff}}[n](\mathbf{r},t) \right] \varphi_n(\mathbf{r},t), \quad (2.70)$$

has the same density as the real system and the effective potential v_{eff} yielding this density is unique. The exchange and correlation potential is defined as Eq. 2.31 of the time independent case and is also a functional of the time-dependent density as well of the initial KS wavefunction $\varphi(t_0)$.

In contrast to time-independent DFT, the total energy cannot be obtained by minimization of the energy functional because the total energy is not a conserved quantity. Also, finding the full solution of the TDKS equations can be computationally expensive for large systems. A different way to calculate time-dependent properties like excitation energies, transition moments, and polarizabilities, is to use linear response within TDDFT.

2.4.2 Linear Density Response

In most situations of interest, systems are subjected to small perturbations and do not deviate strongly from their initial state. This is the case for most spectroscopy applications, where the response to a weak probe is used to study the spectral properties of a system. In these cases, one can use perturbation theory instead of seeking a complete solution to the TDKS equations. Using linear response, the change of a particular variable or observable can be directly calculated up to first order in the perturbation¹⁰⁶. This can be achieved without calculating the change of the wave function. In this thesis, we are employing linear density response in our calculations.

Let us consider the case where a system is in the ground state and a time-dependent scalar potential is activated at time t_0

$$v(\mathbf{r},t) = v_0(\mathbf{r}) + \lambda\Theta(t-t_0)v_1(\mathbf{r},t), \quad (2.71)$$

where $\lambda \in [0, 1]$ denotes the order of the potential perturbation, and $\Theta(t)$ is the Heavyside step

function. That is, the potential is static, $v_0(\mathbf{r})$, until time t_0 . After t_0 the time-dependent additional, but small, perturbation potential $v_1(\mathbf{r}, t)$ is switched on. The potential couples to the density in the following time-dependent Hamiltonian which describes the perturbation

$$\hat{H}_1(t) = \int d^3\mathbf{r}' v_1(\mathbf{r}', t) \hat{n}(\mathbf{r}'). \quad (2.72)$$

The potential causes small time-dependent changes in the system and specifically in the density which can be expanded as

$$n(\mathbf{r}, t) = n_0(\mathbf{r}) + \lambda n_1(\mathbf{r}, t) + \lambda^2 n_2(\mathbf{r}, t) + O(\lambda^3), \quad (2.73)$$

where n_0 is the ground state density, that is, the same as before the perturbative potential was turned on, n_1 is the linear density response, and n_2 is the second-order density response. n_1 is the first-order change induced by v_1 whereas n_2 is the quadratic one in λ . As the perturbation is small, the linear density response dominates over the other higher order terms. Due to norm conservation, the contributions to the density response must integrate to zero.

Using the first-order approximation to the time evolution operator corresponding to the Hamiltonian 2.72 and the interaction picture representation of operators, the linear response of the density can be expressed as

$$n_1(\mathbf{r}, t) = \int_{-\infty}^{\infty} dt' \int d^3\mathbf{r}' \chi(\mathbf{r}, t, \mathbf{r}', t') v_1(\mathbf{r}', t'), \quad (2.74)$$

where $\chi(\mathbf{r}, t, \mathbf{r}', t')$ is the density-density response function defined as¹⁰⁴

$$\chi(\mathbf{r}, t, \mathbf{r}', t') = -i\Theta(t - t') \langle \psi_0 | [\hat{n}(\mathbf{r}, t - t'), \hat{n}(\mathbf{r}')] | \psi_0 \rangle. \quad (2.75)$$

Equation 2.74 can be interpreted as the response of a system at position \mathbf{r} and at time t , caused by the sum of the small perturbations at positions \mathbf{r}' and (earlier) times t' . Equation 2.75 depends on the ground state wavefunction ψ_0 of the system and, due to the Hohenberg-Kohn theorem, the response function is a functional of the ground state density, $\chi[n_0]$.

It is often advantageous to work with the linear density response in frequency space rather than in real time. This is key to extract excitation energies of a system from its linear response.

The linear response of the density in frequency space is

$$n_1(\mathbf{r}, \omega) = \int d^3\mathbf{r}' \chi(\mathbf{r}, \mathbf{r}', \omega) v_1(\mathbf{r}', \omega), \quad (2.76)$$

where the Fourier transform of the response function, $\chi(\mathbf{r}, \mathbf{r}', \omega)$, is

$$\chi(\mathbf{r}, \mathbf{r}', \omega) = \lim_{\eta \rightarrow 0^+} \sum_{n=1}^{\infty} \left\{ \frac{\langle \psi_0 | \hat{n}(\mathbf{r}) | \psi_n \rangle \langle \psi_n | \hat{n}(\mathbf{r}') | \psi_0 \rangle}{\omega - \Omega_n + i\eta} - \frac{\langle \psi_0 | \hat{n}(\mathbf{r}') | \psi_n \rangle \langle \psi_n | \hat{n}(\mathbf{r}) | \psi_0 \rangle}{\omega + \Omega_n + i\eta} \right\}, \quad (2.77)$$

what is called the Lehmann representation, and $\Omega_n = E_n - E_0$ is defined as the n th excitation energy of the system. In equation 2.77, it can be observed that the response function has poles at the excitation energies of the many-body system. That is, if the frequency of the perturbation matches an excitation energy, the response of the system will be large and we will eventually obtain a peak in the spectrum with half width at half maximum η .

Linear density response of the Kohn-Sham system

Based on the Runge-Gross and Hohenberg-Kohn theorems, we can formally express, the time-dependent density as a functional of the effective KS potential and hence of the external potential without any dependence on the initial many-body state:

$$n(\mathbf{r}, t) = n[v_{eff}[v_{ext}]]. \quad (2.78)$$

Then the linear density response n_1 will be given by the linearized effective KS potential following Eq. 2.74. Here the density-density response function for the non-interacting KS system can be expressed as

$$\chi^0(\mathbf{r}, t, \mathbf{r}', t') = \left. \frac{\delta n[v_{eff}](\mathbf{r}, t)}{\delta v_{eff}(\mathbf{r}', t')} \right|_{v_{eff}[n_0](\mathbf{r})}, \quad (2.79)$$

where the linearized effective KS potential, i.e., the effective potential of order λ , is

$$v_{eff1}[n](\mathbf{r}, t) = v_{ext1}(\mathbf{r}, t) + \int d^3\mathbf{r}' \frac{n_1(\mathbf{r}', t)}{|\mathbf{r} - \mathbf{r}'|} + v_{xc1}(\mathbf{r}, t). \quad (2.80)$$

Within the framework of TDDFT, we must calculate self-consistently the linear density response of the non interacting Kohn-Sham system to an effective perturbation, since the linearized

effective potential in Eq. 2.80 depends on $n_1(\mathbf{r}, t)$. The KS response function in terms of the frequency is given by

$$\chi^0(\mathbf{r}', \mathbf{r}, \omega) = \lim_{\eta \rightarrow 0^+} \sum_{m,n=1}^{\infty} \frac{f_n - f_m}{\omega - \omega_{mn} + i\eta} \varphi_m(\mathbf{r}) \varphi_n^*(\mathbf{r}) \varphi_m^*(\mathbf{r}') \varphi_n(\mathbf{r}'), \quad (2.81)$$

where $\omega_{mn} = \varepsilon_m - \varepsilon_n$ are the excitation energies of the KS states and f_n and f_m are the occupation numbers of the KS orbitals. The double summation ensures that the only terms that contribute are those where one orbital is occupied and the other is not.

Performing a Fourier transformation with respect to position, the linear density response in reciprocal space is obtained. This is useful for systems with periodic boundary conditions. We can see in the following equation that we are going from using the positions vectors \mathbf{r} and \mathbf{r}' to using reciprocal lattice vectors \mathbf{G} and \mathbf{G}' ¹⁰⁷:

$$\chi_{\mathbf{G}\mathbf{G}'}^0(\mathbf{q}, \omega) = \frac{1}{\Omega} \sum_{\mathbf{k}}^{\text{BZ}} \sum_{n,m} \frac{f_{n,\mathbf{k}} - f_{m,\mathbf{k}+\mathbf{q}}}{\omega + \varepsilon_{n,\mathbf{k}} - \varepsilon_{m,\mathbf{k}+\mathbf{q}} + i\eta} \langle \varphi_{n,\mathbf{k}} | e^{-i(\mathbf{q}+\mathbf{G})\cdot\mathbf{r}} | \varphi_{m,\mathbf{k}+\mathbf{q}} \rangle \langle \varphi_{n,\mathbf{k}} | e^{i(\mathbf{q}+\mathbf{G}')\cdot\mathbf{r}'} | \varphi_{m,\mathbf{k}+\mathbf{q}} \rangle, \quad (2.82)$$

where \mathbf{q} is the momentum transferred by the perturbation, $f_{n,\mathbf{k}}$, $\varepsilon_{n,\mathbf{k}}$ and $\varphi_{n,\mathbf{k}}$ are the occupations, eigenvalues and eigenfunctions of the n th band at the \mathbf{k} th k -point in the Brillouin zone (BZ), Ω is the volume of the unit cell and η is the half width at half maximum of the Lorentzian broadening.

Random Phase Approximation

The last term of the linearized effective potential in Eq. 2.80 is the linearized effective potential, which is obtained by functional Taylor expansion

$$v_{xc1}(\mathbf{r}, t) = \int dt' \int d^3\mathbf{r}' \left. \frac{\delta v_{xc}[n](\mathbf{r}, t)}{\delta n(\mathbf{r}', t')} \right|_{n_0(\mathbf{r})} n_1(\mathbf{r}', t'), \quad (2.83)$$

which features the time-dependent xc kernel

$$f_{xc}(\mathbf{r}, t, \mathbf{r}', t') = \left. \frac{\delta v_{xc}[n](\mathbf{r}, t)}{\delta n(\mathbf{r}', t')} \right|_{n_0(\mathbf{r})}, \quad (2.84)$$

that is, in turn, also a functional of the ground-state density. In any application of the linear-response within TDDFT, one must rely on a suitable approximation to the xc kernel which can, for

example, be generated from the approximation given to the time-dependent xc potential. Another example is when all dynamical xc effects are ignored, the simplest treatment of the xc kernel is to set it equal to zero:

$$f_{xc}^{\text{RPA}} = 0, \quad (2.85)$$

which is known as the random phase approximation (RPA).

Interacting density response function

The interacting density response function is recovered by solving the Dyson equation

$$\chi(\mathbf{r}, \mathbf{r}', \omega) = \chi^0(\mathbf{r}, \mathbf{r}', \omega) + \iint_{\Omega} d^3\mathbf{r}_1 d^3\mathbf{r}_2 \chi^0(\mathbf{r}, \mathbf{r}_1, \omega) \left\{ \frac{1}{|\mathbf{r}_1 - \mathbf{r}_2|} + f_{xc}(\mathbf{r}_1, \mathbf{r}_2, \omega) \right\} \chi(\mathbf{r}_2, \mathbf{r}', \omega), \quad (2.86)$$

where all the terms are functionals of the ground-state density and one can approximate the interacting response function in terms of the non interaction response function:

$$\chi_{\mathbf{G}, \mathbf{G}'}(\mathbf{q}, \omega) \approx \frac{\chi_{\mathbf{G}, \mathbf{G}'}^0(\mathbf{q}, \omega)}{1 - v_{\mathbf{G}, \mathbf{G}'}(\mathbf{q}) \chi_{\mathbf{G}, \mathbf{G}'}^0(\mathbf{q}, \omega)}, \quad (2.87)$$

where $v_{\mathbf{G}, \mathbf{G}'}$ is the interaction kernel for the Coulomb interaction in 3D,

$$v_{\mathbf{G}, \mathbf{G}'}(\mathbf{q}) = \frac{4\pi}{\|\mathbf{q} + \mathbf{G}\|^2}, \quad (2.88)$$

and the RPA was used.

2.4.3 Dielectric matrix using LDR-TDDFT-RPA

The inverse of the dielectric function ε^{-1} relates the electric field of a system to an external electric field, $\mathbf{E} = \varepsilon^{-1} \mathbf{E}_{ext}$, and it can be approximated for long wavelengths and small frequencies as

$$\varepsilon^{-1} = \frac{v}{v_{ext}} = 1 + v_H \frac{n_1}{v_{ext}}, \quad (2.89)$$

where v_H is the Hartree potential, .

The dielectric matrix within linear density response TDDFT is related to the the interacting response function by, and n_1 is the linear response of the density to the external perturbation v_1 .

$$\varepsilon_{\mathbf{G}\mathbf{G}'}^{-1}(\mathbf{q}, \omega) = \delta_{\mathbf{G}\mathbf{G}'} + \frac{4\pi}{\|\mathbf{q} + \mathbf{G}\|^2} \chi_{\mathbf{G}\mathbf{G}'}(\mathbf{q}, \omega), \quad (2.90)$$

where n_1 is the linear response of the density to the external perturbation v_1 .

Using the RPA, the dielectric matrix^{108–110} is given in terms of the non-interacting response function by

$$\varepsilon_{\mathbf{G}\mathbf{G}'}^{RPA}(\mathbf{q}, \omega) = \delta_{\mathbf{G}\mathbf{G}'} - \frac{4\pi}{\|\mathbf{q} + \mathbf{G}\|^2} \chi_{\mathbf{G}\mathbf{G}'}^0(\mathbf{q}, \omega). \quad (2.91)$$

In optical spectroscopy, the complex index of refraction \tilde{n} is defined as

$$\tilde{n}^2 = \varepsilon_M(\omega), \quad (2.92)$$

where ε_M is the macroscopic dielectric function. The imaginary part of the macroscopic dielectric function is therefore the photoabsorption of a solid. The macroscopic dielectric function in terms of the microscopic dielectric function follows as

$$\varepsilon_M(\omega) = \frac{1}{\varepsilon^{-1}(\mathbf{q}, \mathbf{G} = 0, \mathbf{G}' = 0, \omega)} = \frac{1}{\varepsilon_{00}^{-1}(\mathbf{q}, \omega)} \quad (2.93)$$

As mentioned before, the optical absorption spectrum is obtained from the imaginary part of the macroscopic dielectric function

$$\text{Absorption} = \text{Im} [\varepsilon_M(\mathbf{q} \rightarrow 0, \omega)], \quad (2.94)$$

where the momentum transfer cannot be zero because the Coulomb kernel (Eq. 2.88) would diverge at $\mathbf{q} = \mathbf{G} = 0$. Instead, we take the limit $\mathbf{q} \rightarrow 0^+$ for $\mathbf{G} = 0$. In this limit, the matrix elements in equation 2.82 for $\mathbf{G} = 0$ reduce to

$$\langle \varphi_{n,\mathbf{k}} | e^{-i(\mathbf{q}+\mathbf{G})\cdot\mathbf{r}} | \varphi_{m,\mathbf{k}+\mathbf{q}} \rangle = -i\mathbf{q} \cdot \frac{\langle \varphi_{n,\mathbf{k}} | \nabla | \varphi_{m,\mathbf{k}+\mathbf{q}} \rangle}{\varepsilon_{n,\mathbf{k}} - \varepsilon_{m,\mathbf{k}}}. \quad (2.95)$$

Neglecting local field effects, that is, the rapid oscillations on the microscopic scale caused by slowly varying external fields, the macroscopic dielectric matrix can be approximated as

$$\varepsilon_M(\omega) \approx \varepsilon_{00}(\omega), \quad (2.96)$$

which is valid for local field effects parallel to \mathbf{q} .

Replacing equations 2.82 and 2.95 in equation 2.91, we can obtain an expression for the imaginary part of the microscopic dielectric function in the optical limit,

$$\Im[\varepsilon_M(\omega)] = \frac{4\pi\eta}{\Omega} \sum_{nm} \frac{f_m - f_n}{(\omega - \varepsilon_n + \varepsilon_m)^2 + \eta^2} \left(\frac{\hat{\mathbf{e}}_{\mathbf{q}} \cdot \langle \varphi_n | \nabla | \varphi_m \rangle}{\varepsilon_n - \varepsilon_m} + \Delta_{xc} \right)^2, \quad (2.97)$$

and the real part,

$$\Re[\varepsilon_M(\omega)] = 1 - \frac{4\pi}{\Omega} \sum_{nm} \frac{(\omega - \varepsilon_n + \varepsilon_m)(f_m - f_n)}{(\omega - \varepsilon_n + \varepsilon_m)^2 + \eta^2} \left(\frac{\hat{\mathbf{e}}_{\mathbf{q}} \cdot \langle \varphi_n | \nabla | \varphi_m \rangle}{\varepsilon_n - \varepsilon_m} + \Delta_{xc} \right)^2, \quad (2.98)$$

where $\hat{\mathbf{e}}_{\mathbf{q}}$ is the unit vector in the direction of \mathbf{q} .

The electron energy loss spectrum is then

$$\text{EELS} = -\text{Im} \left[\frac{1}{\varepsilon_M(\mathbf{q}, \omega)} \right]. \quad (2.99)$$

2.5 Chlorophyll

Chlorophyll (Chl) *a* and *b* are the most common chlorophyll molecules found in green plants. Both have the same basic structure: a magnesium ion (Mg^{2+}) in the center of a chlorin ring, a reduced porphyrin, and phytol chain. They differ by a group attached to one of the carbon atoms of the chlorin ring: a methyl group (CH_3) for Chl *a* and a aldehyde group (HCO) for Chl *b*⁴³ as shown in Figure 2.3.

The chlorin ring is a stable molecule around which electrons are delocalized in π orbitals. This means it can easily lose or gain electrons and has the potential to transfer excited electrons to other molecules. An important property of π -conjugated systems is that they can absorb light in the visible regime and are therefore deeply colored, which is a general characteristic of porphyrins. This is because light in the visible regime has sufficient energy to excite an electron from the highest occupied molecular orbital (HOMO) to the lowest unoccupied molecular orbital (LUMO) of a porphyrin.

Chl molecules strongly absorb light in the red and blue regions of the spectrum. These peaks in the absorption are known as the Q and Soret bands, respectively. This is what gives the green

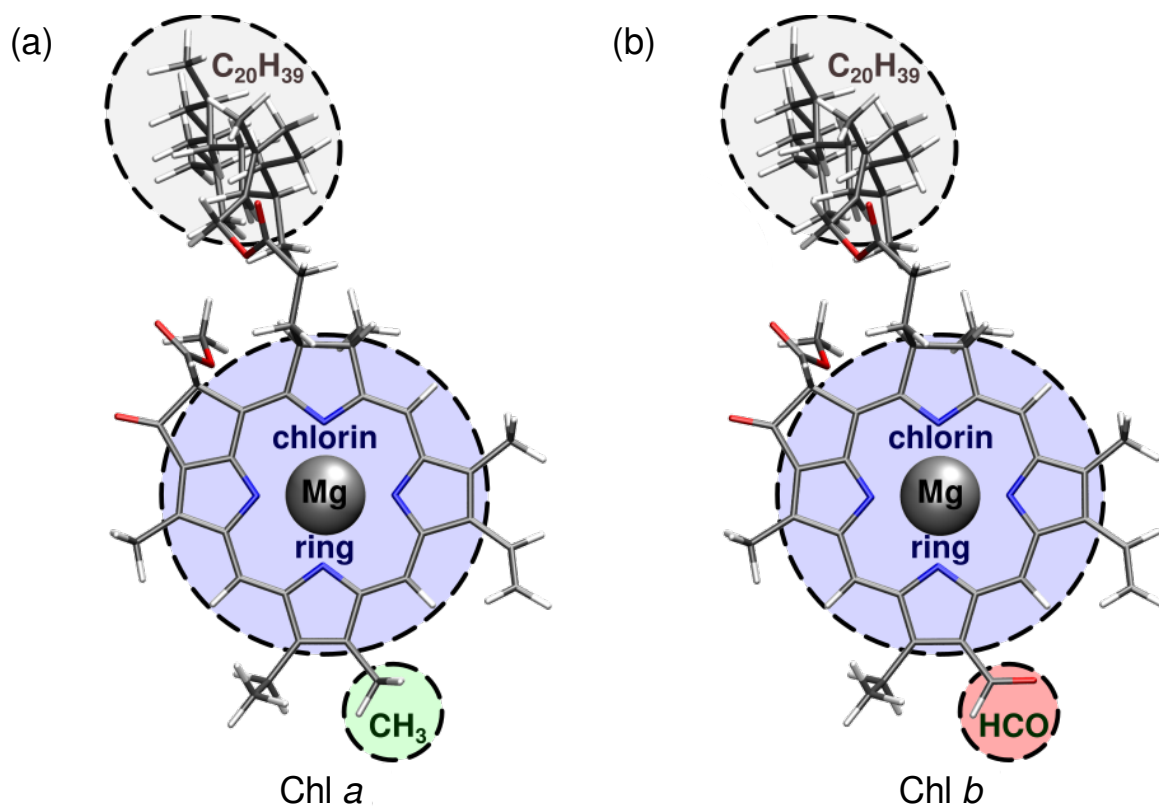


Figure 2.3: Schematics of (a) Chl *a* and (b) Chl *b* with the Mg atom and the chlorin ring (blue), the phytol carbon chain (grey) and either the methyl group (CH₃, green) or the aldehyde group (HCO, red). Mg, C, O, N, and H atoms are depicted in silver, grey, red, blue, and white, respectively.

color to plants and other organisms that contain chlorophyll. When measured in an ether solution, the difference between the Q and Soret band is smaller for Chl *b* compared to Chl *a*, i.e., the Q band is blue-shifted and the Soret band is red-shifted¹¹¹. In this way, Chl *a* and *b* provide experimentally relevant non-periodic systems for benchmarking our LCAO-TDDFT- k - ω code.

2.6 Single-Walled Carbon Nanotubes

A single-walled carbon nanotube (SWCNT) is a graphene sheet rolled into a cylinder with axial symmetry. SWCNTs have typical diameters of about 0.7 to 10.0 nm, with the majority having diameters less than 2 nm¹¹², and lengths from 1 μm to 1 cm¹¹². For this reason they are considered to be one-dimensional objects, because their length to diameter ratio is often as large as 10^4 to 10^5 .

How the graphene sheet is rolled up, that is, the orientation of the carbon atoms' hexagon within the lattice relative to the axis of the nanotube, determines the properties of the tube. SWCNTs are either achiral (zigzag and armchair) or chiral. The chiral vector \mathbf{C}_h points along the circumference of the nanotube, is normal to the translational vector \mathbf{T} , and is expressed in terms of graphene's unit vectors \mathbf{a}_1 and \mathbf{a}_2 by

$$\mathbf{C}_h = n\mathbf{a}_1 + m\mathbf{a}_2 \equiv (n, m) \quad (0 < m < n), \quad (2.100)$$

where n and m are integers that determine the chiral angle $\theta = \arctan \left[\sqrt{3}(n/(2m+n)) \right]$. From this it follows that $(n = m, \theta = 30^\circ)$ corresponds to armchair type SWCNTs, $(m = 0, \theta = 0^\circ)$ to zigzag, and other combinations $(0^\circ < \theta < 30^\circ)$ to chiral nanotubes as it is shown in Figure 2.4.

The carbon atom periodicity also has a huge impact on the band structure and electronic properties of the SWCNTs. This dependence is derived from the tight binding model of graphene and is known as the zone-folding approximation. For our purposes we need only consider the classification of SWCNTs that is given by the relation of their indices: a SWCNT is metallic if $n - m \equiv 0 \pmod{3}$, which includes all armchair type SWCNTs, and semiconducting otherwise. When taking into account curvature effects, the classification changes: armchair SWCNTs remain metallic but when the indices $n - m \equiv 0 \pmod{3}$, the nanotube has a finite gap proportional to $1/d^2$ and $\sin 3\theta$ where d is the diameter and θ the chiral angle¹¹³.

The differences between metallic and semiconducting SWCNTs can be pictured with their density of states (DOS). The DOS near the Fermi level is non-zero for metallic nanotubes, whereas the DOS near the Fermi level is zero for semiconducting nanotubes as shown in Figure 2.5. In either case, the DOS is not a smooth function of the energy, but instead has sharp peaks known as van Hove singularities. This feature of the DOS results from the low dimensionality, 1D,

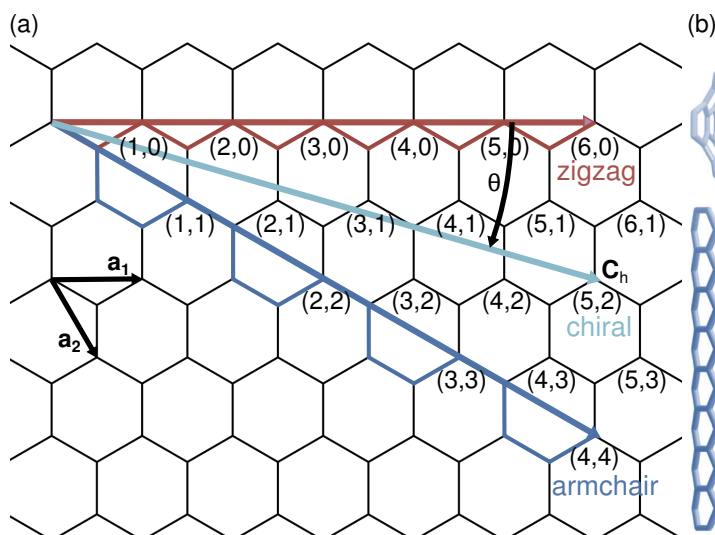


Figure 2.4: (a) Graphene sheet showing the \mathbf{C}_h vector for zigzag $(n, 0)$ (blue), armchair (n, n) (red), or chiral (n, m) nanotubes and (b) the appearance of armchair (blue), zigzag (red) and chiral nanotubes.

of SWCNTs. Each singularity is marked with the index of the subband to which it belongs in Figure 2.5.

Optical selection rules for SWCNTs allow light polarized parallel to the nanotube axis to produce intense transitions between the corresponding subbands in the valence and conduction bands. For instance, $v_1 \rightarrow c_1$ and $v_2 \rightarrow c_2$, and so on, correspond to well-defined absorptions with energies E_{11} and E_{22} , as depicted schematically in Figure 2.5. Metallic SWCNTs also have intense absorption peaks associated to transitions between van Hove singularities¹¹⁴. Recently, experimental measurements of chirality sorted SWCNTs have provided both optical absorbance¹¹⁵ and electron energy loss (EELS) spectra⁴⁸ of a plethora of SWCNTs. For this reason, SWCNTs provide experimentally relevant 1D periodic systems for benchmarking our LCAO-TDDFT- k - ω code.

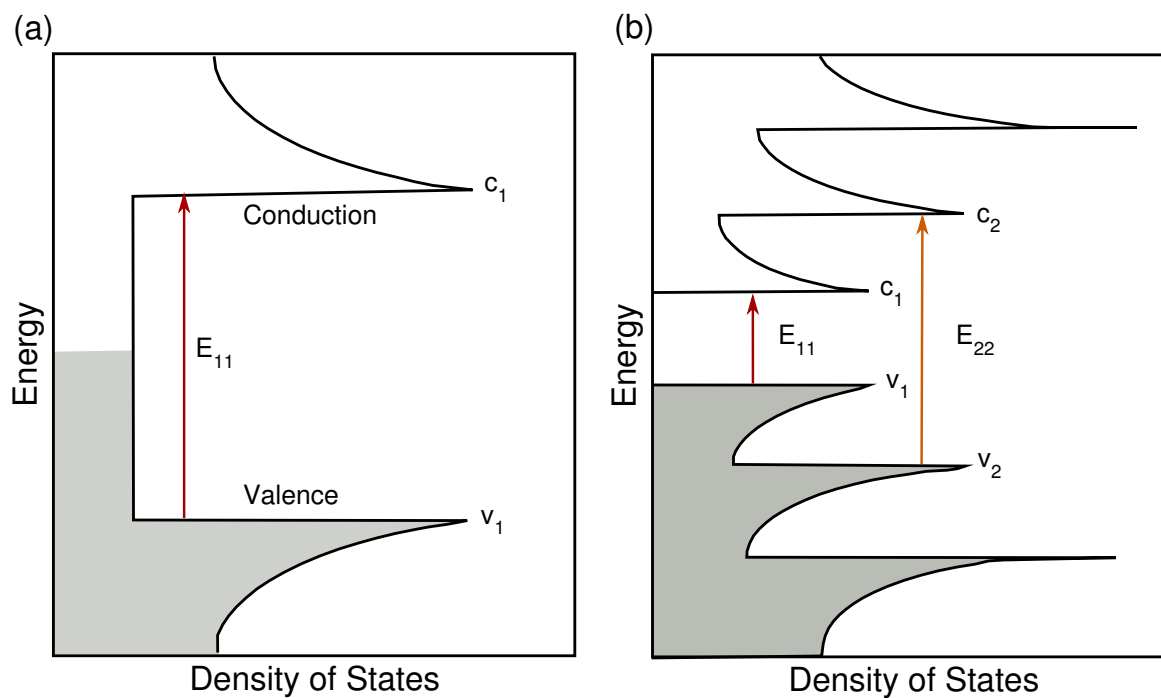


Figure 2.5: Schematics of the density of states (DOS) of (a) a metallic SWCNT and (b) a semiconducting SWCNT. The sharp peaks are van Hove singularities and the arrows show the dominant E_{11} and E_{22} transitions.

Chapter 3

Methodology

3.1 Chlorophyll Monomers Structures & Computational details

As discussed in Ref. 52, Chl molecules in nature are found inside protein pockets that modulate their color. In order to assess how strong this modulation is, the absorption spectra of bare Chl molecules, without solvents or external perturbations, is needed. This is also the starting point to understand the absorption properties of photosystems that contain hundreds of Chl molecules within a protein microenvironment. These were the motivations for Milne *et al.*⁵² to take a new approach in which they tagged the Chl molecules with molecular cations to avoid the rapid decomposition of the Chl molecules when they were evaporated for gas-phase spectroscopy. The charge tags used are quaternary ammonium cations which do not possess mobile protons. Hence the charge remains located in the tag and the Chl spectra should not contain shifts that are hard to interpret. Tetramethylammonium, **1**⁺, tetrabutylammonium, **2**⁺, and acetylcholine, **3**⁺, were the charge tags Milne *et al.* used in Ref. 52.

In this thesis, we performed calculations only for the **1**⁺ tag because Milne *et al.* showed that the dependence on the nature of the charge tag was negligible⁵². Also, the large phytol or hydrocarbon chain was cut for some of the calculations going from C₂₀H₃₉ to C₅H₉. This

simplified version of the molecules allowed us to perform the DFT calculations using a smaller unit cell, 2417.43 Å³ for Chl *a* and 2610.02 for Å³ Chl *b*. The structures used for these calculations are depicted in Figure 3.1.

The DFT calculations were performed using the PAW implementation of the GPAW code. We used the Perdew-Burke-Ernzerhof (PBE)⁷⁴ exchange and correlation functional, which is a generalized gradient approximation. To represent the electron density and the KS wavefunctions we used linear combinations of atomic orbitals with functions from single- ζ (SZ) up to quadruple- ζ (QZ) and their polarized versions (SZP and QZP, for example). We also used PW representations with a cutoff of 340 eV, which has been shown to converge carbon dimers as reported on the GPAW website¹¹⁷. We did not show the convergence of the total energy of the structures with respect to the PW cutoff. We rather studied the convergence of the optical absorption spectra by comparison with PW, various basis sets for the LCAO mode, and the experimental results. We did this because the spectra depend on both occupied and unoccupied eigenenergies and the convergence of the total energy would not imply a converged spectrum.

The structures were optimized until a maximum force less than 0.03 eV/Å was obtained in a supercell with more than 6 Å of vacuum. For the charged structures, fixed boundary conditions were used rather than periodic boundary conditions, i.e., the density and wavefunctions at the boundaries of the unit cell were set to zero. This has been previously shown to be necessary to model charged structures in gas phase¹¹⁸. We did not perform calculations at the spin-polarized level because the number of electrons was even for the charged structures.

The optical absorbance was modelled using the imaginary part of the dielectric function, $\Im[\varepsilon(\omega)]$, from LCAO-TDDFT- k - ω calculations. From Eq. 2.97 and adding the derivative discontinuity correction of the exchange part of the GLLB-SC functional to the eigenenergies of unoccupied KS states, the dielectric function is

$$\Im[\varepsilon_M(\omega)] = \frac{4\pi\eta}{\Omega} \sum_{nm} \frac{f_m - f_n}{(\omega - \varepsilon_n + \varepsilon_m - \Delta_x^{\text{GLLB-SC}})^2 + \eta^2} \left(\frac{\hat{\mathbf{e}}_{\mathbf{q}} \cdot \langle \varphi_n | \nabla | \varphi_m \rangle}{\varepsilon_n - \varepsilon_m + \Delta_x^{\text{GLLB-SC}}} \right)^2. \quad (3.1)$$

From this we can expect the spectra to be blue shifted by the energy derivative discontinuity correction and the intensities corresponding to lower energies will decrease.

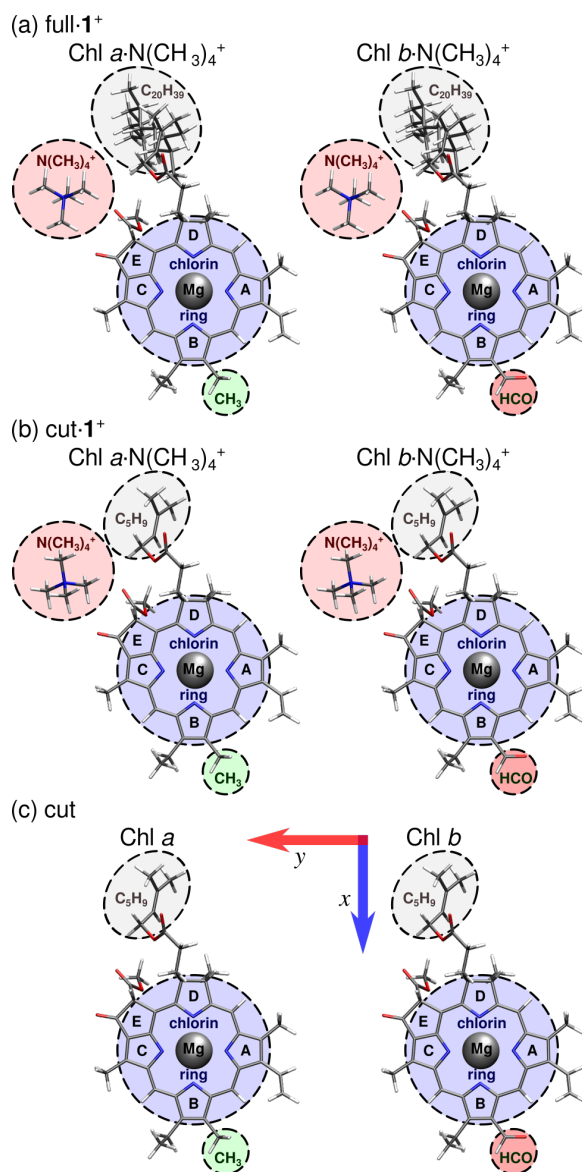


Figure 3.1: Schematics of (a) full·1⁺, (b) cut·1⁺, and (c) cut chlorophyll *a* (Chl *a*) and chlorophyll *b* (Chl *b*). The full (C₂₀H₃₉) or cut (C₅H₉) hydrocarbon chain are in grey and the tetramethylammonium charge tag (N(CH₃)₄⁺) in red. Labelling of the rings (A–E) and orientation of the *x* and *y* polarization axes (blue and red arrows) are according to IUPAC-IUB nomenclature^{43,116}. Structures in (a) full·1⁺ are based on those provided in Ref. 52.

The matrix elements in Eq. 3.1 are expressed using the PAW formalism as in Eq. 2.64 and they must already be calculated to obtain the forces in the previous DFT calculations. For this reason, obtaining the imaginary part of the dielectric function, $\Im[\varepsilon(\omega)]$, within the LCAO-TDDFT- \mathbf{k} - ω code simply involves the multiplication of matrices that have been already calculated. This is a very efficient method with a scaling better than $O(NM^2)$ where N is the number of KS wavefunctions and $M \geq N$ is the total number of basis functions used in the LCAO calculation.

The spectra were calculated with an electronic broadening of $\eta = 50$ meV to the individual Lorentzian peaks. The electron and hole density difference, $\Delta\rho(\mathbf{r})$, of the first four excitations, $m \rightarrow n$, were calculated using the transitions from LCAO-TDDFT- \mathbf{k} - ω , with

$$\Delta\rho(\mathbf{r}) = \rho_h(\mathbf{r}) + \rho_e(\mathbf{r}) \approx |\varphi_m(\mathbf{r})|^2 - |\varphi_n(\mathbf{r})|^2, \quad (3.2)$$

where φ_m and φ_n are the KS orbitals corresponding to the hole and electron, respectively⁴⁷.

3.2 Single-Walled Carbon Nanotubes Structures & Computational Details

In Figure 3.2 we show the indices (m, n) of the SWCNTs in a graphene sheet used in our calculations. The ones marked with red are semiconducting nanotubes for which we obtained the theoretical absorption spectra, the blue ones are semiconducting with electron energy loss spectroscopy, the mauve ones have both optical absorption and electron energy loss spectroscopy, and the dark blue ones are metallic nanotubes with electron energy loss spectroscopy.

The density functional theory (DFT) calculations were also performed using the GPAW code, based on the projector-augmented wave (PAW) method within the atomic simulation environment (ASE)¹²⁰. We have used for the SWCNTs a revised Perdew-Burke-Ernzerhof generalized gradient approximation for solids (PBEsol)⁷⁷ for the exchange and correlation (xc) functional, and represented the Kohn-Sham wave functions using a linear combination of atomic orbitals (LCAO)⁹¹ with a double- ζ polarized (DZP) basis set.

Both the unit cell and atomic structure for each of the nineteen SWCNTs studied (see Fig. 3.2) were relaxed until the maximum force was less than 0.05 eV/Å by including 10 Å of vacuum

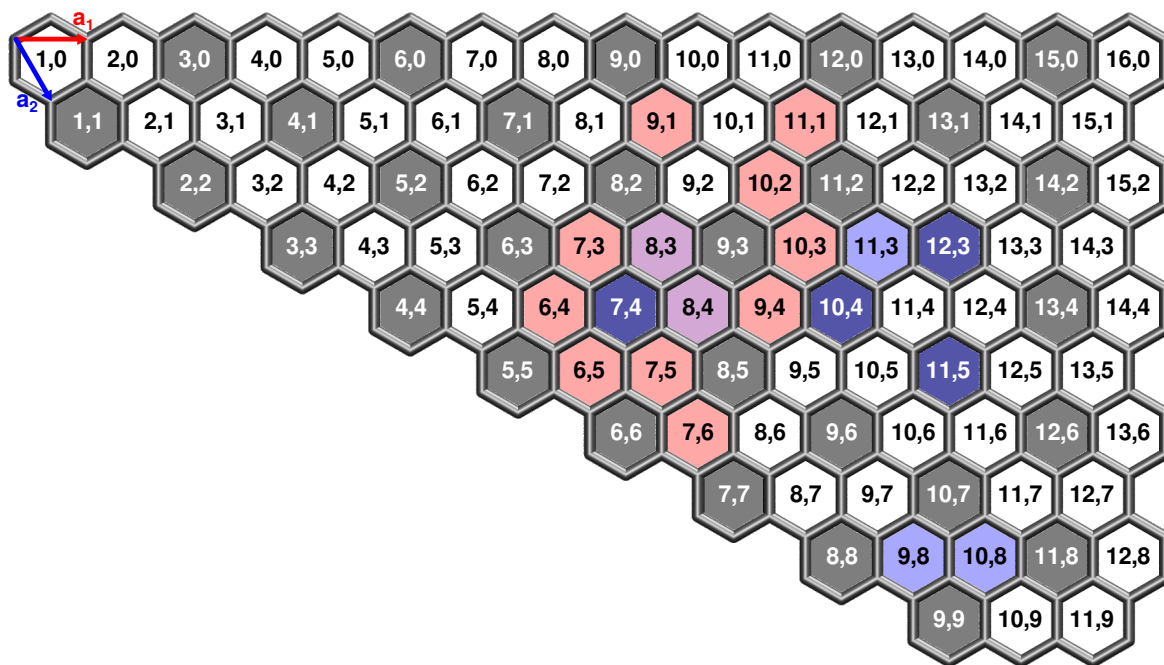


Figure 3.2: SWCNT indices (m, n) of circumference vector $\mathbf{C} \equiv m\mathbf{a}_1 + n\mathbf{a}_2$ where \mathbf{a}_1 (red) and \mathbf{a}_2 (blue) are the primitive unit vectors with optical absorbance (red), electron energy loss (blue), and both (mauve) data from Refs. 115 and 48, respectively. Metallic tubes $(m - n \equiv 0 \pmod{3})$ are marked in grey or dark blue. Adapted from Ref. 119.

perpendicular to the SWCNT's axis. Periodic boundary conditions were employed only in the direction of the SWCNT axis. A grid spacing of $h \approx 0.2 \text{ \AA}$ was employed and the Brillouin-zone was sampled with a k -point density of $\Delta k \lesssim \frac{1}{30} \text{ \AA}^{-1}$.

A Harris calculation was performed for each SWCNT to increase the k -point density to $\Delta k \lesssim \frac{1}{1200} \text{ nm}^{-1}$, fixing the electron density throughout the self-consistency cycle. Such a dense k -point density was found to be necessary to converge the calculated absorbance spectra. In order to improve the description of the electronic gap, we employed the correction of the derivative discontinuity of the exchange and correlation (xc) functional GLLB-SC as described in Section 2.1.9. We also corrected the optical absorption spectra given by the imaginary part of the dielectric function following Eq. 3.1, as well as the real to calculate the electron energy loss spectra in a

similar manner. The exciton density was calculated as in Section 3.1, where the electron hole density difference, $\Delta\rho(\mathbf{r})$, was calculated as⁴⁷

$$\Delta\rho(\mathbf{r}, \omega) = \rho_h(\mathbf{r}, \omega) + \rho_e(\mathbf{r}, \omega) \approx \sum_{nm} \frac{\eta^2 |f_{nm}|^2 (|\varphi_n(\mathbf{r})|^2 - |\varphi_m(\mathbf{r})|^2)}{(\omega - \varepsilon_n + \varepsilon_m + \Delta_x^{\text{GLLB-SC}})^2 + \eta^2}, \quad (3.3)$$

where f_{nm} are the calculated intensities of the $m \rightarrow n$ transition from Eq. 2.97, and $\int \Delta\rho(\mathbf{r}, \omega) d^3\mathbf{r} = 0$.

3.3 Combined System Structure & Computational Details

In Figure 3.3 we show schematics of the combined system, Chl *a*/(6,4) CNT. The unit cell of this system contains the neutral *cut* structure of Chl *a* with the *y* direction (along the N–Mg–N atomic bonds, see Fig. 2.3) aligned with the (6,4) CNT axis, the *z* axis. That is, we rotated the Chl *a* molecules to be aligned with the nanotube as shown in Fig. 3.3(c). We used the relaxed structures from the previous sections to build the combined system. The distance between the Mg atom of the chlorophyll molecule and the nearest C atom from the carbon nanotube is 2.5 Å after relaxation.

The computational details of the calculations of the combined system are the same as the SWCNTs unless otherwise stated. The system was relaxed using FIRE¹²¹ until the maximum force was less than 0.05 eV/Å by having vacuum in the *x* and *y* directions of 10 and 12 Å, respectively, in order to avoid interactions with the replicas. The length of the supercell in the *z* direction was that of the carbon nanotube, that is 18.3 Å. Periodic boundary conditions were used in all three directions. A 112×144×96 grid representation was employed and the Brillouin-zone was sampled using 1×1×3 *k*-points.

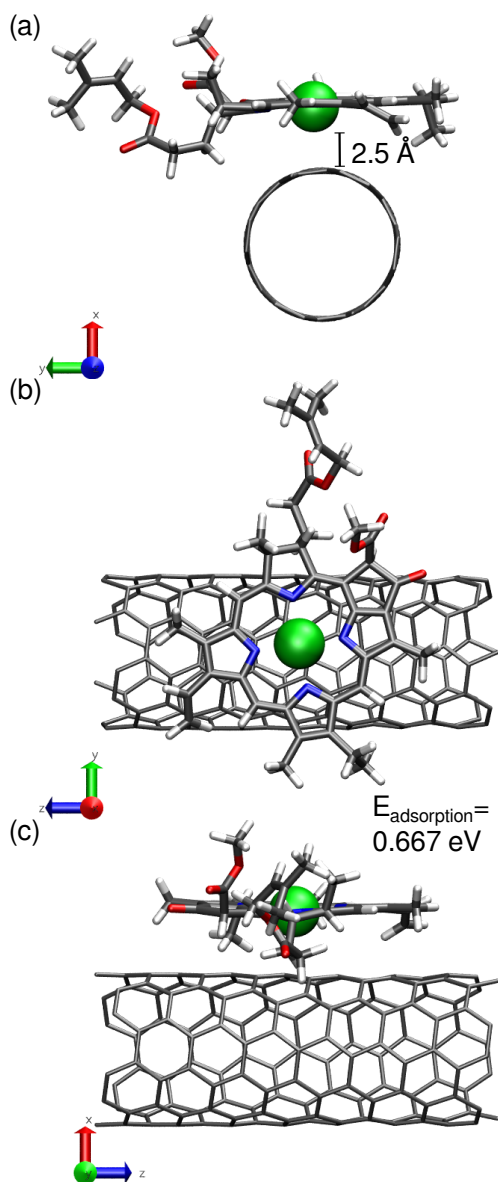


Figure 3.3: Schematics of the system of a cut chain chlorophyll *a* molecule and a (6,4) carbon nanotube. Here are depicted the views along (a) the *z* axis, (b) the *y* axis, and (c) the *x* axis. Mg, C, O, N, and H atoms are depicted in green, black, red, blue, and white, respectively. In (a) the separation between the Chl and SWCNT is approximately 2.5 Å. The calculated binding energy of Chl *a* on the (6,4) SWCNT is 0.667 eV.

Chapter 4

Results & Discussion

The Results & Discussion chapter is split into three sections: the first section shows the optical absorption spectra and related properties of the chlorophyll *a* and *b* monomers, the second section corresponds to the optical absorbance and electron energy loss spectroscopy of single-walled carbon nanotubes (SWCNTs) and the last section corresponds to the study of the combined system, chlorophyll (Chl) *a*/(6,4) CNT.

4.1 Chlorophyll *a* and *b* Monomers *

4.1.1 Optical Absorption Spectra

In Figure 4.1, we show the optical absorption spectrum of the neutral *cut* structure of Chl *a* calculated using either multiple- ζ basis sets (SZ, DZ, TZ and QZ) or the polarized versions of the basis sets (SZP, DZP, TZP and QZP) within the linear combination of atomic orbitals (LCAO) mode of the `CP2K` code. We systematically increase the number of functions to assess the sensitivity of the optical absorbance and observe that the spectrum converges differently for

*This work was performed in collaboration with Duncan John Mowbray, Ask Hjorth Larsen, Keenan Lyon and Bruce Forbes Milne, and is adapted from “Optical Excitations of Chlorophyll *a* and Chlorophyll *b* Monomers and Dimers”, *in preparation*, **2019**.¹²²

basis sets with and without polarization functions.

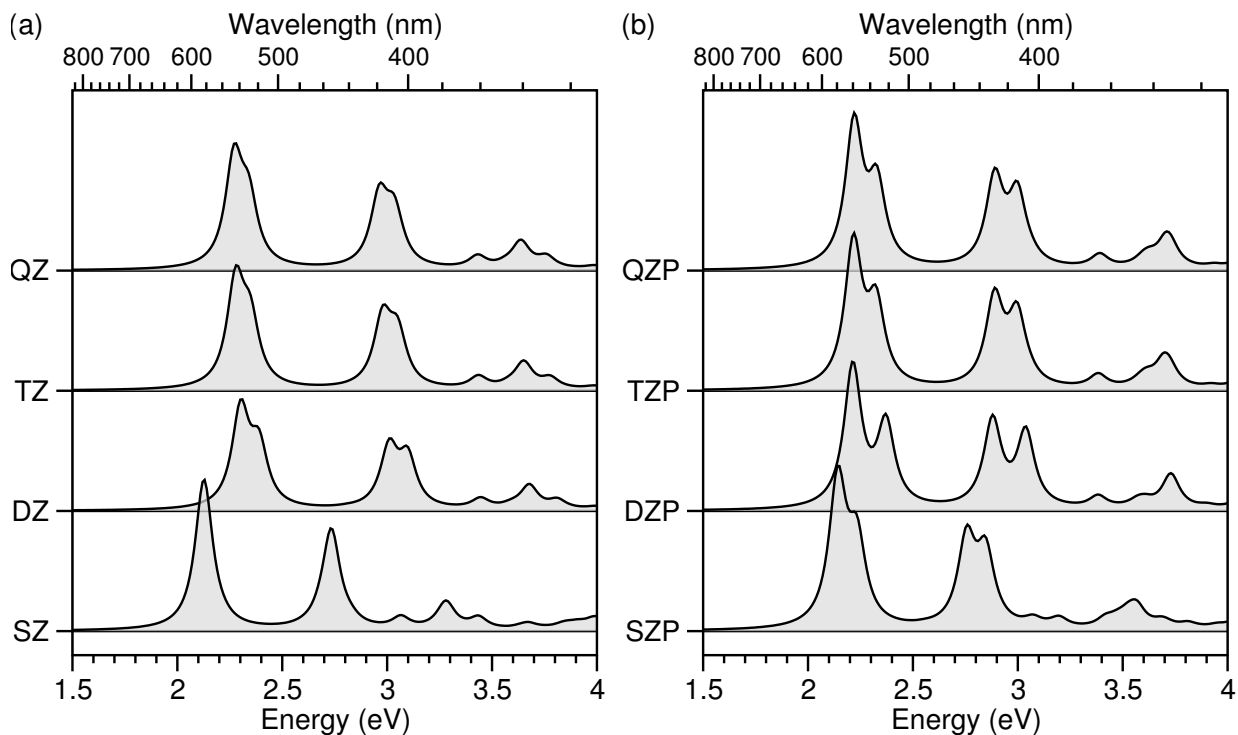


Figure 4.1: Dependence of the optical absorption spectra of Chl *a* on the single- ζ (SZ), double- ζ (DZ), triple- ζ (TZ) and quadruple- ζ (QZ) LCAO basis sets (a) with and (b) without polarization (P) functions.

It can be observed in Figure 4.1(a) that the SZ basis set yields a red-shifted spectrum compared to the other spectra, the TZ and QZ basis sets spectra are almost the same, and the DZ basis set yields the same energies of the Q and Soret bands compared to those of the TZ and QZ but the peaks within the band are more separated than in the TZ or QZ spectra. The polarized multiple-zeta basis sets are shown in Figure 4.1(b) and we observe that the SZP basis set also yields a red-shifted spectrum compared to other spectra and there are more peaks above 3 eV. The spectra obtained using TZP and QZP are basically the same and the DZP basis set yields the same energy of the Q and the Soret bands although the peaks within the bands are a little bit separated when compared to TZP and QZP.

Even though it seems that the spectrum of Chl *a* will not change if we increase the number of functions of the basis set, we cannot rely solely on these results to claim that an LCAO basis set will guarantee an accurate description of the optical absorption spectra. This is because LCAO basis sets cannot be systematically converged to the complete basis set limit. This is clear from comparing the result of the inclusion of polarization functions with the LCAO basis sets in Figure 4.1. Although double- ζ basis sets are converged with respect to the number of radial functions, the inclusion of polarization systematically alters the spectra. For this reason, we compare the spectra of Chl *a* and Chl *b* obtained using LCAOs to the spectra yielded by density functional theory (DFT) calculations with a plane wave plane wave (PW) representation of the Kohn-Sham (KS) wavefunctions.

In Figure 4.2, we show the optical absorption spectra of the *cut* structures of both Chl *a* and Chl *b* calculated using either the DZP basis set within the LCAO mode, or using a PW representation of the KS wavefunctions that ensures converged optical absorption spectra. We find that the DZP basis set yields an optical absorption spectrum with transition energies very close to those of the spectrum calculated using PW. We observe that the LCAO spectra is only slightly (much smaller than the 0.1 eV DFT accuracy) red-shifted compared to the PW spectra but underestimates the intensities of the transitions. Nevertheless, we can affirm that the atomic basis set with double- ζ and polarization functions, DZP, is sufficient to ensure semi-quantitative agreement of the optical absorption spectra for the Chl *a* and Chl *b* with the PW calculations.

The DZP basis sets have been shown to be sufficient (and often necessary) to converge to the results calculated with plane waves representation of the KS wavefunctions in other works as well^{91,123}. From hereon we shall restrict consideration to the DZP basis set and simply refer to our calculations as LCAO.

Figure 4.3 shows the optical absorption spectra, obtained with the LCAO-TDDFT- k - ω code and with the derivative discontinuity correction of the Gritsenko-Leeuwen-Lenthe-Baerends solid and correlation (GLLB-SC) functional for the *cut*, *cut* $\cdot\mathbf{1}^+$ and *full* $\cdot\mathbf{1}^+$ structures of Chl *a* and Chl *b* molecules, as depicted in the schematics of Figure 2.3. For comparison, the experimental data from reference 52 corresponding to the full chain Chl molecules with either a $\mathbf{1}^+$ or a $\mathbf{3}^+$ tag are also shown. We have assigned the first and the second excitations of the calculated spectra to the

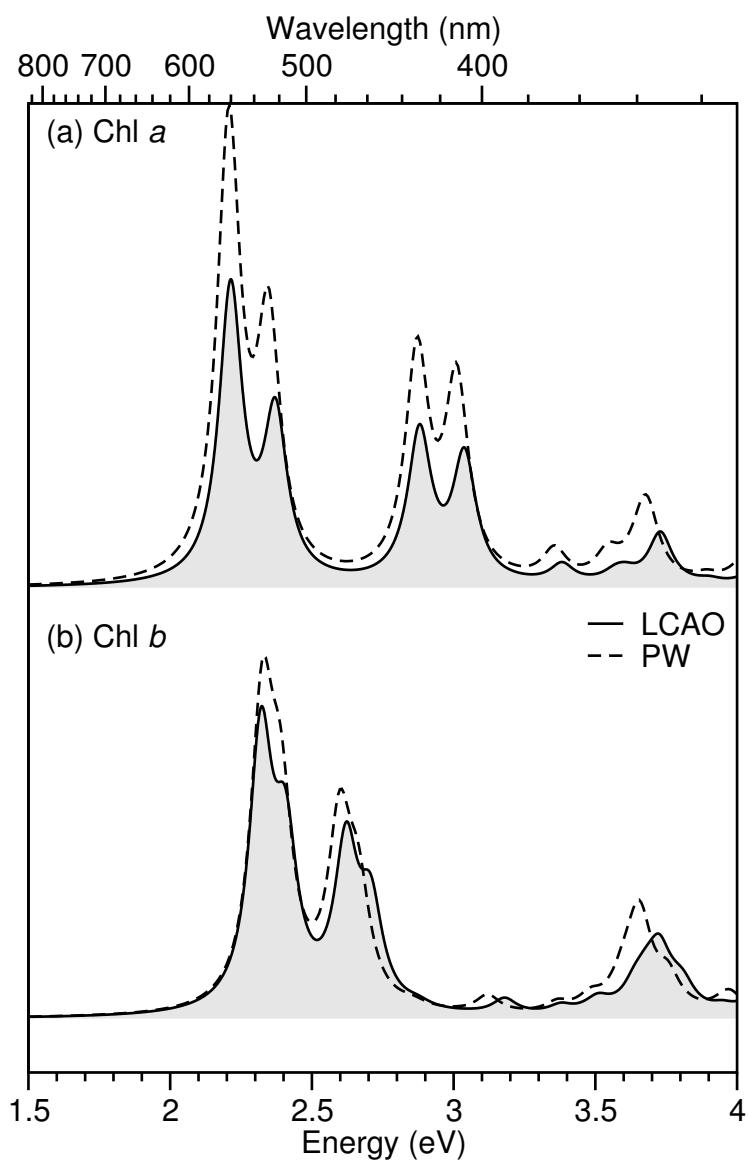


Figure 4.2: Optical absorption of Chl *a* and *b* employing LCAO (solid lines) and PW (dashed lines) representations of the Kohn-Sham orbitals.

Q band and the third and fourth excitations to the Soret band.

In the case of Chl *a*, as observed in the Fig. 4.3(a), the onset of the calculated spectra for the

full· $\mathbf{1}^+$ structure are in semi-quantitative agreement with the experimental spectra obtained with either the $\mathbf{1}^+$ or $\mathbf{3}^+$ tag. The difference between the maximum of the Q band and the calculated first excitation energy is less than 0.2 eV and the difference between the maximum of the Soret band and the calculated fourth excitation is less than 0.1 eV. Also, the spectra of the *cut*· $\mathbf{1}^+$ structure shows the same qualitative behavior as the *full*· $\mathbf{1}^+$ structure, suggesting that none to negligible changes in the optical absorption spectra are caused by the carbon chain. However, when the charge tag is removed, that is, regarding the *cut* structure, the Q band peaks are blue shifted and the band gap is widen, whereas the Soret band peaks are red shifted.

For Chl *b*, Figure 4.3(b), the calculated spectra for the *full*· $\mathbf{1}^+$ structure is also in semi-quantitative agreement with the experimental spectra. Specifically, the peaks of the Q band and the Soret band of the *full*· $\mathbf{1}^+$ structure are blue and red shifted, respectively, when compared to the experimental data, with a difference between the Q band maximum and the calculated first excitation of 0.23 eV and a difference between the Soret band maximum and the calculated fourth excitation of 0.26 eV. Again, the spectrum of the *cut*· $\mathbf{1}^+$ structure is qualitatively the same as the spectrum of the *full*· $\mathbf{1}^+$, reinforcing the idea that the carbon chain has no impact in the optical absorbance and that it should be centered on the Mg atom and the chlorin ring. When removing the charge tag, *cut* structure, the Q band peaks are again blue shifted, and the band gap is widen, whereas the Soret band peaks are red shifted.

The intensities of the excitations of the Soret band are being underestimated about 75% for Chl *a* and 52% for Chl *b*, comparing the *full*· $\mathbf{1}^+$ to the experimental data. Also, the intensity of the Soret band peaks is less compared to that of the Q band peaks. This is not the case of the experimental data. Although, the relative intensities are adjusted, that is, the Soret band peaks intensities are increased by the applying the GLLB-SC correction to the spectra following Eq. 3.1, they are still underestimated. Such a difference can be explained by the fact that we are neglecting charge transfer excitations at the linear density response level. The higher intensity of these peaks is often attributed in the literature to this type of charge transfer excitation⁵² which we are unable to model. In this way, our underestimation of the Soret band intensity provides indirect insight into the nature of the experimentally observed peaks.

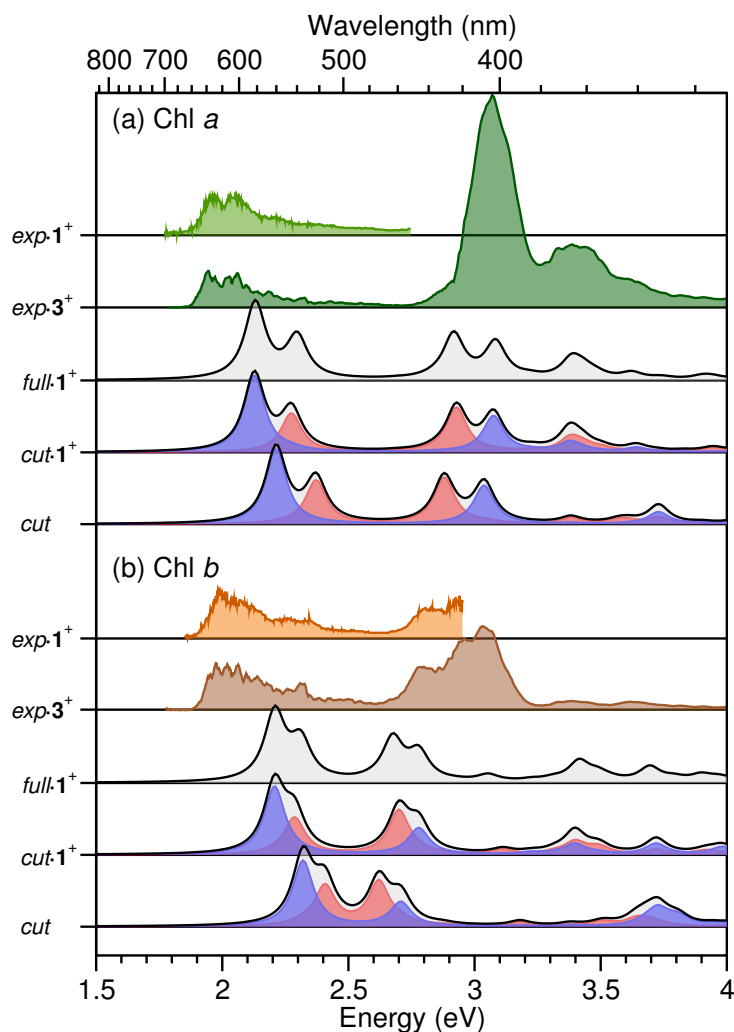


Figure 4.3: Optical absorption spectra, for isolated chlorophyll *a* and *b*, were obtained using the imaginary part of the dielectric function from the frequency domain TDDFT. Linear combinations of atomic orbitals representations of the KS wavefunctions were used for (a) chlorophyll *a* and (b) chlorophyll *b*. Different structures are being compared: chlorophyll with a full hydrocarbon chain and a $\text{N}(\text{CH}_3)_4^+$ charge tag ($\text{full}\cdot\mathbf{1}^+$), with a cut version of the hydrocarbon chain and a $(\text{CH}_3)_4^+$ charge tag ($\text{cut}\cdot\mathbf{1}^+$), and neutral chlorophyll with a cut hydrocarbon chain (cut). The spectra for the cut hydrocarbon chain was decomposed along the N-Mg-N bonds either in the x (blue) or y (red) directions.

Regarding the decomposed spectra of the $cut\cdot\mathbf{1}^+$ and cut structures of Chl a and Chl b , the first and fourth peaks correspond to excitations parallel to the hydrocarbon chain (x direction, blue arrow in Figure 3.1), while the second and third peaks correspond to excitations perpendicular to the hydrocarbon chain (y direction, red arrow in Figure 3.1). In all cases the Q/Soret band for Chl a is lower/higher in energy than the Q/Soret band for Chl b , as found experimentally.

We have compared the calculated spectra for bare Chl a and Chl b molecules to those obtained experimentally. We obtained a reasonable agreement regarding the energies of the excitations, whereas the relative intensities differ due to our neglect of charge-transfer excitations without linear density response. Having been able to reproduce in part the experimental results, we will now study how these excitations are spatially distributed throughout the molecules.

4.1.2 Excitonic Density

In Figure 4.4 we have plotted the spatial distribution of the electron and hole densities for the first four transitions of the $cut\cdot\mathbf{1}^+$ structures of Chl a and Chl b . The first and fourth excitations are induced by optical absorption in the x polarization direction, whereas the second and third excitations are induced by optical absorption in the y polarization direction, as shown in Figure 4.3. In all cases, the excitations are $\pi \rightarrow \pi$ transitions, involving the highest occupied molecular orbital (HOMO) and the lowest unoccupied molecular orbital (LUMO) as well as the HOMO-1 and LUMO+1.

The electron density of the first and third excitations has weight on the $2p_z$ orbitals of the N atoms neighboring the central Mg atom, parallel to the direction of the absorption. In contrast, the hole density of the second and fourth excitations has weight on the $2p_z$ levels of the N and also the Mg atoms. Overall, the first and third excitations redistribute the charge within the chlorin ring, with charge from the ring moving either to the edges or towards the Mg atom. This is in contrast to the second and fourth excitations, which tend to move charge from the Mg atom to the edge of the chlorin ring along the direction of the excitation.

The excitations for Chl a and Chl b are qualitatively the same, but there are differences in the region of the methyl or the aldehyde group. In particular, the electron density of the third and

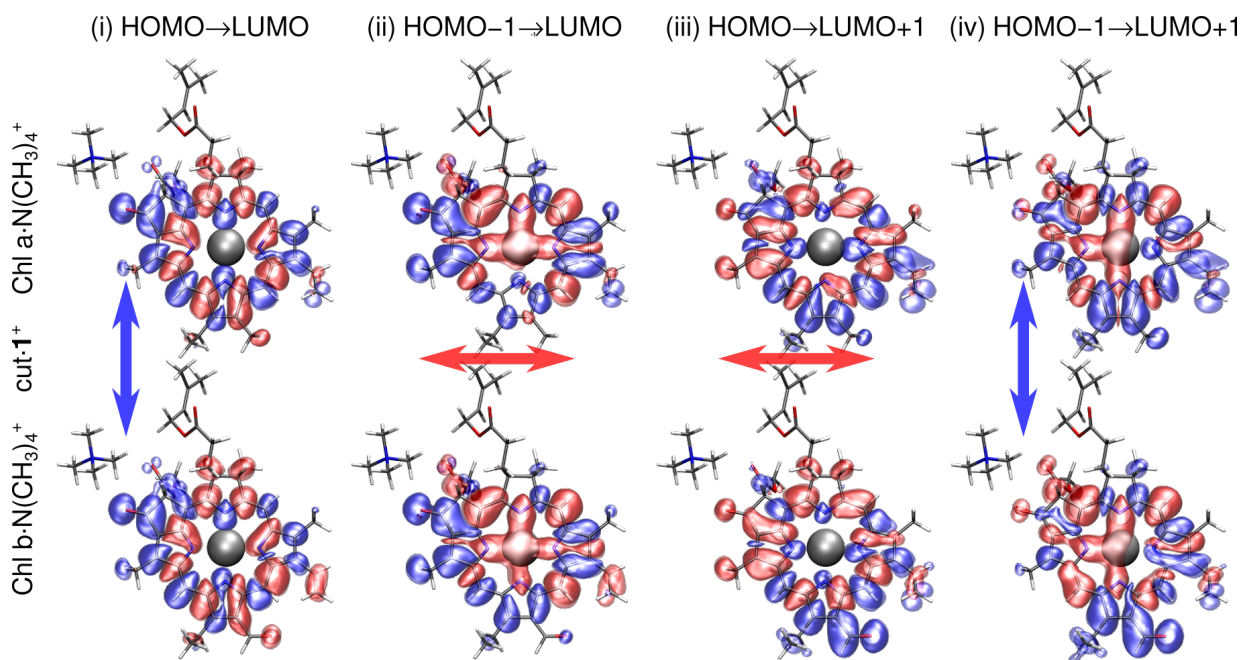


Figure 4.4: Isosurfaces of the electron (blue) and hole (red) densities $\rho(\mathbf{r}) = \pm 0.001 e/\text{\AA}^3$ of the first four excitations of charge tagged Chl $a \cdot \text{N}(\text{CH}_3)_4^+$ and Chl $b \cdot \text{N}(\text{CH}_3)_4^+$ with a cut hydrocarbon chain ($\text{cut} \cdot \mathbf{1}^+$) (i) HOMO \rightarrow LUMO, (ii) HOMO-1 \rightarrow LUMO, (iii) HOMO \rightarrow LUMO+1, and (iv) HOMO-1 \rightarrow LUMO+1. Mg, C, O, N, and H atoms are depicted in silver, grey, red, blue, and white.

fourth transitions has more weight around the aldehyde group of the Chl b than in the methyl group of Chl a . Also, the hole density of the second and the fourth transitions has weight on all the N atoms of the chlorin ring of Chl b , but only on three N atoms of Chl a . Moreover, the electron density has some weight on the remaining N atom which is perpendicular to the direction of excitation.

Finally, it is observed that no charge is coming from or going to the charge tag $\mathbf{1}^+$. Also the excitations of the $\text{cut} \cdot \mathbf{1}^+$ and of the cut structures, which are shown in Figures A.1 and A.2 of Appendix A, have basically the same spatial distribution as the $\text{cut} \cdot \mathbf{1}^+$ structures. This provides additional evidence that justifies the use of charge tagged Chl a and Chl b molecules to describe

experimentally the optical absorption of neutral isolated Chl species.

In this section we have tested the LCAO-TDDFT- k - ω code for isolated molecules obtaining a good description of the optical absorption spectra that both qualitatively and semi-quantitatively matches the experimental data. We will now assess the description of low dimensionality systems using the same code. In the next section we will show the optical absorption spectra and the energy band gap of single-walled carbon nanotubes (SWCNTs) using the LCAO-TDDFT- k - ω code.

4.2 Single-Walled Carbon Nanotubes*

We have looked at very different single-walled carbon nanotubes (SWCNTs) that once relaxed have diameters ranging from 6.97 to 12.38 Å, lengths from 6.51 to 63.02 Å, and from 84 to 868 atoms per unit cell, as listed in Table 4.1. The SWCNTs for which we made calculations have also different electronic properties, 14 of them are semiconducting and four are metallic.

Also in Table 4.1, we show the derivative discontinuity correction of the exchange part of the GLLB-SC functional, Δ_x , that was calculated as explained in Reference 80 and in Section 2.1.9. The corrections have a size on average of $\sim 28\%$ of the corrected band gap energies and are proportional to both the corrected band gap energy and the KS band gap.

4.2.1 Optical Absorption Spectra

In Figure 4.5, we directly compare our results to the experimental data obtained in Ref. 115. The experimental data was normalized, that is, the highest value was set to 1.5 in arbitrary units. Likewise, we normalized the maximum of the calculated spectra to 1 in the same arbitrary units.

In each of the optical absorption spectra, the first peak corresponds to the first excitation associated to van Hove singularities, i.e., the E_{11} transition. The second highest peak corresponds

*This work was performed in collaboration with Víctor Alexander Torres-Sánchez and Duncan John Mowbray, and is adapted from “Optical and Energy Loss Spectroscopy of Single-Walled Carbon Nanotubes”, *submitted*, 2019.^{119,124}

Table 4.1: Relaxed single-walled carbon nanotube (SWCNT) diameters d in Å, unit cell lengths L in Å, numbers of atoms N_{at} per unit cell, and derivative discontinuity corrections Δ_x and electronic band gaps E_{gap} in eV.

SWNT	d (Å)	L (Å)	N_{at}	Δ_x (eV)	E_{gap} (eV)
(6,4)	6.97	18.64	152	0.418	1.475
(9,1)	7.62	40.81	364	0.417	1.476
(8,3)	7.84	42.12	388	0.399	1.414
(6,5)	7.60	40.83	364	0.374	1.317
(7,3)	7.09	38.06	316	0.365	1.281
(7,5)	8.31	44.68	436	0.360	1.273
(10,2)	8.84	23.80	248	0.358	1.269
(9,4)	9.17	49.33	532	0.339	1.199
(8,4)	8.40	11.34	112	0.329	1.158
(7,6)	8.97	48.21	508	0.315	1.113
(10,3)	9.36	50.47	556	0.278	0.983
(11,1)	9.16	49.35	532	0.269	0.950
(10,8)	12.38	33.37	488	0.240	0.849
(9,8)	11.66	63.02	868	0.246	0.869
(11,3)	10.13	54.63	652	0.310	1.098
(11,5)	11.22	20.20	268	—	—
(12,3)	10.89	6.51	84	—	—
(10,4)	9.91	8.91	104	—	—
(7,4)	7.70	13.69	124	—	—

to the second excitation of this kind, E_{22} . We were able to resolve in some cases a peak between these two, such as in the (9,4), (9,1), (8,3), (7,5) and (9,4). We can also observe excitations higher in energy than the E_{22} , but they do not seem to match any of the transitions obtained

experimentally. From hereon, we shall restrict our discussion to the E_{11} and the E_{22} excitations.

All the spectra were calculated by using the derivative discontinuity correction of the exchange part of the GLLB-SC functional. This not only shifted the energies, yielding a good description of the first excitation energy E_{11} or the band gap, but also changed the intensities of all the spectrum following Eq. 3.1.

For all the SWCNTs there is semi-quantitative agreement in the description of the relative intensities and positions of the E_{11} and E_{22} transitions. We find that the E_{11} transition is more intense than the E_{22} , except in the case of the (9,1) SWCNT. The first transition being more intense than the second transition is a feature also observed in the experimental data.

When comparing the spectra of all the SWCNTs, we find that the energies of the E_{22} transitions are not at all correlated to those of the E_{11} transitions. The energies of these two transitions are neither separated by the same amount nor is one proportional to the other. In some cases they are closer than in others. Although the E_{11} and the E_{22} transitions are uncorrelated, the spectra calculated with the LCAO-TDDFT- k - ω code was able to reproduce semi-quantitatively the values of these transitions energies.

The optical absorption spectra showed in Figure 4.5 corresponds to the first 12 SWCNTs listed in Table 4.1, which vary widely in length and number of atoms per unit cell. We can observe that the spectra calculated using the LCAO-TDDFT- k - ω code reproduce the features of the experimental data of these very different SWCNTs, showing that it is surprisingly robust when calculating the optical absorbance of carbon-based one-dimensional nanostructures.

In order to calculate the optical absorption spectra of SWCNTs with large unit cells, it was also necessary to implement the domain decomposition of the real space grids. This type of parallelization, used along with parallelization over k -points, allowed us to carry out the calculations with limited computational resources.

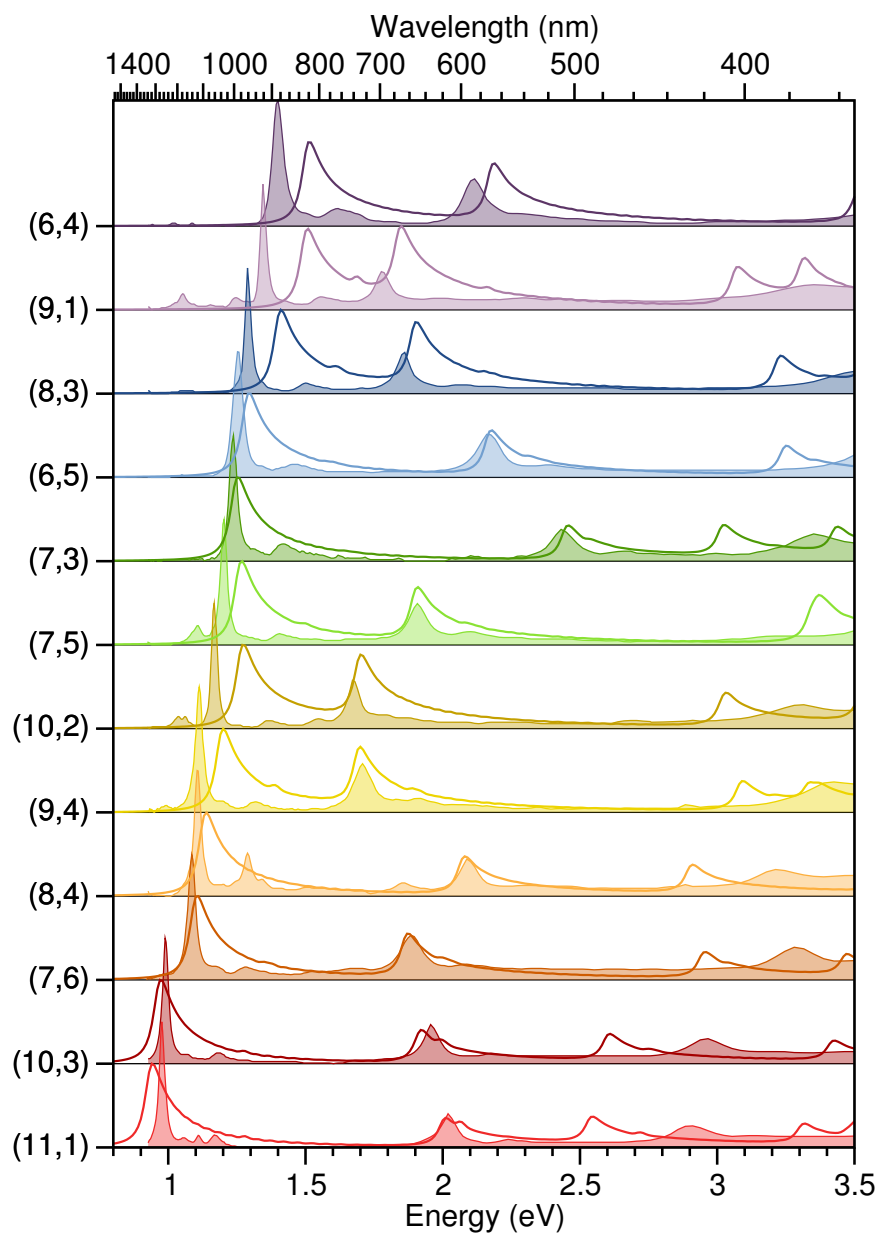


Figure 4.5: Comparison of LCAO-TDDFT- k - ω calculated (solid lines) and measured (filled regions) optical absorbance $\Im[\epsilon(\omega)]$ spectra along the SWCNT axis in nm (upper axis) and eV (lower axis) for chirality sorted (6,4), (9,1), (8,3), (6,5), (7,3), (7,5), (10,2), (9,4), (8,4), (7,6), (10,3), and (11,1) SWCNTs shown in Fig. 3.2. Experimental spectra were taken from Ref. 115.

4.2.2 E_{11} and E_{22} Transitions

In Figure 4.6 we compare the experimental values of the electronic band gaps E_{11} from optical absorption and electron loss spectroscopy of References 115 and 48 to the our theoretical DFT values. We also compare the values obtained with the derivative discontinuity correction of the exchange part of the GLLB-SC functional (squares) and without this correction, that is, using only the PBEsol exchange and correlation functional (circles).

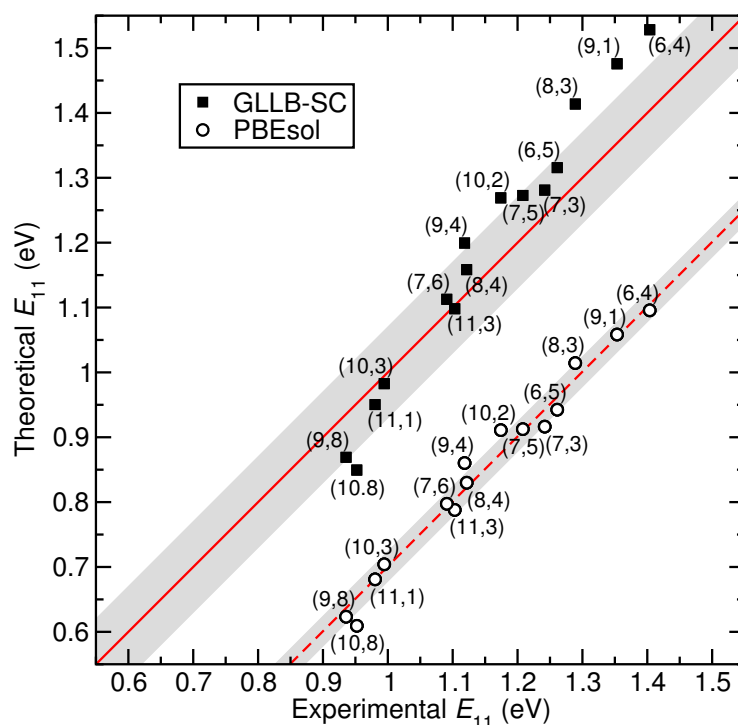


Figure 4.6: Comparison of theoretical DFT electronic band gaps, E_{11} , in eV with (GLLB-SC⁸⁰, filled squares) and without (PBEsol⁷⁷, open circles) including the derivative discontinuity correction with experimental E_{11} transitions obtained from optical absorbance and electron energy loss measurements of fifteen different chirality sorted SWCNT samples from Refs. 115 and 48, respectively. The standard deviation for GLLB-SC ($\sigma \approx 70$ meV) and average error for PBEsol ($\epsilon \approx -0.30 \pm 0.03$ eV) are shown as grey regions and red solid and dashed lines, respectively.

The PBEsol functional yields an estimation of the band gap with an average error of $\epsilon \approx -0.30 \pm 0.02$ eV. It reproduces the trend better than in the case of GLLB-SC functional but the band gap is always underestimated. When we add the derivative discontinuity correction of the GLLB-SC functional, the average error is $\epsilon \approx 0.04 \pm 0.07$ eV, that is, much smaller than when not adding the correction and well within the expected 0.1 eV accuracy of DFT calculations. Nevertheless, the standard deviation is somewhat larger. This shows that it is important to use the derivative discontinuity correction of the GLLB-SC functional to properly describe the band gaps and have a better agreement with the experimental band gaps of SWCNTs.

In Figure 4.7, we compare the experimental values of transitions energies E_{22} and their corresponding theoretical DFT calculated values. We show in this case just the calculated transition with the derivative discontinuity correction of the GLLB-SC functional. We were able to obtain a better agreement than in the estimation of the E_{11} case because the error was $\epsilon \approx 26 \pm 33$ meV, so again well within the expected 0.1 eV accuracy of DFT calculations.

Based on the results of this subsection and the previous one, we have shown that the LCAO-TDDFT- k - ω code can reproduce with great accuracy the uncorrelated E_{11} and E_{22} transitions energies for SWCNTs. Moreover, the fact that we are obtaining such a good agreement suggests that we are considering almost all the processes that are taking place during the optical absorption. This also means that absorptions that include charge transfer, which are not described by our method, do not occur.

4.2.3 Electron Energy Loss Spectroscopy

We have so far looked at the optical absorption spectra calculated using the LCAO-TDDFT- k - ω code, which was defined as the imaginary part of the dielectric function, $\Im[\epsilon(\omega)]$, for semiconducting SWCNTs. Now we will look at the EELS of both metallic and semiconducting SWCNTs. In so doing we are able to also assess the accuracy of the real part of the dielectric function, $\Re[\epsilon(\omega)]$. This is because the EELS is the negative of the imaginary part of the inverse of the dielectric function, $-\Im[\epsilon^{-1}(\omega)]$, i.e., $\frac{\Im[\epsilon(\omega)]}{\Re[\epsilon(\omega)]^2 + \Im[\epsilon(\omega)]^2}$. In this way, we are assessing the robustness of the LCAO-TDDFT- k - ω code by looking at another of its outputs. Furthermore, the

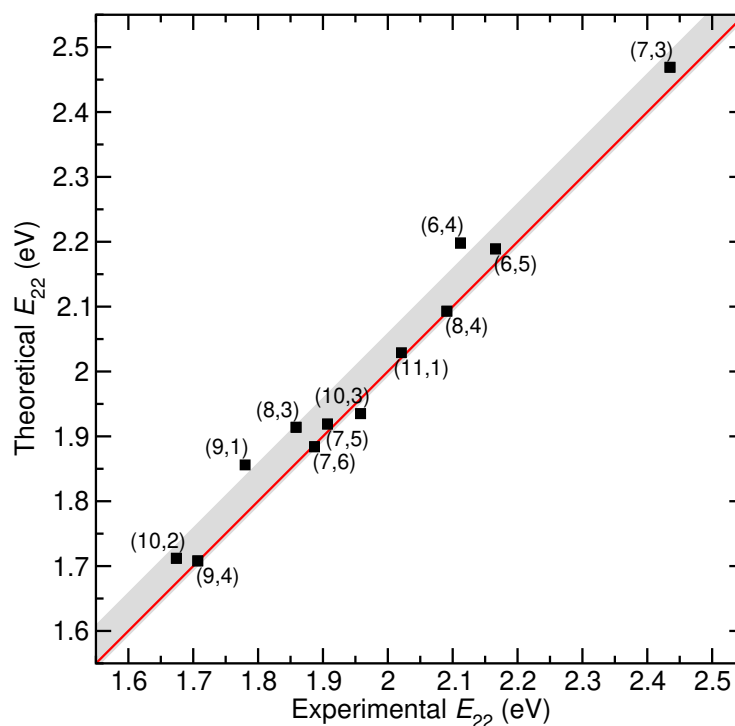


Figure 4.7: Comparison of theoretical and experimental E_{22} transitions in eV from LCAO-TDDFT- k - ω including the derivative discontinuity correction and optical absorbance measurements in Fig. 4.5 from Ref. 115 for twelve different chirality sorted SWCNT samples shown in Fig. 3.2. The average error is $\epsilon \approx 26 \pm 33$ meV (grey region).

comparison will be done with respect to measured spectra that correspond to different experiments than those used in Section 4.2.1.

In Figure 4.8(a) we show the experimentally measured EELS of semiconducting SWCNTs from Ref. 48, represented by filled regions. They are compared to the theoretical DFT EELS calculated using the LCAO-TDDF- k - ω code, represented by solid lines. We observe for all five semiconducting SWCNTs that the first and second peaks are blue-shifted with respect to the measured spectra by about 0.2 and 0.4 eV on average, respectively. These peaks are the assigned the E_{11} and E_{22} interband transitions.

Following these two peaks there is a trough and one, two or three intermediate peaks before

a broader and last peak in the measured spectra. The third of all the peaks, that is, the first of the intermediate peaks or the one right after the trough, is always red-shifted with respect to the measured spectra by about 0.37 eV on average. These intermediate peaks correspond to the E_{33} , E_{44} and E_{55} interband transitions which can be easily identified in the spectra of the (10,8) and the (9,8) SWCNTs.

The broader and last peak is blue-shifted by about 0.29 eV on average but it has not been assigned a specific transition. The spectra have the same behavior in general up to an energy shift, but in the spectra of the (8,4) and the (8,3) SWCNTs the peaks are closer together and harder to recognize. As in the experimental results, the spectra present a monotonic downshift as the diameter of the SWCNT increases.

Turning to an analysis of the metallic SWCNTs' EELS in Figure 4.8(b), we observe a strong peak at around 1 eV (marked with an *) that matches what is observed in the experimental spectra. An exception to this is the spectrum of the (7,4) nanotube where a peak is observed but not as strong as in the theoretical spectrum. These peaks, which are present only in the spectra of metallic SWCNTs, correspond to free charge carrier plasmons. This means an intraband excitation that causes quantized collective oscillations of electrons. More specifically, these would correspond to Drude plasmons.

Going higher in energy, there is a trough and three well-known peaks. The first two of these peaks correspond to E_{11} transitions, which we can label M_{11} as the nanotubes are metallic. The splitting of the transition into two peaks is probably caused by the trigonal wrapping effect⁴⁸. The third peak corresponds to the M_{22} transition. All of these transitions can be compared to peaks in the experimental data, although they are red-shifted by about 0.15 eV. Finally, the broader peak that was not assigned to any transition is blue-shifted by about 0.28 eV. We also observe intense peaks that do not match any in the spectra beyond the 5 eV in the (11,5) and (12,3) SWCNTs.

In summary, we obtained an accurate energy for the plasmonic transition and also a qualitative description of the two peaks related to the M_{11} transition and the peak related to the M_{22} up to a red-shift. In this way we have assessed both the real and imaginary part of the dielectric function calculated using the LCAO-TDDFT- k - ω code.

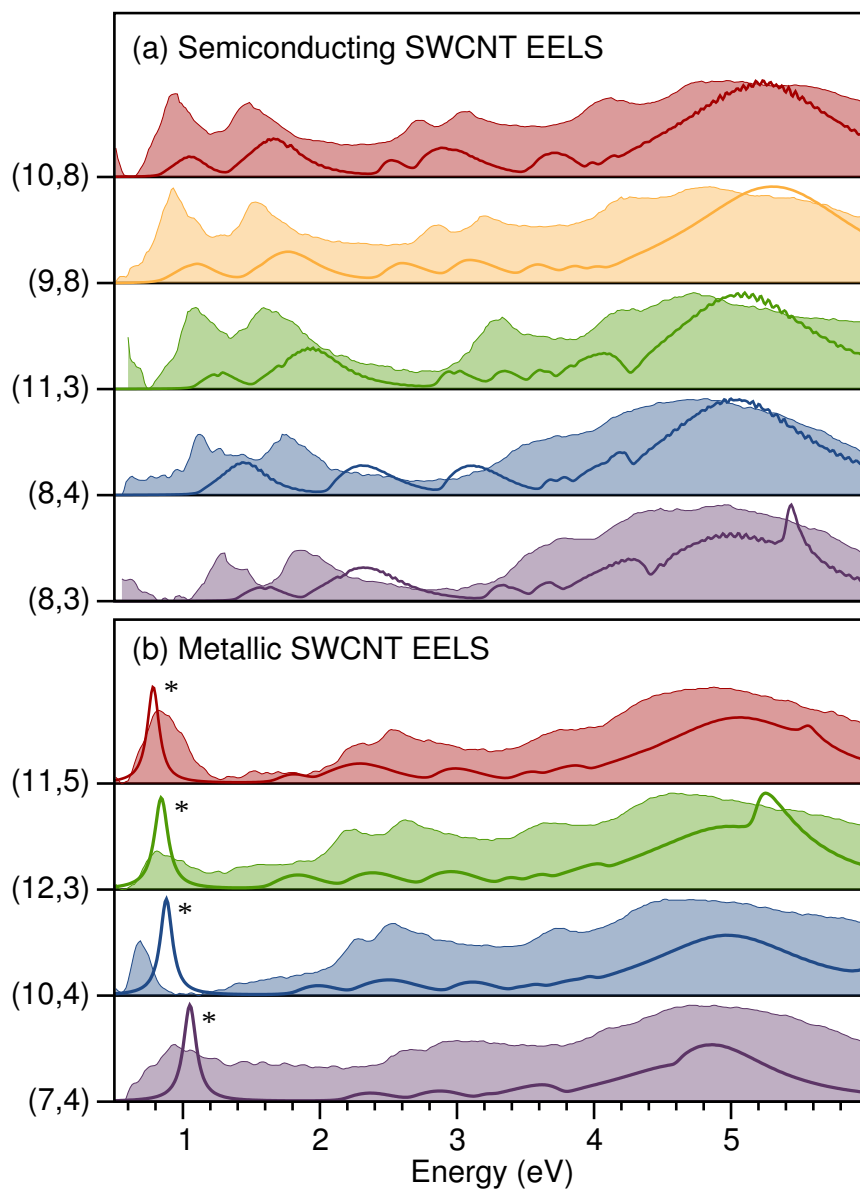


Figure 4.8: Comparison of LCAO-TDDFT- k - ω calculated (solid lines) and measured (filled regions) electron energy loss $\Im[\epsilon^{-1}(\omega)]$ spectra along the SWNT axis in eV for chirality sorted (a) semiconducting (10,8), (9,8), (11,3), (8,4), and (8,3) and (b) metallic (11,5), (12,3), (10,4) and (7,4) SWNTs. Experimental spectra were taken from Ref. 48. Drude metallic plasmons (*) are marked.

4.2.4 Excitonic Density

In Figure 4.9 we show the spatially resolved electron-hole density difference $\Delta\rho(\mathbf{r}, \omega)$. The blue isosurfaces correspond to negative density difference and the red isosurfaces to positive density difference. This provides us insight into the exciton density distribution at the $E_{11} = 1.48$ eV transition of the (6,4) SWCNT. We observe that the positive (or hole) density is distributed in a kind of continuous spiral around the nanotube and that the negative (or electron) density follows the same pattern but is not continuous.

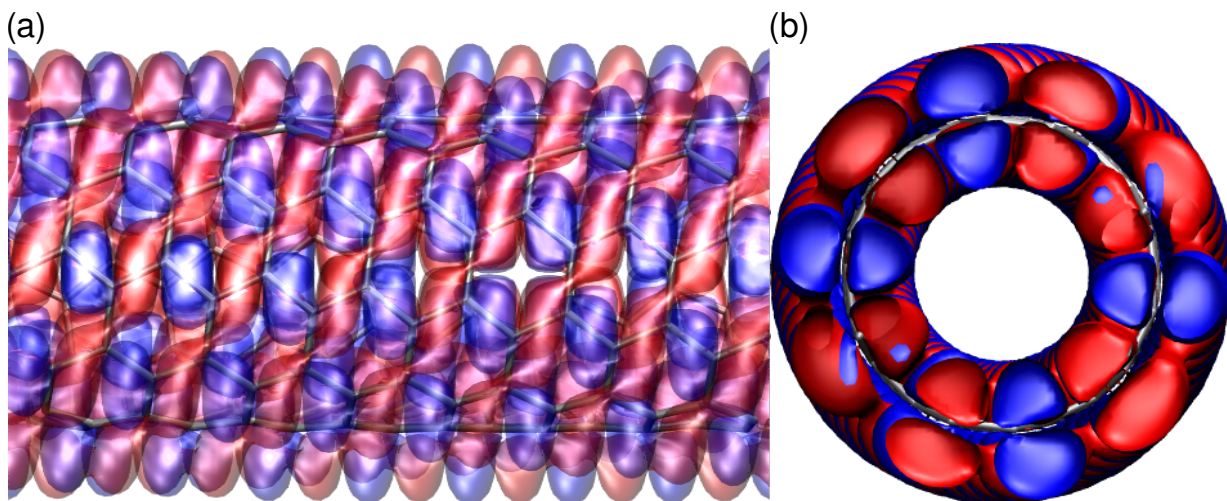


Figure 4.9: The exciton density difference positive (red) and negative (blue) isosurfaces for the (6,4) SWCNT corresponding to an absorption induced transition at 1.53 eV (a) along the z axis and (b) in the xy plane. The density difference corresponds to $\Delta\rho(\mathbf{r}, \omega) = \pm 2 \times 10^5 e/\text{\AA}^3$ and we observe that it corresponds to a $\pi \rightarrow \pi$ orbitals transition.

In Figure 4.9(b) we show the electron-hole density difference isosurfaces seen along the z direction. The isosurfaces resemble π -orbitals. So the E_{11} transition is indeed a $\pi \rightarrow \pi$ transition.

4.3 Chlorophyll–Single-Walled Carbon Nanotube Combined System*

4.3.1 Optical Absorption

In the previous sections we have obtained semi-quantitative agreement when comparing the measured optical absorbance of chlorophyll structures and different SWCNTs with the optical spectra calculated using LCAO-TDDFT- k - ω code. Now we shall investigate properties related to the optical absorbance of a mixed system, Chl *a*/(6,4) SWCNT, as a candidate organic photovoltaic material.

We showed previously that the carbon chain of the Chl *a* molecule does not contribute to the optical absorption spectrum either experimentally or theoretically. For this reason, in this section we are going to use the cut structure of Chl *a* to study a mixed system, that is, the cut Chl *a* on top of the (6,4) SWCNT. From hereon we shall omit “cut” and “SW” to simply our notation.

As we are proposing the mixed system Chl *a*/(6,4) CNT, there is no experimental data available to compare with our results. However, we can rely on the optical absorbance we obtain, up to a given point, based on the reliability of our results of the individual molecules in Sections 4.1.1 and 4.2.1. In Figure 4.10 we show the theoretical DFT optical absorption spectrum of the combined system and observe that it has more peaks or transitions than either of the individual spectra.

We may match the transitions of the molecules alone to the spectra of the combined system. For example, the first peak at 1.48 eV could correspond to the E_{11} transition of the (6,4) CNT at 1.52 eV and the third peak at 2.17 eV could correspond to the E_{22} transition of the CNT. Likewise, the fourth peak at 2.45 eV may be matched to the first transition at 2.38 eV in the y direction of the Chl *a* molecule and the peak at around 2.75 eV to the second transition at 2.88 eV. Of course, these transitions are in some way kept in the combined system, but the resonant energies are blue or red-shifted.

This is not the case for a peak in the spectrum of the combined system Chl *a*/(6,4) CNT at

*This work was performed in collaboration with Duncan John Mowbray and will also be included on “Theoretical Spectroscopy of a Single-Walled Carbon Nanotube with a Modified Chlorophyll Molecule”, *in preparation*, 2019.

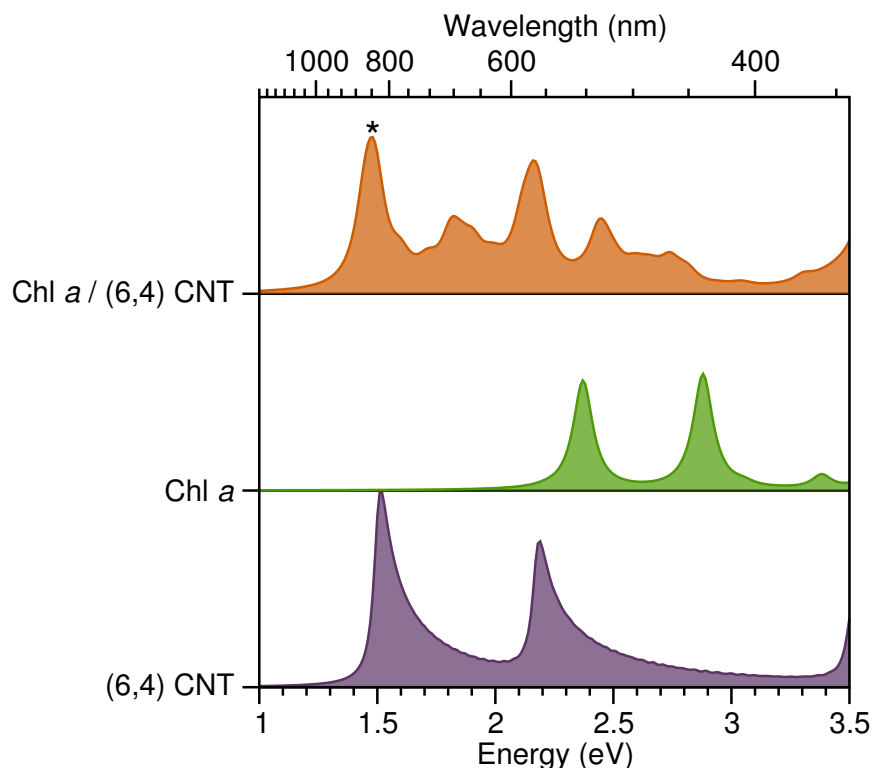


Figure 4.10: Optical absorption spectra of the mixed system Chl *a*/(6,4) SWCNT (orange) along the *z* direction or the nanotube axis compared to those of the Chl *a* molecule along the *y* axis (green) and the (6,4) SWCNT alone (violet) along the SWCNT axis in eV.

1.83 eV. We could not match it to a transition of the chlorophyll molecules nor the carbon nanotube. This could be a new excitation with a transition from one molecule to the other. In the following section we use the spatial distribution of the exciton density difference to provide quantitative insight into the nature of the transitions of the combined system.

4.3.2 Excitonic Density

In order to provide insight into the excitonic density of the combined system, we have plotted in Figure 4.11 the spatially resolved electron-hole density difference $\Delta\rho(\mathbf{r}, \omega)$. Again, the blue/red isosurfaces correspond to the negative/positive density difference. It is observed that, for the

same cutoff we chose to plot the isosurfaces, the positive or hole density is only in the Chl *a* molecule and that the negative or electron density is only in the CNT.

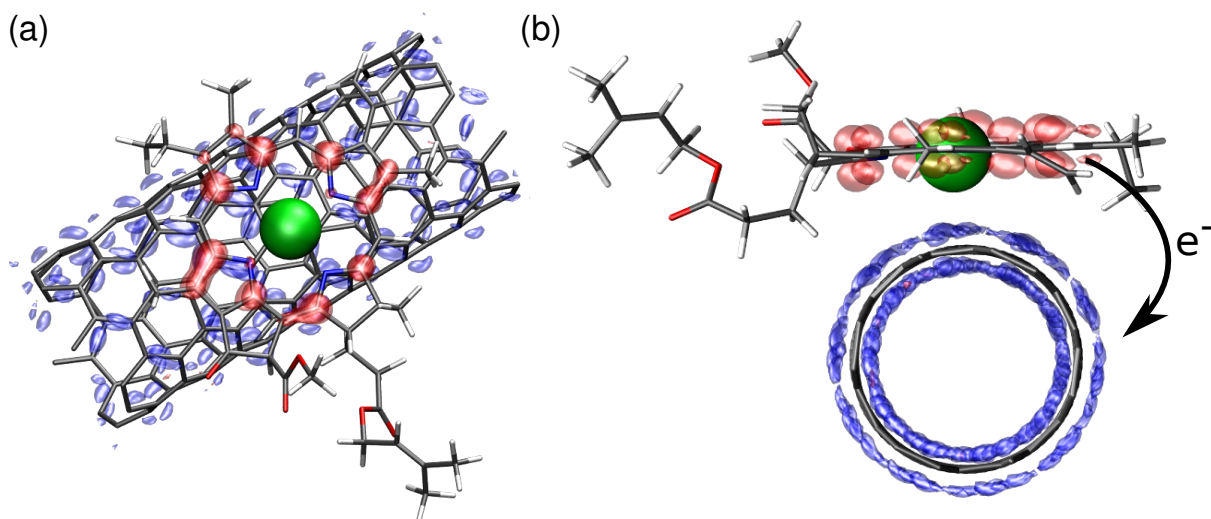


Figure 4.11: The exciton density difference positive (red) and negative (blue) isosurfaces for the combined system Chl *a*/(6,4) CNT corresponding to an absorption induced transition at ~ 1.4 eV (a) along the z axis and (b) in the xy plane. A charge separation is observed where an electron is going from the Chl *a* molecule to the (6,4) CNT.

Because the direction of the excitation was along the CNT axis, and therefore perpendicular to the carbon chain, we consider it appropriate to compare the excitations to the HOMO \rightarrow LUMO+1 transition of the *cut* Chl *a* that are plotted in Fig. A.2. We observe in Figure 4.11(a) that the hole isosurfaces are distributed in the chlorin ring with very small or no concentration in the N atoms.

In Figure 4.11(b) we see that the electron density resembles the π orbitals, as in the excitonic density of the (6,4) CTN alone plotted in 4.9. We also find that the hole density has a π orbital distribution. From this we can say that negative charge, that is, an electron, is excited from the chlorophyll molecule to the carbon nanotube by a $\pi \rightarrow \pi$ transition. This finding provides clear evidence of electron–hole spatial separation for the first bright exciton of a Chl *a*/(6,4) CNT network, which is an important result for assessing the feasibility of employing this system in a photovoltaic cells.

Chapter 5

Conclusions & Outlook

In this thesis, we have looked at the optical absorption of chlorophyll *a* and *b* monomers in gas phase, of 14 semiconducting and four metallic single-walled carbon nanotubes, and a combined system of the two. We have also obtained the electron energy loss spectra for some single-walled carbon nanotubes (SWCNTs) and provided insight into the spatial distribution of photoinduced excitations.

We first assessed the dependence on the basis set of the optical absorption spectrum for *cut* chlorophyll (Chl) *a* and found that the DZP basis set within the linear combination of atomic orbitals (LCAO) mode was necessary and sufficient to ensure a convergence to the complete basis set limit. This was done by comparing the spectra calculated with a DZP basis set to the one calculated using a plane wave representation of the Kohn-Sham (KS) wavefunctions. We then restricted the usage to the DZP basis set to calculate the optical absorbance of charged or neutral, *full* or *cut* structures of Chl *a* and Chl *b* monomers, made direct comparisons to the experimental data of the same molecules in gas phase, and found a semi-quantitative agreement when adding the derivative discontinuity corrections of the exchange part of the Gritsenko-Leeuwen-Lenthe-Baerends solid and correlation (GLLB-SC) functional. We also used the excitonic density distribution to show that the carbon chain of Chl molecules does not contribute to the optical absorbance and that it was centered principally on the chlorin ring.

We then turned to an analysis of the optical absorption and electron energy loss spectra of

single-walled carbon nanotubes, one dimensional structures with properties determined by their (m, n) indices. We looked at nanotubes with very different indices and found that our theoretical optical absorption spectra, given by the imaginary part of the dielectric function, agree semi-quantitatively with the experimental data when the derivative discontinuity correction of the GLLB-SC functional is added. We also found that the E_{11} transition or band gap energies have an average error much smaller than the expected accuracy of density functional theory (DFT) calculations. We also found that E_{22} transition energies had even better agreement than the E_{11} . This last result was rather surprising because the E_{11} and E_{22} energies seem to be uncorrelated. Furthermore, we assessed the real part of the dielectric function by comparing the calculated electron energy loss spectra to experimental data. We were able to reproduce the qualitative behavior of the spectra and to get an accurate energy for the plasmonic transition in the case of the metallic SWCNTs.

Finally, we looked at a combined system that contained both a chlorophyll monomer and a single-walled carbon nanotube. Although we did not have experimental data to compare with we could rely on our results because the theoretical spectra were already assessed for the separated molecules, yielding a semi-quantitative agreement. We found that the spectra of the Chl *a*/(6,4) SWCNT was not merely the sum of the absorption of the separated molecules. Specifically, there was a transition at 1.83 eV that could not be matched to any transitions from the SWCNT or the Chl molecule. Such results may be attributed to excitations occurring between the molecules. One example of this was observed when plotting the spatially resolved electron-hole density difference of the first transition of the combined system, where the exciton had the electron density in the nanotube but the hole density in the chlorophyll molecule.

Because of the photoinduced separation of charges, this last result has placed the combined system Chl *a*/(6,4) CNT as a potential material to be used in organic photovoltaics (OPVs). Even though we do not have experimental data to compare with, we already assessed the LCAO-TDDFT- k - ω code for the constituent molecules of the system and obtained very accurate results with a reduction of the computational effort. The methods we used in order to do so can be employed to study other π conjugated systems in gas phase and carbon-based nanostructures. In this way our results will contribute to the development of next generation organic photovoltaics.

However, there is still a long way to go in order to have an actual organic photovoltaic device with the combined system we proposed. Some of the remaining steps include design of the complete circuit. This involves both seeking for optimal materials or molecules suitable for this task and calculating the resulting cells' quantum efficiency. Another project than can be developed from the work of this thesis is to study the intraband transitions that are related to plasmons in metallic SWCTNs by using the method we employed to get the electron-hole density difference. Finally, we also encourage any experimental study than can be done with the proposed system and that could be compared to our theoretical calculations.

Appendix A

Excitations of $full\cdot 1^+$ and $cut\cdot 1^+$ Structures

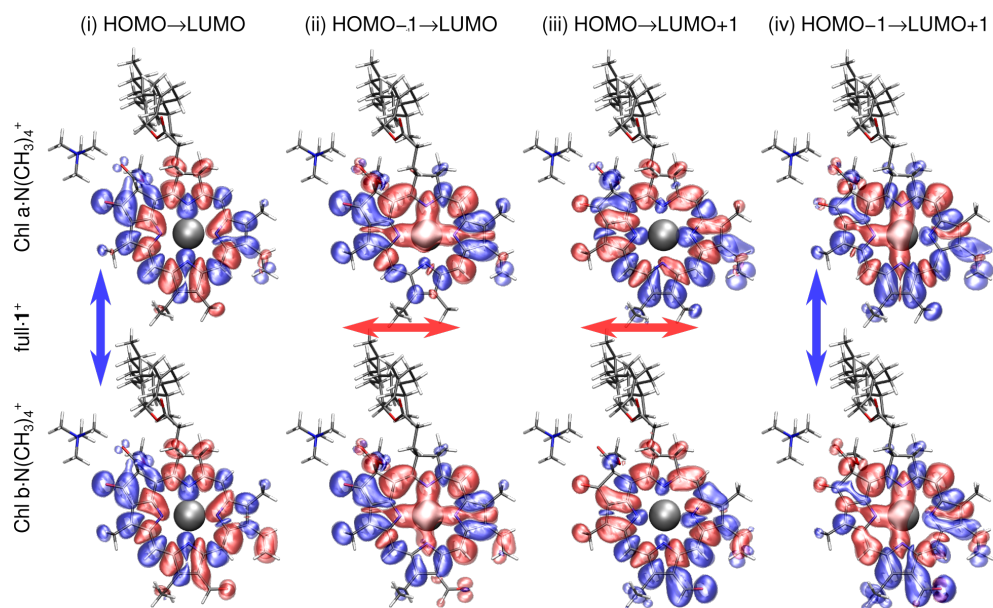


Figure A.1: Isosurfaces of the electron (blue) and hole (red) densities $\rho(\mathbf{r}) = \pm 0.001 e/\text{\AA}^3$ of the first four excitations of charge tagged Chl $a\cdot N(\text{CH}_3)_4^+$ and Chl $b\cdot N(\text{CH}_3)_4^+$ with a full hydrocarbon chain ($full\cdot 1^+$) (i) HOMO \rightarrow LUMO, (ii) HOMO-1 \rightarrow LUMO, (iii) HOMO \rightarrow LUMO+1, and (iv) HOMO-1 \rightarrow LUMO+1. Mg, C, O, N, and H atoms are depicted in silver, grey, red, blue, and white.

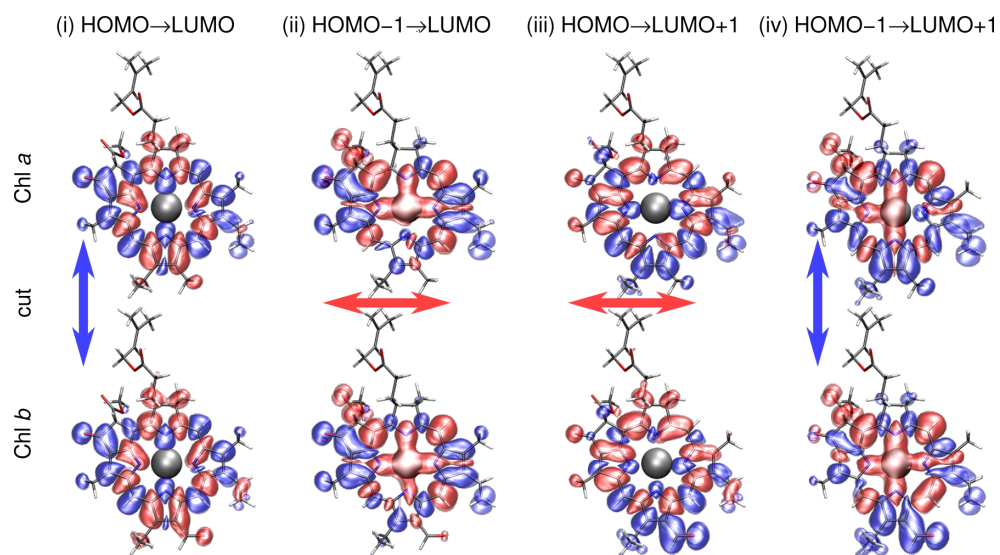


Figure A.2: Isosurfaces of the electron (blue) and hole (red) densities $\rho(\mathbf{r}) = \pm 0.001 e/\text{\AA}^3$ of the first four excitations of neutral Chl *a* and Chl *b* with a cut hydrocarbon chain (cut) (i) HOMO → LUMO, (ii) HOMO-1 → LUMO, (iii) HOMO → LUMO+1, and (iv) HOMO-1 → LUMO+1.

Additionally, the *CIF* of the structures used in this thesis are available in <https://drive.google.com/drive/folders/1dPpHdEGbidvguAdPpHTc7FSgGD-IugJm?usp=sharing>.

Bibliography

- [1] Agencia de Regulación y Control de Electricidad, Balance Nacional de Energía Eléctrica. 2018; <https://www.regulacionelectrica.gob.ec/balance-nacional/>.
- [2] Habas, S. E.; Platt, H. A. S.; van Hest, M. F. A. M.; Ginley, D. S. Low-Cost Inorganic Solar Cells: From Ink To Printed Device. *Chemical Reviews* **2010**, *110*, 6571–6594, PMID: 20973478.
- [3] Bergmann, R. Crystalline Si thin-film solar cells: a review. *Applied Physics A: Materials Science & Processing* **1999**, *69*, 187–194.
- [4] Li, B.; Wang, L.; Kang, B.; Wang, P.; Qiu, Y. Review of recent progress in solid-state dye-sensitized solar cells. *Solar Energy Materials and Solar Cells* **2006**, *90*, 549–573.
- [5] Green, M. A.; Emery, K.; Hishikawa, Y.; Warta, W.; Dunlop, E. D. Solar cell efficiency tables (Version 45). *Progress in Photovoltaics: Research and Applications* **2014**, *23*, 1–9.
- [6] Hoppe, H.; Sariciftci, N. S. Organic solar cells: An overview. *Journal of Materials Research* **2004**, *19*, 1924–1945.
- [7] Shockley, W.; Queisser, H. J. Detailed Balance Limit of Efficiency of p-n Junction Solar Cells. *Journal of Applied Physics* **1961**, *32*, 510–519.
- [8] Rühle, S. Tabulated values of the Shockley-Queisser limit for single junction solar cells. *Solar Energy* **2016**, *130*, 139 – 147.

- [9] Grätzel, M. Dye-sensitized solar cells. *Journal of Photochemistry and Photobiology C: Photochemistry Reviews* **2003**, *4*, 145–153.
- [10] Kim, H.; Nam, S.; Jeong, J.; Lee, S.; Seo, J.; Han, H.; Kim, Y. Organic solar cells based on conjugated polymers: History and recent advances. *Korean Journal of Chemical Engineering* **2014**, *31*, 1095–1104.
- [11] Yin, Z.; Zhu, J.; He, Q.; Cao, X.; Tan, C.; Chen, H.; Yan, Q.; Zhang, H. Graphene-Based Materials for Solar Cell Applications. *Advanced Energy Materials* **2013**, *4*, 1300574.
- [12] Miao, X.; Tongay, S.; Petterson, M. K.; Berke, K.; Rinzler, A. G.; Appleton, B. R.; Hebard, A. F. High Efficiency Graphene Solar Cells by Chemical Doping. *Nano Letters* **2012**, *12*, 2745–2750.
- [13] Falke, S. M.; Rozzi, C. A.; Brida, D.; Maiuri, M.; Amato, M.; Sommer, E.; Sio, A. D.; Rubio, A.; Cerullo, G.; Molinari, E.; Lienau, C. Coherent ultrafast charge transfer in an organic photovoltaic blend. *Science* **2014**, *344*, 1001–1005.
- [14] Wei, J.; Jia, Y.; Shu, Q.; Gu, Z.; Wang, K.; Zhuang, D.; Zhang, G.; Wang, Z.; Luo, J.; Cao, A.; Wu, D. Double-Walled Carbon Nanotube Solar Cells. *Nano Letters* **2007**, *7*, 2317–2321.
- [15] Baker, B.; Zhang, H.; Cha, T.-G.; Choi, J. *Carbon Nanotubes and Graphene for Photonic Applications*; Elsevier, 2013; pp 241–269.
- [16] Kirk, A. *Solar photovoltaic cells : photons to electricity*; Academic Press: London, 2015; Chapter 3, pp 25–40.
- [17] Bisquert, J. *The physics of solar cells : perovskites, organics, and photovoltaic fundamentals*; CRC Press, Taylor & Francis Group: Boca Raton, FL, 2018.
- [18] Goetzberger, A.; Knobloch, J.; Voss, B. Crystalline silicon solar cells. *editorial John Wiley & Sons Ltd* **1998**, *1*.

- [19] Britt, J.; Ferekides, C. Thin-film CdS/CdTe solar cell with 15.8% efficiency. *Applied physics letters* **1993**, *62*, 2851–2852.
- [20] Naghavi, N.; Spiering, S.; Powalla, M.; Cavana, B.; Lincot, D. High-efficiency copper indium gallium diselenide (CIGS) solar cells with indium sulfide buffer layers deposited by atomic layer chemical vapor deposition (ALCVD). *Progress in Photovoltaics: Research and Applications* **2003**, *11*, 437–443.
- [21] Bertness, K.; Kurtz, S. R.; Friedman, D. J.; Kibbler, A.; Kramer, C.; Olson, J. 29.5%-efficient GaInP/GaAs tandem solar cells. *Applied Physics Letters* **1994**, *65*, 989–991.
- [22] Nalwa, H. *Handbook of Advanced Electronic and Photonic Materials and Devices, Ten-Volume Set*; Handbook of Advanced Electronic and Photonic Materials and Devices; Elsevier Science, 2000; Chapter 1, pp 1–5.
- [23] Smith, M. *March's advanced organic chemistry: reactions, mechanisms, and structure*; Wiley-Interscience: Hoboken, N.J, 2007; Chapter 2, pp 32–46.
- [24] Baughman, R. H.; Zakhidov, A. A.; de Heer, W. A. Carbon nanotubes—the route toward applications. *Science* **2002**, *297*, 787–792.
- [25] Dresselhaus, M. S., Dresselhaus, G., Avouris, P., Eds. *Carbon Nanotubes: Synthesis, Structure, Properties, and Applications*; Springer: Berlin, 2001.
- [26] Spataru, C. D.; Ismail-Beigi, S.; Benedict, L. X.; Louie, S. G. Excitonic Effects and Optical Spectra of Single-Walled Carbon Nanotubes. *Phys. Rev. Lett.* **2004**, *92*, 077402.
- [27] Kataura, H.; Kumazawa, Y.; Maniwa, Y.; Umezue, I.; Suzuki, S.; Ohtsuka, Y.; Achiba, Y. Optical properties of single-wall carbon nanotubes. *Syn. Metals* **1999**, *103*, 2555–2558.
- [28] Yamamoto, T.; Watanabe, K.; Hernández, E. R. In *Carbon Nanotubes: Advanced Topics in the Synthesis, Structure, Properties and Applications*; Jorio, A., Dresselhaus, G., Dresselhaus, M. S., Eds.; Springer Berlin Heidelberg: Berlin, Heidelberg, 2008; pp 165–195.

- [29] Liew, K. M.; Wong, C. H.; He, X. Q.; Tan, M. J. Thermal stability of single and multi-walled carbon nanotubes. *Phys. Rev. B* **2005**, *71*, 075424.
- [30] Liang, W.; Bockrath, M.; Bozovic, D.; Hafner, J. H.; Tinkham, M.; Park, H. Fabry-Perot interference in a nanotube electron waveguide. *Nature* **2001**, *411*, 665.
- [31] Frank, S.; Poncharal, P.; Wang, Z.; De Heer, W. A. Carbon nanotube quantum resistors. *Science* **1998**, *280*, 1744–1746.
- [32] Liu, H.; Nishide, D.; Tanaka, T.; Kataura, H. Large-scale single-chirality separation of single-wall carbon nanotubes by simple gel chromatography. *Nat. Commun.* **2011**, *2*, 309.
- [33] Kymakis, E.; Amaratunga, G. Single-wall carbon nanotube/conjugated polymer photovoltaic devices. *Applied Physics Letters* **2002**, *80*, 112–114.
- [34] Kymakis, E.; Koudoumas, E.; Franghiadakis, I.; Amaratunga, G. Post-fabrication annealing effects in polymer-nanotube photovoltaic cells. *Journal of Physics D: Applied Physics* **2006**, *39*, 1058.
- [35] Campidelli, S.; Ballesteros, B.; Filoramo, A.; Díaz, D.; de la Torre, G.; Torres, T.; Rahman, G. A.; Ehli, C.; Kiessling, D.; Werner, F. Facile decoration of functionalized single-wall carbon nanotubes with phthalocyanines via “click chemistry”. *Journal of the American Chemical Society* **2008**, *130*, 11503–11509.
- [36] Bartelmess, J.; Ballesteros, B.; de la Torre, G.; Kiessling, D.; Campidelli, S.; Prato, M.; Torres, T.; Guldi, D. M. Phthalocyanine-pyrene conjugates: a powerful approach toward carbon nanotube solar cells. *Journal of the American Chemical Society* **2010**, *132*, 16202–16211.
- [37] Guldi, D. M.; Rahman, G.; Prato, M.; Jux, N.; Qin, S.; Ford, W. Single-wall carbon nanotubes as integrative building blocks for solar-energy conversion. *Angewandte Chemie International Edition* **2005**, *44*, 2015–2018.

- [38] Ham, M.-H. *et al.* Photoelectrochemical complexes for solar energy conversion that chemically and autonomously regenerate. *Nature Chemistry* **2010**, *2*, 929–936.
- [39] Kiang, N. Y.; Siefert, J.; Govindjee,; Blankenship, R. E. Spectral Signatures of Photosynthesis. I. Review of Earth Organisms. *Astrobiology* **2007**, *7*, 222–251.
- [40] Kay, A.; Graetzel, M. Artificial photosynthesis. 1. Photosensitization of titania solar cells with chlorophyll derivatives and related natural porphyrins. *The Journal of Physical Chemistry* **1993**, *97*, 6272–6277.
- [41] Kumara, G.; Kaneko, S.; Okuya, M.; Onwona-Agyeman, B.; Konno, A.; Tennakone, K. Shiso leaf pigments for dye-sensitized solid-state solar cell. *Solar Energy Materials and Solar Cells* **2006**, *90*, 1220–1226.
- [42] Amao, Y.; Yamada, Y.; Aoki, K. Preparation and properties of dye-sensitized solar cell using chlorophyll derivative immobilized TiO₂ film electrode. *Journal of Photochemistry and Photobiology A: Chemistry* **2004**, *164*, 47–51.
- [43] Moss, G. P. Nomenclature of Tetrapyrroles. *European Journal of Biochemistry* **1988**, *178*, 277–328.
- [44] Zamora-Ledezma, C.; Blanc, C.; Anglaret, E. Orientational order of single-wall carbon nanotubes in stretch-aligned photoluminescent composite films. *Phys. Rev. B* **2009**, *80*.
- [45] Torres-Canas, F. J.; Blanc, C.; Zamora-Ledezma, C.; Silva, P.; Anglaret, E. Dispersion and Individualization of SWNT in Surfactant-Free Suspensions and Composites of Hydrosoluble Polymers. *The Journal of Physical Chemistry C* **2014**, *119*, 703–709.
- [46] Weisman, R. B.; Kono, J. *Handbook of Carbon Nanomaterials*; World Scientific, 2019; pp 1–43.
- [47] Glanzmann, L. N.; Mowbray, D. J.; Figueroa del Valle, D. G.; Scotognella, F.; Lanzani, G.; Rubio, A. Photoinduced Absorption within Single-Walled Carbon Nanotube Systems. *The Journal of Physical Chemistry C* **2015**, *120*, 1926–1935.

- [48] Senga, R.; Pichler, T.; Suenaga, K. Electron Spectroscopy of Single Quantum Objects To Directly Correlate the Local Structure to Their Electronic Transport and Optical Properties. *Nano Letters* **2016**, *16*, 3661–3667.
- [49] Weisman, R. B.; Bachilo, S. M. Dependence of Optical Transition Energies on Structure for Single-Walled Carbon Nanotubes in Aqueous Suspension: An Empirical Kataura Plot. *Nano Letters* **2003**, *3*, 1235–1238.
- [50] Stockett, M. H.; Musbat, L.; Kjær, C.; Houmøller, J.; Toker, Y.; Rubio, A.; Milne, B. F.; Nielsen, S. B. The Soret absorption band of isolated chlorophyll a and b tagged with quaternary ammonium ions. *Physical Chemistry Chemical Physics* **2015**, *17*, 25793–25798.
- [51] Milne, B. F.; Kjaer, C.; Houmøller, J.; Stockett, M. H.; Toker, Y.; Rubio, A.; Nielsen, S. B. On the Exciton Coupling between Two Chlorophyll Pigments in the Absence of a Protein Environment: Intrinsic Effects Revealed by Theory and Experiment. *Angewandte Chemie International Edition* **2016**, *55*, 6248–6251.
- [52] Milne, B. F.; Toker, Y.; Rubio, A.; Nielsen, S. B. Unraveling the Intrinsic Color of Chlorophyll. *Angewandte Chemie International Edition* **2014**, *54*, 2170–2173.
- [53] Zangwill, A. A half century of density functional theory. *Physics Today* **2015**, *68*, 34–39.
- [54] Nørskov, J. K.; Bligaard, T.; Rossmeisl, J.; Christensen, C. H. Towards the computational design of solid catalysts. *Nature Chemistry* **2009**, *1*, 37–46.
- [55] Jain, A.; Ong, S. P.; Hautier, G.; Chen, W.; Richards, W. D.; Dacek, S.; Cholia, S.; Gunter, D.; Skinner, D.; Ceder, G.; Persson, K. A. Commentary: The Materials Project: A materials genome approach to accelerating materials innovation. *APL Materials* **2013**, *1*, 011002.
- [56] Glanzmann, L. N.; Mowbray, D. J. Theoretical Insight into the Internal Quantum Efficiencies of Polymer/C60 and Polymer/SWNT Photovoltaic Devices. *The Journal of Physical Chemistry C* **2016**, *120*, 6336–6343.

- [57] Jornet-Somoza, J.; Alberdi-Rodriguez, J.; Milne, B. F.; Andrade, X.; Marques, M. A. L.; Nogueira, F.; Oliveira, M. J. T.; Stewart, J. J. P.; Rubio, A. Insights into colour-tuning of chlorophyll optical response in green plants. *Physical Chemistry Chemical Physics* **2015**, *17*, 26599–26606.
- [58] Mortensen, J. J.; Hansen, L. B.; Jacobsen, K. W. Real-space grid implementation of the projector augmented wave method. *Phys. Rev. B* **2005**, *71*.
- [59] Larsen, A. H. *et al.* The atomic simulation environment – A Python library for working with atoms. *Journal of Physics: Condensed Matter* **2017**, *29*, 273002.
- [60] Schrödinger, E. An Undulatory Theory of the Mechanics of Atoms and Molecules. *Physical Review* **1926**, *28*, 1049–1070.
- [61] Haynes, P. D. Linear-scaling methods in *ab initio* quantum-mechanical calculations. Ph.D. thesis, University of Cambridge, Cambridge, 1998; Retrieved from <http://www.tcm.phy.cam.ac.uk/~pdh1001/thesis/>.
- [62] Born, M.; Oppenheimer, R. Zur Quantentheorie der Molekeln. *Annalen der Physik* **1927**, *389*, 457–484.
- [63] Monkhorst, H. J.; Pack, J. D. Special points for Brillouin-zone integrations. *Physical Review B* **1976**, *13*, 5188–5192.
- [64] Chadi, D. J.; Cohen, M. L. Special Points in the Brillouin Zone. *Physical Review B* **1973**, *8*, 5747–5753.
- [65] Wisesa, P.; McGill, K. A.; Mueller, T. Efficient generation of generalized Monkhorst-Pack grids through the use of informatics. *Phys. Rev. B* **2016**, *93*.
- [66] Hohenberg, P.; Kohn, W. Inhomogeneous Electron Gas. *Phys. Rev.* **1964**, *136*, B864–B871.
- [67] Engel, E. *Density functional theory: an advanced course*; Springer-Verlag: Berlin Heidelberg New York, 2011.

- [68] Kohn, W.; Sham, L. J. Self-Consistent Equations Including Exchange and Correlation Effects. *Phys. Rev.* **1965**, *140*, A1133–A1138.
- [69] Hartree, D. R. The Wave Mechanics of an Atom with a Non-Coulomb Central Field. Part I. Theory and Methods. *Math. Proc. Cambridge* **1928**, *24*, 89–110.
- [70] Glanzmann, L. N. Modelling of Polymer–Carbon Nanotube Heterojunctions for Photovoltaic Applications. Ph.D. thesis, University of the Basque Country UPV/EHU, 2017.
- [71] Feynman, R. P. Forces in Molecules. *Physical Review* **1939**, *56*, 340–343.
- [72] Perdew, J. P.; Zunger, A. Self-interaction correction to density-functional approximations for many-electron systems. *Phys. Rev. B* **1981**, *23*, 5048–5079.
- [73] Becke, A. D. Perspective: Fifty years of density-functional theory in chemical physics. *The Journal of Chemical Physics* **2014**, *140*, 18A301.
- [74] Perdew, J. P.; Burke, K.; Ernzerhof, M. Generalized Gradient Approximation Made Simple. *Phys. Rev. Lett.* **1996**, *77*, 3865–3868.
- [75] Zupan, A.; Burke, K.; Ernzerhof, M.; Perdew, J. P. Distributions and averages of electron density parameters: Explaining the effects of gradient corrections. *The Journal of Chemical Physics* **1997**, *106*, 10184–10193.
- [76] Perdew, J. P.; Ernzerhof, M.; Zupan, A.; Burke, K. Nonlocality of the density functional for exchange and correlation: Physical origins and chemical consequences. *The Journal of Chemical Physics* **1998**, *108*, 1522–1531.
- [77] Perdew, J. P.; Ruzsinszky, A.; Csonka, G. I.; Vydrov, O. A.; Scuseria, G. E.; Constantin, L. A.; Zhou, X.; Burke, K. Restoring the Density-Gradient Expansion for Exchange in Solids and Surfaces. *Physical Review Letters* **2008**, *100*.
- [78] Tran, F.; Ehsan, S.; Blaha, P. Assessment of the GLLB-SC potential for solid-state properties and attempts for improvement. *Physical Review Materials* **2018**, *2*.

- [79] Tran, F.; Blaha, P. Importance of the Kinetic Energy Density for Band Gap Calculations in Solids with Density Functional Theory. *The Journal of Physical Chemistry A* **2017**, *121*, 3318–3325.
- [80] Kuisma, M.; Ojanen, J.; Enkovaara, J.; Rantala, T. T. Kohn-Sham potential with discontinuity for band gap materials. *Phys. Rev. B* **2010**, *82*.
- [81] Gritsenko, O.; van Leeuwen, R.; van Lenthe, E.; Baerends, E. J. Self-consistent approximation to the Kohn-Sham exchange potential. *Physical Review A* **1995**, *51*, 1944–1954.
- [82] Gritsenko, O. V.; Leeuwen, R. V.; Baerends, E. J. Direct approximation of the long- and short-range components of the exchange-correlation Kohn-Sham potential. *International Journal of Quantum Chemistry* **1997**, *61*, 231–243.
- [83] Castelli, I. E.; Olsen, T.; Datta, S.; Landis, D. D.; Dahl, S.; Thygesen, K. S.; Jacobsen, K. W. Computational screening of perovskite metal oxides for optimal solar light capture. *Energy Environ. Sci.* **2012**, *5*, 5814–5819.
- [84] Chelikowsky, J. R.; Troullier, N.; Saad, Y. Finite-difference-pseudopotential method: Electronic structure calculations without a basis. *Physical Review Letters* **1994**, *72*, 1240–1243.
- [85] Briggs, E. L.; Sullivan, D. J.; Bernholc, J. Large-scale electronic-structure calculations with multigrid acceleration. *Phys. Rev. B* **1995**, *52*, R5471–R5474.
- [86] Marques, M. A. L.; Castro, A.; Bertsch, G. F.; Rubio, A. octopus: a first-principles tool for excited electron–ion dynamics. *Computer Physics Communications* **2003**, *151*, 60–78.
- [87] Heiskanen, M.; Torsti, T.; Puska, M. J.; Nieminen, R. M. Multigrid method for electronic structure calculations. *Physical Review B* **2001**, *63*.
- [88] Grossmann, C. *Numerical treatment of partial differential equations*; Springer: Berlin New York, 2007.

- [89] Clark, T.; Koch, R. *The Chemist's Electronic Book of Orbitals*; Springer Berlin Heidelberg, 1999; pp 5–22.
- [90] Artacho, E.; Anglada, E.; Diéguez, O.; Gale, J. D.; García, A.; Junquera, J.; Martin, R. M.; Ordejón, P.; Pruneda, J. M.; Sánchez-Portal, D.; Soler, J. M. The SIESTA method; developments and applicability. *Journal of Physics: Condensed Matter* **2008**, *20*, 064208.
- [91] Larsen, A. H.; Vanin, M.; Mortensen, J. J.; Thygesen, K. S.; Jacobsen, K. W. Localized Atomic Basis Set in the Projector Augmented Wave Method. *Phys. Rev. B* **2009**, *80*, 195112.
- [92] Sankey, O. F.; Niklewski, D. J. Ab initio multicenter tight-binding model for molecular-dynamics simulations and other applications in covalent systems. *Phys. Rev. B* **1989**, *40*, 3979.
- [93] Anglada, E.; M. Soler, J.; Junquera, J.; Artacho, E. Systematic generation of finite-range atomic basis sets for linear-scaling calculations. *Phys. Rev. B* **2002**, *66*, 205101.
- [94] Larsen, A. H. Localized Atomic Orbital Basis Sets in the Projector Augmented Wave Method. M.Sc. thesis, Technical University of Denmark, Denmark, 2008.
- [95] Vanin, M. Projector Augmented Wave Calculations with Localized Atomic Orbitals. M.Sc. thesis, Technical University of Denmark, Denmark, 2008.
- [96] Soler, J. M.; Artacho, E.; Gale, J. D.; Garcia, A.; Junquera, J.; Ordejón, P.; Sánchez-Portal, D. The SIESTA method for *ab initio* order-*N* materials simulation. *J. Phys.: Condens. Matter* **2002**, *14*, 2745.
- [97] Heine, V. *Solid State Physics*; Elsevier, 1970; pp 1–36.
- [98] Pickett, W. E. Pseudopotential methods in condensed matter applications. *Computer Physics Reports* **1989**, *9*, 115–197.

- [99] Slater, J. C. An Augmented Plane Wave Method for the Periodic Potential Problem. *Physical Review* **1953**, *92*, 603–608.
- [100] Blöchl, P. E. Projector augmented-wave method. *Physical Review B* **1994**, *50*, 17953–17979.
- [101] Blöchl, P. E.; Först, C. J.; Schimpl, J. Projector augmented wave method: ab initio molecular dynamics with full wave functions. *Bulletin of Materials Science* **2003**, *26*, 33–41.
- [102] Kresse, G.; Joubert, D. From ultrasoft pseudopotentials to the projector augmented-wave method. *Physical Review B* **1999**, *59*, 1758–1775.
- [103] Marques, M. A., Ullrich, C. A., Nogueira, F., Rubio, A., Burke, K., Gross, E. K. U., Eds. *Time-Dependent Density Functional Theory*; Springer Berlin Heidelberg, 2006.
- [104] Ullrich, C. A. *Time-Dependent Density-Functional Theory*; Oxford University Press, 2011.
- [105] Runge, E.; Gross, E. K. U. Density-Functional Theory for Time-Dependent Systems. *Phys. Rev. Lett.* **1984**, *52*, 997–1000.
- [106] Ullrich, C. A.; Yang, Z. H. A Brief Compendium of Time-Dependent Density Functional Theory. *Brazilian Journal of Physics* **2013**, *44*, 154–188.
- [107] Adler, S. L. Quantum Theory of the Dielectric Constant in Real Solids. *Phys. Rev.* **1962**, *126*, 413–420.
- [108] Onida, G.; Reining, L.; Rubio, A. Electronic Excitations: Density-Functional versus Many-Body Green's-Function Approaches. *Rev. Mod. Phys.* **2002**, *74*, 601–659.
- [109] Yan, J.; Thygesen, K. S.; Jacobsen, K. W. Nonlocal Screening of Plasmons in Graphene by Semiconducting and Metallic Substrates: First-Principles Calculations. *Phys. Rev. Lett.* **2011**, *106*, 146803.

- [110] Yan, J.; Mortensen, J. J.; Jacobsen, K. W.; Thygesen, K. S. Linear density response function in the projector augmented wave method: Applications to solids, surfaces, and interfaces. *Phys. Rev. B* **2011**, *83*, 245122.
- [111] Gross, J. *Pigments in Vegetables : Chlorophylls and Carotenoids*; Springer US Imprint Springer: Boston, MA, 1991.
- [112] Saito, R.; Dresselhaus, G.; Dresselhaus, M. *Physical Properties of Carbon Nanotubes*; Imperial College Press, London, 1998.
- [113] Lu, X.; Chen, Z. Curved Pi-Conjugation, Aromaticity, and the Related Chemistry of Small Fullerenes (<C60) and Single-Walled Carbon Nanotubes. *Chemical Reviews* **2005**, *105*, 3643–3696.
- [114] Weisman, R.; Subramoney, S. Carbon nanotubes. **2006**, *15*, 42–46.
- [115] Wei, X.; Tanaka, T.; Yomogida, Y.; Sato, N.; Saito, R.; Kataura, H. Experimental determination of excitonic band structures of single-walled carbon nanotubes using circular dichroism spectra. *Nat. Comm.* **2016**, *7*, 12899.
- [116] Scheer, H. *Chlorophylls and Bacteriochlorophylls: Biochemistry, Biophysics, Functions and Applications*; Advances in Photosynthesis and Respiration; Springer: Dordrecht, The Netherlands, 2006; Vol. 25; Chapter 1, pp 1–26.
- [117] GPAW developers, Carbon. <https://wiki.fysik.dtu.dk/gpaw/setups/C.html>.
- [118] Mowbray, D. J.; Migani, A.; Walther, G.; Cardamone, D. M.; Rubio, A. Gold and Methane: A Noble Combination for Delicate Oxidation. *The Journal of Physical Chemistry Letters* **2013**, *4*, 3006–3012.
- [119] Preciado-Rivas, M. R.; Torres-Sanchez, V. A.; Mowbray, D. J. Optical and Energy Loss Spectroscopy of Single-Walled Carbon Nanotubes. **2019**, submitted to Physical Review B.

-
- [120] Bahn, S. R.; Jacobsen, K. W. An Object-Oriented Scripting Interface to a Legacy Electronic Structure Code. *Comput. Sci. Eng.* **2002**, *4*, 56.
- [121] Bitzek, E.; Koskinen, P.; Gähler, F.; Moseler, M.; Gumbsch, P. Structural Relaxation Made Simple. *Physical Review Letters* **2006**, *97*.
- [122] Preciado-Rivas, M. R.; Mowbray, D. J.; Larsen, A. H.; Lyon, K.; Milne, B. F. Optical Excitations of Chlorophyll a and b Monomers and Dimers. **2019**, submitted to Journal of Chemical Physics.
- [123] Strange, M.; Kristensen, I. S.; Thygesen, K. S.; Jacobsen, K. W. Benchmark Density Functional Theory Calculations for Nanoscale Conductance. *J. Chem. Phys.* **2008**, *128*, 114714.
- [124] Kroeckel, C.; Preciado-Rivas, M. R.; Torres-Sanchez, V. A.; Mowbray, D. J.; Reich, S.; Hauke, F.; Chacon-Torres, J. C.; Hirsch, A. Understanding the electron-doping mechanism in single-walled carbon nanotubes. **2019**, in preparation.

Abbreviations

E_{11} first van Hove optical transition in SWCNTs xix, 4, 6, 40, 41, 59, 61, 63–66, 68, 69, 74

E_{22} second van Hove optical transition in SWCNTs xix, 7, 40, 41, 60, 61, 64, 65, 69, 74

APW augmented plane wave 28, 29

ASE atomic simulation environment 5

CBM conduction band minimum 23, 25

Chl chlorophyll xix, 3–7, 37, 38, 43–45, 48, 49, 51–55, 57–59, 69–71, 73, 74, 77, 78

DFT density functional theory 4, 5, 15, 16, 19, 25, 31, 44, 46, 53, 63–65, 69, 74

DNA deoxyribonucleic acid 3

DZ double- ζ 27, 51, 52

DZP double- ζ polarized 27, 46, 51–53, 73

EA electron affinity 23

EELS electron energy loss spectroscopy 4

GGA generalized gradient approximation 20, 21, 25, 44, 46

GLLB Gritsenko-Leeuwen-Lenthe-Baerends 24

GLLB-SC Gritsenko-Leeuwen-Lenthe-Baerends solid and correlation xi, xiii, xv, 5, 6, 24, 25, 44, 47, 53, 55, 59, 61, 63, 64, 73, 74

HOMO highest occupied molecular orbital 2, 17, 37, 57, 58, 71, 77, 78

IP ionization potential 23

- IPCE** incident photon-to-current efficiency 3
- KS** Kohn-Sham xi, xiii, xvi, 5, 14, 16, 17, 19, 23–28, 31, 33, 34, 44, 46, 53, 56, 59, 73
- LCAO** linear combination of atomic orbitals xi, xiii, xvi, xix, 5, 25–27, 44, 46, 51–54, 73
- LDA** local-density approximation 19, 25
- LHC** light-harvesting complex 3, 5
- LUMO** lowest unoccupied molecular orbital 2, 37, 57, 58, 71, 77, 78
- OPV** organic photovoltaic xi, xiii, 1–6, 74
- PAW** projector-augmented wave 5, 26, 29, 44, 46
- PBE** Perdew-Burke-Ernzerhof 20, 21, 44, 46
- PBEsol** Perdew-Burke-Ernzerhof for solids 21, 46, 63, 64
- PW** plane wave xix, 25, 26, 28, 44, 53, 54
- QZ** quadruple- ζ 44, 51, 52
- QZP** quadruple- ζ polarized 44, 51, 52
- SWCNT** single-walled carbon nanotube xix, xxi, 2–7, 39–41, 46–49, 51, 59–66, 68–70, 73, 74
- SZ** single- ζ 27, 44, 51, 52
- SZP** single- ζ polarized 44, 51, 52
- TDDFT** time-dependent density functional theory xi, xiii, 5, 29, 31, 33, 34, 36, 56
- TZ** triple- ζ 51, 52
- TZP** triple- ζ polarized 51, 52
- VBM** valence band maximum 23, 25
- xc** exchange and correlation xv, 6, 16, 19, 21, 24, 31, 34, 35, 44, 46, 47, 63